Dynamics of aggregation and dissociation in quantum matrices

Roland Panzou

Université Gustave Eiffel

MSME
LABORATOIRE MODÉLISATION ET SIMULATION MULTI ÉCHELLE
Sous la co-tutelle de :
CNRS
UNIVERSITÉ GUSTAVE EIFFEL
UPEC - UNIVERSITÉ PARIS-EST CRÉTEIL

PARIS EST SUP ÉCOLE DOCTORALE
Sciences, Ingénierie et Environnement

THÈSE

POUR OBTENIR LE TITRE ET GRADE DE
DOCTEUR ÈS SCIENCES

SPÉCIALITÉ : CHIMIE

PAR

ROLAND PANZOU

Dynamics of aggregation and dissociation in quantum matrices

Dynamique d'agrégation et de dissociation dans des matrices quantiques

---

Sous la direction de Monsieur le Professeur Marius LEWERENZ

Thèse soutenue le 17 Novembre 2022 devant le jury d'examen :

Dr. Nadine HALBERSTADT	Université Paul Sabatier	Rapporteuse
Dr. Nicolas SISOURAT	Sorbonne Université	Rapporteur
Pr. David BONHOMMEAU	Université d'Evry	Examinateur
Pr. Isabelle NAVIZET	Université Gustave Eiffel	Présidente du jury
Pr. Marius LEWERENZ	Université Gustave Eiffel	Directeur de thèse

Acknowledgements

This thesis was carried out in the Theoretical Chemistry (CT) group of the Modélisation et Simulation Multi Echelle (MSME) laboratory at the University Gustave Eiffel.

I would like to thank the members of my thesis committee: Dr. Nadine Halberstadt, Dr. Nicolas Sisourat, Prof. Dr. David Bonhommeau and Prof. Dr. Isabelle Navizet for their questions, comments and suggestions during the defense of PhD research. Thank you very much for taking time to read and correct my thesis !

I would like to express my gratitude to Prof. Dr. Marius Lewerenz, my thesis supervisor, for his trust and time as well as for sharing his knowledge and science during three and a half years of collaboration since Master internship. I have learned a lot, which will be useful to me both scientifically and on a human level. It was a pleasure and a privilege to work with you. Vielen Dank !

I would like to thank Dr. Mirjana Mladenović for taking time to give me advice and suggestions during the writing time. Hvala vam !

I would like to express my thanks to the other permanent members of Theoretical Chemistry group, in the order of their first names: Dr. Alexander Mitrushchenkov, Prof. Dr. Céline Léonard, Dr. Etienne Mangaud, Dr. Frédéric Le Quéré, Dr. Halima Mouhib, Prof. Dr. Isabelle Navizet and Dr. Loïc Joubert-Doriol. A special thanks to Dr. Marie Guitou, who guided me towards theoretical chemistry when I was hesitant with experimental chemistry.

My thanks go to all of you for the moments we shared, the teaching during the undergraduate and graduate courses and advices during the doctoral thesis. Eight years in a row !

I would like to express my thanks to current and former non-permanent members: Dr. Juan Sanz Garcia, Dr. Madjid Zemmouche, Dr. Mehdi Sahihi, Dr. Mohamed Bensifia, Dr. Mohamed Cheraki, Fanny Schnetz, Houda Moumene, Kossi Kety, Mina Asaad, Robin Manevy and Rosa Maskri. We had a great time together and I wish you all the best for your careers and your current PhD thesis !

I would like to extend my gratitude to Dr. Rajko Ćosić with whom I learned a lot about graphic users interface and scripting during the first month of my PhD thesis!

I would like to thank administrative and technical staff of the laboratory: Siméone Boston, Laurie Valdes and Guillaume Sauvenay.

I am thankful to the University Gustave Eiffel (ex-UPEM) and the doctoral school Paris-Est Sup for funding my research.

Finally I would like to express my gratitude to my family, my parents for supporting and encouraging me throughout my school career, from kindergarten until now. Thank you very much !

Abstract

For the past 30 years, helium nanodroplets (HeNDs) have been of particular interest to experimentalists. Specifically, this is a cold dense finite liquid environment which is an excellent medium for spectroscopy applications, atomic and molecular collision physics as well as ultra cold chemistry, with the ability to isolate interesting reactions intermediates, such as HCN-HF complex or to synthesize new materials as metallic nanowires. These phenomena are consequences of the quantum collective behaviour of helium atoms at a temperature T < 1 K which classify helium nanodroplets as quantum liquids. In this PhD thesis, we model photodissociation of immersed molecular iodine, the doping and the rotational excitation of these droplets. A computational molecular dynamics code, developed by Prof. Dr. Marius Lewerenz, called the CLUSTER code, has been used. To take into account the quantum nature of helium atoms, the methodology exploits the quantum effective potential technique at experimental work temperature 0.37 K.

With the photodissociation, an excitation above a molecular fragmentation limit leads to two possible scenarios depending on the energy dissipated by the helium droplets. The first one is the fast recombination, the so-called "cage effect", and the second is where photofragments reside in the helium bath. But with nanometer-scaled droplets a third scenario is also possible with fragments leaving the cluster surrounded by a helium solvation shell. Results are shown for helium nanodroplets containing thousands of atoms (2500 to 9000 He) and statistics on size and velocity of I@He_n photofragments have been computed and are similar to experimental outcomes for the analogous system CH_3I.

According to experiments using 1 fs X-ray flashes, the helium nanodroplets are geoids such as the Earth which is a hint indicating a rotation. Our code can set precise angular momentum in order to study the pattern of distortion from fission to multiple splitting. To evaluate the number of sub-clusters a Complete Clustering algorithm based on graph theory has been written exhibiting a linear complexity.

To conclude a study on xenon doping is presented where the recombination dynamics unveils a metastable state called Atkins' snowball which is a metastable state where the helium atoms are structured as crystals surrounding the interacting dopant, and different patterns of aggregation as nanocrystals and nanowires well known to experimentalists.

Keywords: Aggregation and dissociation, Cluster, Helium nanodroplets, Molecular Dynamics, Quantum matrices, Zero Point Average Dynamics.

Résumé

Depuis 30 ans, les nanogouttes d'hélium présentent un intérêt particulier pour les expérimentateurs. En effet, c'est un milieu dense, fini, froid et liquide qui en fait une excellente matrice pour des applications en spectroscopie, en physique des collisions ainsi qu'en chimie ultra froide avec la possibilité d'isoler des intermédiaires réactionnels d'intérêt comme le complexe HCN-HF ou de synthétiser des matériaux innovants avec les nanofilaments de métaux. Ces phénomènes sont dus aux propriétés particulières du comportement collectif quantique des atomes d'hélium à des températures T < 1 K qui classent les nanogouttes d'hélium parmi les liquides quantiques.

Nous nous proposons de modéliser la dynamique de photodissociation de molécules immergées dans des nanogouttes d'hélium, l'implantation de dopants ainsi que la dynamique de ce fluide, c'est-à-dire la déformation et le déchirement, à des températures avoisinant 0,37 K.

Pour tenir compte des effets quantiques, la méthodologie repose sur la technique des potentiels effectifs. Dans le premier cas évoqué ci-dessus, une excitation au-delà du seuil de fragmentation moléculaire conduit à deux scénarios dépendant de l'amortissement énergétique de la matrice liquide. La première observation est la recombinaison rapide dit « effet cage » et la seconde est celle où les photofragments perdurent dans le bain. Cependant, dans un environnement de taille nanométrique, une autre voie est possible avec la sortie des photofragments de la nanogoutte d'hélium avec ou sans atomes de solvant. Dans cette partie, des résultats de simulation de photodissociation du diiode à différentes énergies d'excitation seront montrés pour des systèmes contenant des milliers d'atomes d'hélium (2500 à 9000 He). Grâce à cela, nous obtenons des statistiques sur la vitesse et la taille des photofragments I@He_n similaires aux résultats expérimentaux pour un système analogue CH_3I.

Selon des expériences utilisant des flashs à rayon X d'une femto seconde sur ces nanogouttelettes, la forme de ces dernières est celle d'un géoïde ce qui indique une déformation par la rotation. Notre code permet de d'attribuer un moment cinétique L précis aux gouttes. En augmentant L, nous observons une transition entre déformation et fission puis fragmentation multiple. Pour évaluer rapidement le nombre et la taille des fragments, un algorithme d'analyse de graphe de complexité linéaire a été développé (« complete clustering »).

Pour finir, une étude préliminaire du dopage des nanogouttes par des atomes de xénon est présentée. En effet, la recombinaison des dopants sous forme d'agrégat à l'intérieur de la nanogoutte passe par un état métastable qu'est le « snowball d'Atkins », où les atomes d'hélium forment une couche cristalline autour des dopants.

Mots-clés: Agrégation et dissociation, Cluster, Dynamique moléculaire, Hélium, Matrices quantiques, Potentiels effectifs quantiques.

Table of contents

List of Figures

List of Tables

Abbreviation list

AIMD: Ab Initio Molecular Dynamics
CCA: Complete Clustering Algorithm
CFG: Configuration file
DFT: Density Functional Theory
DMC: Diffusion Monte Carlo
GUI: Graphic User Interface
HeND: Helium NanoDroplet
LCG: Linear Congruential Generator
LIF: Laser Induced Fluorescence
MC: Monte Carlo
MD: Molecular Dynamics
MSME: Modélisation et Simulation Multi Echelle
OT-DFT: Orsay-Trento Density Functional Theory
PIMD: Path Integral Molecular Dynamics
QEP: Quantum Effective Potential
QMC: Quantum Monte Carlo
VMC: Variational Monte Carlo
VMI: Velocity Map Imaging
TDDFT: Time-Dependent Density Functional Theory
TOF-MS: Time of Flight - Mass Spectrometry
ZPE: Zero Point Energy

Part I

Introduction

Chapter 1

Experimental observations on helium

Investigation of liquid helium started during the first half of the XXth century. The observations made in these studies provide inspiration for many ongoing experiments and theoretical investigations. The special and unique properties of liquid helium open the way for the chemistry in a cold dense (finite) and liquid environment.

1.1 First observations

At low temperature helium is a quantum liquid with properties of a superfluid which is a physical phenomenon observed by physicists and examined by Kapitza, Allen and Misener in 1938 [1, 2]. This nature appears below the λ-point (2.17 K). This specificity of helium characterises it as a fluid where there is no viscosity which indicates no loss of energy. This phenomenon has been seen for ^{4}He and later for ^{3}He whose λ-point is at 2 mK. This difference can be explained by the fact that ^{4}He is a boson. ^{3}He is a fermion, only pairing at lower temperature induces the superfluidity. This research topic was awarded by the Nobel prize where main contributors were David M. Lee, Douglas D. Osheroff and Robert C. Richardson in 1996.

In the middle of the 20th century, several experiments on liquid helium have been done to illustrate its quantum nature specially about the rotation of this solvent. In 1956, Hall and Vinen discovered during experiments on ^{4}He, the so-called Helium II, when it is a superfluid, the presence of quantized vortice line structures [3, 4]. In 1964, Rayfield and Reif demonstrated that those quantum perturbations can be rings [5]. The rotation in this fluid is quantized meaning that the rotational angular momentum given by a vessel needs to be a multiple of $\hbar$.

However all those observations concern helium in bulk and not helium nanodroplets. Then we can raise a question: are helium nanodroplets superfluids ?

In order to get an answer to the latter question a brief review of helium nanodroplet formation, doping and experimentation will be given in the following parts.

1.2 Formation of helium nanodroplets

Helium nanodroplets (HeND) are most commonly made by a gas expansion of helium. In 1908, Kamerling Onnes [6] proceeded to the liquefaction of helium which was a first step on the road to study HeND. In 1961, Becker, Klingelhöfer and Lohse [7] produced for the first time HeND inside a supersonic gas expansion where soft collisions between helium atoms allow the growth of clusters. This way of production gives a certain rotational movement to HeND because each random collision with a helium atom affects an existing droplet. In 1977, ^{3}He and ^{4}He cluster beams were created according to the works of Gspann *et al.* [8, 9]. More than a decade later, experimentations in the Toennies' group led to the rediscovery of HeND by time of flight mass spectrometry (TOF-MS) [10]. This was the first time that the production of HeND was published in a scientific paper. A typical design [11] of a machine used to produce HeND is schematically shown below in Figure 1.1. The machine is composed of three parts. The first part is the place of the formation of the helium nanodroplets by a gas expansion starting at high pressure (P_0=20-100 bar) and low temperature (T_0=5-20 K) through a nozzle typically about 5 µm of diameter. Cluster growth by condensation occurs in this step and the low temperature is a consequence of the helium atom velocity homogenisation through the nozzle. The main

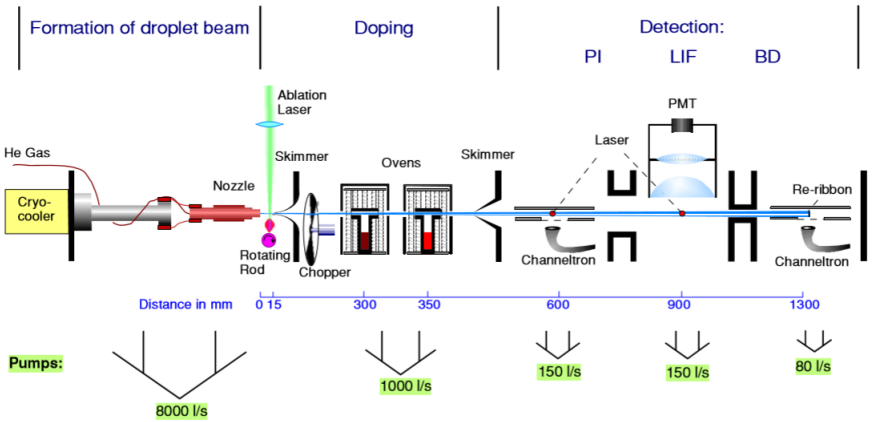

Figure 1.1: Scheme of typical experimental machinery of production and analysis of helium nanodroplets [11]
Representation of the different compartments for formation, doping and detection of photofragments (PI: photoionisation detector, LIF: laser induced fluorescence, BD: bolometric detector [12])

parameter to control is the cluster size which depends on the nozzle diameter, the temperature and the reservoir pressure. The latter conditions determine the kind of expansion : supercritical or subcritical (λ-point at T = 2,17 K). The supercritical expansion favours the production of droplets with a lot of helium atoms ($\overline{N} > 3.10^4$) and the subcritical one small clusters ($\overline{N} < 3.10^4$). The typical HeND size in spectroscopic experiments is about 5000 helium atoms in a cluster. In a LIF study of HeND at P=20 bar and T=15 K, for instance, Stienkemeier *et al.* [13]

found the maximum of the signal at about 5000 helium atoms/droplet for Na-doped ^{4}He.

To determine the cluster sizes and their distributions, Lewerenz, Schilling and Toennies [14] used a method of scattering deflection on HeND in order to get an angular distribution of cluster sizes. These authors crossed the helium and SF_6 beams and showed that the collision between the two species is inelastic with complete transfer of the momentum on the cluster in the direction where the HeND momentum equals to zero. Droplets containing up to 10^{10} helium atoms were created by the group of Vilesov in 2011 with a continuous-nozzle beam expansion and different techniques for HeND detection [15–17].

Other techniques to produce helium clusters, like pulsed helium droplet beams [18, 19], have been built to bypass the need for a chopper in some continuous helium beam. An example of the formation of HeND is shown in the following Figure 1.2. There, a collimated helium flux condenses by a mechanism of soft collisions to form HeND.

Helium clusters, formed in the first part are studied by different techniques of spectroscopy in order to get information on the structure of the dopants and also on the physics of the special fluid at temperatures near the absolute zero (-273 °C). In the next section some important experiments are briefly described, with special attention paid to experiments whose aim is to confirm its superfluid nature.

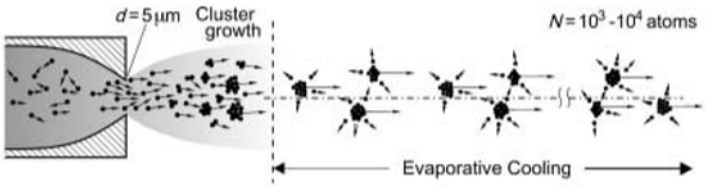

Figure 1.2: Scheme of the formation of helium nanodroplets in a supersonic gas expansion [20]

1.3 Experiments on HeND

1.3.1 HeND doping

Following the part of HeND growth, experiments can be done on the cluster like implanting another species (doping). These experimentations take place in the second part of the machinery see above (Figure 1.1) which is the pickup cell. The latter one depends on the heliophilicity but the majority of the elements of the periodical table are heliophilics. This criterion defines the fact that the dopants are localized inside or on the surface of the HeND. Experimental works proved that alkali atoms reside on the helium clusters surface because no spectral shift appears which is typical for species embedded in this matrice [21, 22]. However experimentalists worked on alkali clusters and then remarked that indirect ionization of those dopant clusters

sank into the center of HeND to lower the potential energy by a process of charge transfer from He toward alkali [23]. The same observation was confirmed recently for Rb [24].

The pickup technique was developped by the group of Scoles. [25] in 1985. However some works from Gspann in 1981 showed the doping of HeND with heavy atoms like cesium or noble gases like xenon [26]. During this process the nanodroplets are shrunk by the collisions with foreign atoms and the evaporation of solvent atoms. In fact, some experiments about pickup were made in 1990 by Scheidemann, Schilling, Northby and Toennies who showed that the foreign atoms were not scattered but embedded [27] in the HeND because its signal in the spectrometer was coincident with the helium cluster. This was the first time that doping HeND was officially introduced. However, a collaborator of Becker, Gspann revealed that his team had worked on cesium atoms doping HeND (^{3}He and ^{4}He clusters) by publishing their results in 1995 [28]. Technique of picking up evolves by integrating a heat cell to vaporise some metallic elements [29], pyrolysising to produce propargyl radicals [30] and even by laser ablation [31]. Some molecules of biological importance such as tryptophan and tyrosine were embedded in HeND to conduct some experiments [32]. The HeND are not destroyed during their travels in rough conditions because the energy needed to ionize helium exceeds 20 eV [11].

Likewise in 1995 a mix between experimental and theoretical chemistry with Monte-Carlo (MC) was done and confirmed that HeND catch foreign atoms and those latter form cluster inside their matrice [33]. The latter study presented that the pick-up process proceeds according to a Poisson law (P_k) depending on the previous number of atoms caught. This approximation does not take the shrinking of the cluster into account. In fact, during successive collisions, the HeND looses atoms by an evaporative process.

$$P_k = \frac{\bar{k}^k}{k!} e^{-\bar{k}} \tag{1.1}$$

In eq. (1.1) the parameter k is the number of dopants in the HeND, $\bar{k}$ is the mean number of k which is a function of the pressure in the pick-up cell. More recently other techniques like merged beams were set up instead of passing through a specific doping structure. The latter method was utilized in the study of Hideho Odaka and Masahiko Ichihashi in 2017 where they crossed cobalt cluster generated from laser ablation and HeND [34].

These studies paved the way for more aggregation and dissociation experiments in HeND. In fact, experimentalists succeeded to dope HeND with molecules like SF_6 [35] and OCS [36], charged proteins [37, 38]. The experiments of doping HeND by OCS revealed the superfluid nature of the droplets by showing resolved rotational spectra. By those experiments some group of researchers doped helium clusters with different type of atoms and observed the formation of core-shell structures. Likewise in large HeND, which presents fluid perturbations named quantum vortices, nanowires were detected [39]. The resume of the main experiment on HeND

showed that this kind of fluid can be doped by a lot of different species. This ability of catching and solvating the foreign atoms or molecules lead to study on the cohesive or evaporative energies by photodissociating some species whose physical and chemical properties are well known. The following paragraphs present experimentations of photodissociation of molecules in HeND.

1.3.2 Photodissociation of molecules inside HeND

With all the different techniques of doping HeND one subject of interest at experimental and theoretical scale is the photodissociation of species in helium clusters. In this thesis, we are interested in the photodissociation of molecular iodine which is a well-studied object in the gas phase and matrices whose interacting potentials can easily be found in the literature [40]. In fact, the phenomenon of dissipation of energy is particular in a soft, dense, finite and cold environment. What is interesting in this case is in a common liquid two scenarios can occur. The first one is known as a fast recombination of the dopants, the so-called cage effect [41]. The evaporation of helium atoms is a conversion of the excess energy and then the HeND comes back to the thermal equilibrium. The second case occurs when the photofragments travel in the solvant. However in a nanometric system a third way is possible with the fragments leaving the cluster when the excess of energy is higher than the amount the HeND can dissipate. The Braun and Drabbels works on photodissociation have brought some elements of comprehension about energy transfer by doping helium droplets with CH_3I, C_2H_5I and CF_3I [42] and exciting the systems by a 266 nm Nd:YAG laser. They studied the velocity and angular distributions of the photofragments of the species listed above. This reveals that the transfer of energy is a direct non-thermal process where heavy dopants push the helium atoms away. Moreover the analysis [43] by TOF-MS of the exited photofragments has shown that they are composed of a dopant surrounded by helium atoms which is a partial solvating sphere. They also studied the recombination using the velocity map imaging (VMI) to analyse the process [44].

1.3.3 HeND excitations

A direction of this thesis is the study of the deformation, the fragmentation and the fission of the HeND. In fact, according to the research of Gomez *et al.* in 2014 the experiments [45] using ultra fast X ray on the helium clusters showed that during the process of formation, some nanodroplets were geoid-shaped. This observation was confirmed by articles about the shapes of the large rotating HeND and their angular momentum [46, 47]. The shape of the nanodroplets, where the angular momentum (L) is equivalent to zero, have a spherical shape. According to the investigation when there is an increasing of L, the HeND get elongated and split into two or more lobes perpendicularly of the axis of rotation. However, in certain case, the

oblate form can be conserved if the energy of rotation is below the cohesive threshold which is an oblate metastable form. As a rotating fluid, experimentalists made the assumption that there is distortion in the fluid. In order to study that, the experiment was based on the assumption of Onsager saying that the rotation of helium is quantified because of its quantum nature. The same supposition was done for helium nanodroplet. The work of Gomez, Loginov and Vilesov [39] in 2012 by doping the cluster with silver atoms and they observed the formation of silver nanowires through the quantum vortices and analyse the structure by soft-landing technique. The helium droplets are superfluid and offer an original matrice for diverse experiments and numerical simulations.

Chapter 2

Computational modelling of HeND

2.1 Some numerical tools

As seen in the previous part of this introduction there is a significant body of dynamic and spectroscopic observations of HeND. Most of the theoretical studies on HeND explore the static properties like density and cohesive energy with help of nuclear density functional theory (DFT) and quantum Monte Carlo (QMC). There is actually no fully quantum dynamical method available.

The theoretical works on HeND are motivated by the fact that the elementary excitation spectrum and the superfluid fraction are accessible in bulk helium but not in nanodroplets. Indeed experiments of HeND scattering are limited because of the weak cluster flux and the measurement of their moment of inertia for rotating clusters are not possible. By adding some foreign atoms in those structures at temperature where superfluid behaviour is apparent, the extracted informations can be similar to the bulk as the dissipation of rotational, translational vibrational energy of dopant and the estimation of the helium cluster temperature and potential energy [48].

The main methodologies used for calculating HeND properties are the nuclear DFT and the QMC and their variants. The first method is based on the Hohenberg-Kohn theorem [49]. This theorem postulates that the total energy is a functional of the one-particle density for a many-body quantum system and can be expressed as [50]:

$$E[\rho] = T[\rho] + \int \mathrm{d}r \varepsilon_c[\rho] \tag{2.1}$$

Where $T[\rho]$ is the kinetic energy of the particles in the system and $\varepsilon_c[\rho]$ is the interaction term. A version of DFT taking the time evolution into account has been developed and is well-known as Time-Dependent-DFT (TDDFT) based on the Runge-Gross theorem [51]. This technique allows the production of vortices in the HeND but the quality of the results depends strongly

on the functional. In the case of helium the van der Waals forces dominates in this fluid as well as the dispersion likewise for the dopant interactions. To overcome these problems which affect the accuracy of the methods the Orsay-Trento DFT (OT-DFT) [52] has been developed by integrating experimental data of bulk liquid like the chemical potential, the equilibrium density and the dispersion relation. But the functional used for a system is not universal and needs parametrisations. Moreover, the computation cost by including quantum description is important and only permit the simulation of thousands of helium atoms.

QMC techniques are used to interpret statistically the wave function of a many-body quantum system [53]. The problem can be split in four parts where the distribution of the energy is known with $T = 0\,K$ and $T > 0\,K$. In this cases classical Monte Carlo (MC) can be apply. When the distribution of energy is unknown with $T = 0\,K$ and $T > 0\,K$ different techniques of QMC are used. For $T = 0\,K$, the Variational MC (VMC) and the Diffusion MC (DMC) are techniques to sample a quantum state with unknown properties. The idea of the VMC is to use non-factorisable trial wave functions with free parameters and to approach approximatively the properties of a many-body quantum system by using the variational principle and MC. The DMC is a MC which uses the Green's function to solve the Schrödinger's equation. This method gives the exact ground state energy where the results suffer only from statistical errors. For $T > 0\,K$, the technique used is the Path Integral MC (PIMC) which reposes on the path integral formulation which describes the trajectory of a particle by a sum over the infinity of quantum-mechanically possible trajectories. This type of method strongly depends on the number of path descriptors to be accurate.

The MC techniques give data on quantum systems which are static so other methods have been developed to simulate large helium clusters with less parametrisations than in DFT method. The Molecular Dynamics based on quantum effective potential is a nice choice between these compromises and the hardware limitations.

2.2 Objectives

Having seen techniques of modelling and experiments on the HeND and aiming to simulate large helium clusters with less parametrisations and computational cost, the Molecular Dynamics based on quantum effective potential (QEP) has been chosen for computational method. The idea is to get a dynamic descriptions of the phenomena occurring during the photodissociation, the vibrational and rotational excitations of dopants or of HeND and finally the impact and aggregation on/in nanodroplet. This technique has been used several times to model pick up and fragmentation within HeND [54–56]. To achieve these objectives the MD code used is an home-made one named CLUSTER developed by Prof. Dr. Marius Lewerenz and based on QEP. This MD program can simulate helium clusters containing up to 10,000 atoms and it is

vectorised to minimise computational costs. An important part of the work in this thesis was to develop some tools related to the CLUSTER code in order to excite dopants and HeND, for the doping of the nanoclusters in order to get significant statistics on the physical phenomena and compare them to the experimental outcomes. Moreover, scripts have been developed to automatically handle launching and data collection for multiple trajectories and to visualise the behaviour of the droplet undergoing the experiments described previously.

This thesis is divided in three other parts with the Part II Methodology : theoretical and technical elements where all the basis of this research work are presented starting from the statistical mechanics visiting the kinetic theory of gas, the Molecular Dynamics, the interaction potentials and finishing with method to excite HeND, to determine the number of fragment clusters, the development of random numbers and the adjusting of the effective quantum potential by the chemical potential. Part III is essentially focused on the results on photodissociation of molecular iodine for different HeND sizes, the rotational and vibrational excitation of the same diatomic in the helium nanobath, the study of the HeND excitation and terminates with a work on the impact and aggregation in the nanodroplet. The last part of this document is a resume and an outlook of this topic.

Part II

Methodology: theoretical and technical elements

Chapter 3

Statistical mechanics

3.1 Generalities

Statistical mechanics is the bridge between microscopic phenomena and the macroscopic explanation of physical parameters as temperature, pressure or heat capacity. The main contributors to this theory are Ludwig Boltzmann, James Clerk Maxwell and Josiah Willard Gibbs.

By averaging these microscopic values based on quantum or classical mechanics, this field of science [57–59] gives access to macroscopic properties of bulk matter because the experiments can not have instantaneous informations over each particle in a bulk. The microscopic parameters fluctuate around average values and have probability distributions which depends on the former parameters(N,V,T,P,μ,...). This paradigm is formulated on the fact that particles in bulk can occupy different states at thermodynamic equilibrium. Then the access of the macroscopic property values is available for systems of N particles in an ensemble with N tending to infinite. Statistical mechanics defines basic equilibrium ensembles for systems in steady states but in this thesis the interest is over three of them:

- Micro-canonical ensemble: this one describes a system with no exchange of particles, an invariant volume and at constant energy. All the states have the same probability which are in accordance with the energy and the composition of the system. It is applied to an isolated system.

- Canonical ensemble: describes a system with fixed number of system components, volume and at constant temperature. The exchange of energy with an external system is allowed.

- Grand canonical ensemble: describes a system where the exchange of particles is allowed, in thermal and chemical equilibrium with a reservoir. The system presents different energy states occupied by different numbers of particles.

Statistical mechanics relies on two fundamental postulates:

- Ergodicity: this idea was described by J. Willard Gibbs in 1902 by the concept of an ensemble of η replicas of a thermodynamic system having reached an equilibrium state in an ensemble. The fluctuations after exchanging energy are small and the properties of a system are time independent. Then Gibbs proposed to compute the thermodynamic values over all the η replica instead of one. In molecular dynamics, this concept can be translated as to allow the system to start with different initial conditions in phase space and let the different dynamics runs over a sufficient time of simulation to explore it.

- Equal *a priori* probability: the many body system states are distributed over all the energy states consistent with the energy of the system. This postulate defines the micro-canonical ensemble

In this work the HeND are simulated in a micro-canonical ensemble denoted NVE where the particles exchange energy between them. In these conditions a subset of particles can describe a canonical sub-ensemble or NVT. The latter is not treated in this document.

3.2 Ergodicity in molecular dynamics

In experiments the value are determined by several experiments which give the average value of macroscopic parameters. The Molecular Dynamics works in the same way of sampling over a long time to get the average physical details over a trajectory. This is time averaging for Molecular Dynamics and ensemble averaging for Monte Carlo simulation which average all the possible states of a system. The evolution of the system depends on the coordinates of positions r and momenta p which compose the phase space. This space has 6N dimensions. The system starts with initial conditions in accordance with the ensemble conditions where it evolves. Then, by averaging over the trajectory the observable A is computed, when equilibrium is reached, by:

$$A_{obs} = \langle A \rangle_{time} = \lim_{t_{obs} \to +\infty} \frac{1}{t_{obs}} \int_0^{t_{obs}} A\left(r^{\mathrm{N}}, p^{\mathrm{N}}, t\right) \mathrm{d}t \tag{3.1}$$

The trajectory of Molecular Dynamics is integrated over a large finite number of time step where the length is $\delta \mathrm{t} = \mathrm{t}_{obs}/\tau_{obs}$ where τ_{obs} is the number of steps. Then eq. (3.1) must be written as :

$$A_{obs} \approx \langle A \rangle_{time} = \frac{1}{\tau_{obs}} \sum_{\tau=1}^{\tau_{obs}} A\left(r^{\mathrm{N}}, p^{\mathrm{N}}, \tau\right) \tag{3.2}$$

Over a sufficient long time of simulation, the trajectory should not depend on the initial coordinates within the phase space. The limit of the time average is to take into account all the possible points $(r^{\mathrm{N}}, p^{\mathrm{N}})$ in the phase space in accordance with the NVE ensemble by running

simulations over them. So that the link between time and ensemble average can be expressed as:

$$A_{obs} = \langle A \rangle_{time} = \lim_{t_{obs} \to +\infty} \frac{1}{t_{obs}} \int_0^{t_{obs}} \langle A \rangle_{ensemble} \mathrm{d}t \tag{3.3}$$

But the ensemble average by Monte Carlo is time independent so that the method of time and ensemble averaging are equivalent.

$$A_{obs} = \langle A \rangle_{time} = \langle A \rangle_{ensemble} \tag{3.4}$$

The ergodicity principle is respected because averaging over a long time simulation is comparable to averaging an ensemble with η replica according to an NVE as stipulated by Gibbs.

3.3 Kinetic theory of gases

The kinetic theory of gases is a part of statistical mechanics which also explains macroscopic values by microscopic one such as the temperature and the pressure of a system by applying Newton law to the motion of atoms which constitute the ideal gases [60] as point objects without potential interactions where total energy is kinetic energy.

3.3.1 Ideal gas pressure

The pressure of molecules or atoms is due to collisions with the wall of a container. The number of collisions depends on gas density. The higher is the density the larger is the number of collisions. To express the pressure of an ideal gas, Newton law has to be applied to the system to unveil the relation between pressure, volume and the square velocity average of atoms in a gas. The simplest model is to take the motion in one dimension into account and then, develop it on the two other dimensions. Starting from scratch, atoms in a gas move without any distributions. The first assumption is to define the number of atoms colliding the wall of surface S. To achieve that the density of the gas ρ, the distance between the atoms and the surface, depending on Δt, as to be set to express the number n_{atoms} moving at a velocity v_x. By combining the former parameters, the number of atoms hitting the wall for + x direction is :

$$n_{atoms} = \frac{1}{2} \rho \mathrm{S} v_x \Delta t \tag{3.5}$$

By applying the second law of the Newton motion which stipulates that:

$$\sum_i \mathrm{F}_{i,x} = m a_x = \frac{d(m v_x)}{dt} \tag{3.6}$$

The expression of the force in the case of collision with the container wall on an integrating step of Δt is given by:

$$\mathrm{F_x}\Delta t = \Delta(mv_x) = 2mv_x \tag{3.7}$$

Indeed, the force of collisions of one atom is equal to twice the momenta of these particles because when it collides the wall, in the case of elastic collisions, there is no loss of kinetic energy. The momentum of a particle changes from + mv_x to - mv_x. With an amount of n_{atoms} eq. (3.7) is written as:

$$\begin{aligned} \mathrm{F}\Delta t &= \rho \mathrm{S} m v_x^2 \Delta t \\ \mathrm{F} &= \rho \mathrm{S} m v_x^2 \end{aligned} \tag{3.8}$$

The mathematical definition of pressure is:

$$\mathrm{P} = \frac{\mathrm{F}}{\mathrm{S}} \tag{3.9}$$

Then, the pressure is expressed by:

$$\mathrm{P} = \rho m v_x^2 \tag{3.10}$$

Where taking the velocity to the square average on x-component of space, eq. (3.10) is written as:

$$\mathrm{P} = \rho m \langle v_x^2 \rangle \tag{3.11}$$

The velocity of atoms in gas have other components of space so the average squared velocity over all the Cartesian space can be expressed as:

$$\langle v^2 \rangle = \langle v_x^2 \rangle + \langle v_y^2 \rangle + \langle v_z^2 \rangle \tag{3.12}$$

The motion of atoms in an isotropic gas is random and the velocity is the same over all directions of space so $\langle v_x^2 \rangle = \langle v_y^2 \rangle = \langle v_z^2 \rangle = \langle v^2 \rangle / 3$. Then the pressure is:

$$\mathrm{P} = \frac{1}{3} \rho m \langle v^2 \rangle \tag{3.13}$$

According to eq. (3.13), the pressure is a function of the average squared velocity of particles. By pushing forward this equation, the kinetic energy can be deduced and likewise with the analogy with the ideal gas law. The number of atoms by unit volume ρ can be written as $\mathrm{n}N_A/\mathrm{V}$ where n is the number of moles, N_A Avogadro's number and V the volume. Then the pressure is:

$$\mathrm{PV} = \frac{1}{3} n N_A m \langle v^2 \rangle \tag{3.14}$$

Knowing that the kinetic energy per particle expression is $\langle \mathrm{E} \rangle = \mathrm{m}\langle v^2 \rangle/2$, eq. (3.14) is rewritten as:

$$\mathrm{PV} = \frac{2}{3} n N_A \langle \mathrm{E} \rangle \tag{3.15}$$

Eq. (3.15) shares some similarities with the ideal gas law PV = nRT. With this relation a link between kinetic energy and temperature can be deduced.

3.3.2 Energy and temperature

The energy transfer between two isolated systems with different temperatures give the following outcome. The hotter system has a decreasing temperature and the cooler one has an increasing until the two temperatures are equal and by extension the energies. So energy and temperature have a close link. The ideal gas law can connect these two concepts.

$$\mathrm{PV} = n\mathrm{RT} = \frac{2}{3} n N_A \langle \mathrm{E} \rangle \tag{3.16}$$

Then from eq. (3.16) and knowing that $\mathrm{R} = N_A k_B$ where k_B is Boltzmann constant,

$$\mathrm{T} = \frac{2}{3} \frac{\langle \mathrm{E} \rangle}{k_B} \tag{3.17}$$

The relation between mean kinetic energy and temperature is clearly showed:

$$\langle \mathrm{E} \rangle = \frac{3}{2} k_B \mathrm{T} \tag{3.18}$$

Likewise the relation between the average squared velocity and the temperature is given by:

$$\langle v^2 \rangle = \frac{3 k_B \mathrm{T}}{m} \tag{3.19}$$

3.3.3 The Maxwell-Boltzmann distribution

The velocities of gas particle do not have the same speeds and are subject to a distribution of each component of the Cartesian space. This function has to be an even function. In fact, the parameter of pressure is the same in each point of the space of a container. So there is an equal dispersion of particles in positive and negative directions of the space components. This is a characteristic of an isotropic gas.

The velocities of atoms in the gas are random in the space component. Moreover, the distributions of each component are independent and uncorrelated. So the global probability is

the product of the probability of each component of space.

$$p(v_x, v_y, v_z) = p(v_x)p(v_y)p(v_z) = p(v_x^2)p(v_y^2)p(v_z^2) \tag{3.20}$$

The function which can exhibit this kind of behaviour is the exponential where the product of exponential forms is the sum of exponents in a exponential function: $\exp(a+b+c) = \exp(a)\exp(b)\exp(c)$. The typical function which describes the distribution according to α=x,y,z is written as:

$$p(v_\alpha) = A_\alpha \exp\left(\pm B_\alpha v_\alpha^2\right) \tag{3.21}$$

As a probability distribution, the function is normalised on the range $]-\infty;+\infty[$. Then the pre-factor A can be deduced.

$$\int_{-\infty}^{+\infty} p(v_\alpha)\mathrm{d}v_\alpha = 1 \tag{3.22}$$

Integral is finite therefore -B is chosen with $B_\alpha > 0$.

$$A_\alpha \int_{-\infty}^{+\infty} \exp\left(-B_\alpha v_\alpha^2\right) = 1 \tag{3.23}$$

The solution of the eq. (3.23) is:

$$A_\alpha = \left(\frac{B_\alpha}{\pi}\right)^{1/2} \tag{3.24}$$

The average squared velocity is calculated with the distribution as:

$$\langle v_\alpha^2 \rangle = \left(\frac{B_\alpha}{\pi}\right)^{1/2} \int_{-\infty}^{+\infty} v_\alpha^2 \exp\left(-B_\alpha v_\alpha^2\right) \mathrm{d}v_\alpha \tag{3.25}$$

The solution of eq. (3.25) is:

$$\langle v_\alpha^2 \rangle = \frac{1}{2}\left(\frac{B_\alpha}{\pi}\right)^{1/2} \left(\frac{\pi}{B_\alpha^3}\right)^{1/2} = \frac{1}{2B_\alpha} \tag{3.26}$$

Eq. (3.26) is the solution for a simple space component. The relation which connects the global velocity and its components is $\langle v_x^2 \rangle = \langle v_y^2 \rangle = \langle v_z^2 \rangle = \langle v^2 \rangle/3$ according to eq. (3.12), the global solution is then:

$$\langle v^2 \rangle = \frac{3}{2B} \tag{3.27}$$

Eq. (3.27) is quite the same as eq. (3.19) which means that the average squared velocity respects the ideal gas law and B can be expressed as:

$$B = \frac{m}{2k_B \mathrm{T}} \tag{3.28}$$

Then the distribution on one-dimension of space well-known as the Maxwell-Boltzmann distribution can be written as:

$$p(v_\alpha)\mathrm{d}v_\alpha = \left(\frac{m}{2\pi k_B \mathrm{T}}\right)^{1/2} \exp\left(-\frac{mv_\alpha^2}{2k_B\mathrm{T}}\right)\mathrm{d}v_\alpha \tag{3.29}$$

The 3D Maxwell-Boltzmann distribution is given :

$$p(v_x,v_y,v_z)\mathrm{d}v_x\mathrm{d}v_y\mathrm{d}v_z = \left(\frac{m}{2\pi k_B \mathrm{T}}\right)^{3/2} \exp\left(-\frac{m\left(v_x^2+v_y^2+v_z^2\right)}{2k_B\mathrm{T}}\right)\mathrm{d}v_x\mathrm{d}v_y\mathrm{d}v_z \tag{3.30}$$

An observation is that the Maxwell-Boltzmann distribution is in accordance with the Boltzmann distribution law where the probability of finding an atom at a kinetic energy given is proportional to $\exp\left(-\mathrm{E_i}/k_B\mathrm{T}\right)$.

The distribution is a function which depends only on the speed of particles in gas and not on the direction. Moreover, the gas is isotropic, then the expansion is in a spherical volume. The distribution can be integrated over spherical coordinates:

$$p(v)\mathrm{d}v = \int_0^{2\pi}\int_0^{\pi} v^2 \left(\frac{m}{2\pi k_B \mathrm{T}}\right)^{3/2} \exp\left(-\frac{mv}{2k_B\mathrm{T}}\right)\sin\theta\mathrm{d}v\mathrm{d}\theta\mathrm{d}\phi \tag{3.31}$$

Then,

$$p(v)\mathrm{d}v = 4\pi v^2 \left(\frac{m}{2\pi k_B \mathrm{T}}\right)^{3/2} \exp\left(-\frac{mv}{2k_B\mathrm{T}}\right)\mathrm{d}v \tag{3.32}$$

The Maxwell-Boltzmann distribution in eq. (3.32) has an average value $\langle v\rangle$ equal to:

$$\langle v\rangle = \int_0^{\infty} v p(v)\mathrm{d}v = \left(\frac{8k_B\mathrm{T}}{\pi m}\right)^{1/2} \tag{3.33}$$

And the standard deviation for each velocity component is $\sqrt{k_B\mathrm{T}/m}$.

Chapter 4

Molecular Dynamics

4.1 The concept of MD

Molecular dynamics (MD) is a numerical technique where equations of motion are solved to determine the evolution of a system in time. This is a well known instrument used in many branches of science to study small systems, like clusters of atoms, to the largest like proteins.

MD is used to model the motion of a particle ensemble under different conditions depending on temperature or pressure in a physical time scale under the control of Newtonian mechanics [57, 59]. In this paradigm, atoms are treated as points avoiding all quantum effects.

The global idea of numerical simulation is to proceed like in experimental conditions. Three main steps are reported. The first one is initial condition setting by modifying positions and or velocities in a configuration file. Tools have been created during this work to modify this kind of file for studying rotation by setting droplet angular momentum, doping by setting positions and velocities dopant atoms and photodissociation by iodine velocity modifications. The second is the equilibration, a model is selected and Newton equations of motion are solved until there is relaxation or equilibration of the system. The last stage is data collecting and sampling to interpret the physical phenomena. Indeed, CLUSTER code gathers data and some external instruments have been programmed to automatise MD starting and collection of specific data such as photofragments kinetic energy.

4.2 Equations of motion

As previously described the MD solves Newtonian equations of motion for atoms and uses classic Hamiltonian :

$$H = \sum_i \frac{p_i^2}{2m_i} + V \tag{4.1}$$

m_i represents the atomic masses and V the potential energy :

$$V = V(r_1, r_2, r_3, ..., r_n) \tag{4.2}$$

The potential 4.2 is often expressed as a sum of pair potentials :

$$V = \frac{1}{2}\sum_{i \neq j} V_{ij}(r_{ij}) \tag{4.3}$$

$r_{ij} = |\vec{r}_i - \vec{r}_j|$ which represents the inter atomic distances and V_{ij} the pair potential depending on atom type. Hamilton's equations of motion state are:

$$\dot{r}_i = \frac{\partial H}{\partial p_i} \qquad \dot{p}_i = -\frac{\partial H}{\partial r_i} = -\frac{\partial V(r_1, r_2, r_3, ..., r_n)}{\partial r_i} \tag{4.4}$$

4.3 Integration of equations of motion

In this section, the objective is to present the strengths and weaknesses of different method to integrate motion equations in MD as Euler method and the Verlet algorithms.

4.3.1 Euler method

This numerical method aims to solve a first order differential equation by approximating the derivative :

$$f(x_i, y_i) = \frac{y_{i+1} - y_i}{x_{i+1} - x_i} \Leftrightarrow y_{i+1} = y_i + (x_{i+1} - x_i) f(x_i, y_i) \tag{4.5}$$

An analogy can be done with the rectangle rule where :

$$\int_{x_i}^{x_{i+1}} f(x,y)dx \simeq (x_{i+1} - x_i) f(x_i, y_i) = h f(x_i, y_i) \tag{4.6}$$

The method can be iterated :

$$\begin{cases} y_{n+1} = y_n + h f(x_n, y_n), \quad n = 0, 1, 2, ..., N \\ y_0 = y(0) \end{cases} \tag{4.7}$$

The Euler method of integration is a h first-order approximation which shows problems of accuracy. Moreover this method of integration presents the inconvenience of having numerical instabilities depending on the discretization step h. In MD, h represents the time step. The smaller it is the more accurate integration will be. The small time steps need longer simulations than other methods of integration to describe the same systems. Moreover, the Euler method needs a first step of test with different time step to minimize the numerical errors due to the

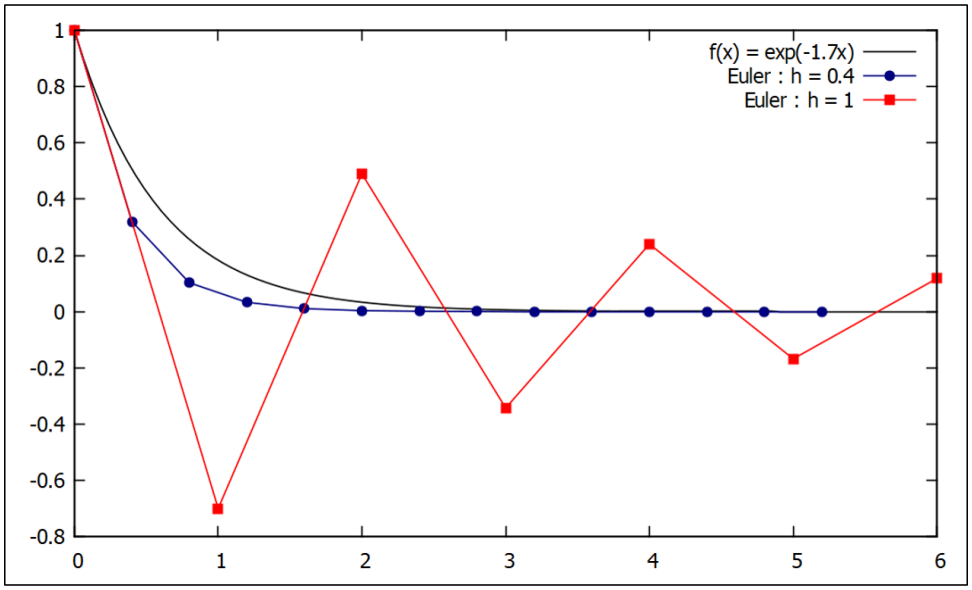

Figure 4.1: The solution of y' = -1.7y with Euler method with h = 0.4 (blue circles), h = 1 (red squares) and the exact solution (black)

truncation at the first derivative in the Taylor expansion. This means at each step of the MD the local numerical error is proportional to h^2.

$$y(t_0+h) = y(t_0) + hy'(t_0) + O(h^2) \tag{4.8}$$

One important thing is the rounding error in this method of integration which depends on ε, the machine precision. Even if small time step h is used rounding error can be huge on the calculations because computers represent number on finite number of bits.

4.3.2 Verlet integrators

Position Verlet algorithm

It was introduced by Delambre in the XVIII$^{\text{th}}$ and first used by Loup Verlet in 1967 for numerical simulations [61]. The central finite difference on the second derivative is used instead of the forward difference in Euler's method which gives a better approximation of the derivative. Then, we can determine two equations:

$$\begin{cases} x(t+\Delta t) = x(t) + v(t)\Delta t + \dfrac{(\Delta t)^2}{2}a(t) + \dfrac{(\Delta t)^3}{6}\dfrac{d^3x(t)}{dt^3} + O((\Delta t)^4) \\ \\ x(t-\Delta t) = x(t) - v(t)\Delta t + \dfrac{(\Delta t)^2}{2}a(t) - \dfrac{(\Delta t)^3}{6}\dfrac{d^3x(t)}{dt^3} + O((\Delta t)^4) \end{cases} \tag{4.9}$$

From the Taylor expansions in eqs. 4.9 the Verlet equations for advancing the position can be expressed after summation :

$$x(t+\Delta t) = 2x(t) - x(t-\Delta t) + (\Delta t)^2 a(t) + O((\Delta t)^4) \tag{4.10}$$

The velocity is not implemented in this algorithm because they are not needed to calculate the energy of the system, velocities can be found by the following approximation :

$$v(t) = \frac{x(t+\Delta t) - x(t-\Delta t)}{2\Delta t} \tag{4.11}$$

The fact that the Verlet algorithm is clearly centered shows the reversibility of this method which is an important property for an integration method. One point where problems can appear is the rounding error on the term $(\Delta t)^2 a(t)$ because it is small compared to the other terms. Moreover phase space can not be treated in a balanced way because positions and velocities are not treated in a equivalent way. The calculation accuracy on positions and velocities are not from the same order (Δt^4 and Δt^2) which means that the first is more accurate than the latter.

Leap frog Verlet algorithm

The Leapfrog integration [62] is derived from the standard Verlet algorithm. This strategy has been developed in order to reduce the rounding error induced by the local truncation error in the weak difference in eq. (4.11). The velocity and the position are updated as follows :

$$\begin{cases} v(t+\frac{\Delta t}{2}) = v(t-\frac{\Delta t}{2}) + a(t)\Delta t \\ \\ x(t+\Delta t) = x(t) + v(t+\frac{\Delta t}{2})\Delta t \end{cases} \tag{4.12}$$

In this scheme the velocity is computed before the position at a half integer time step. This operation is iterated over the simulation.

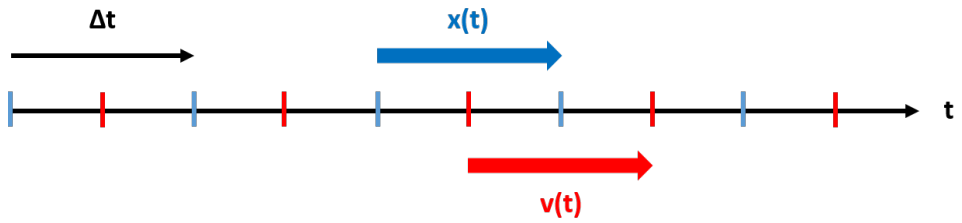

Figure 4.2: Leap frog. The position (blue) and the velocity (red) are calculated for each Δt (black) on a arbitrarly time scale

The position and velocity are not defined at the same time so the calculation of data like

kinetic, potential and total energy requires interpolation. However, the Leapfrog algorithm is symmetric in time but it is not able to start itself. There is the possibility to calculate the previous point from the latter. Moreover, there is no difference between terms that may induce numerical losses.

Velocity Verlet algorithm

This algorithm has been developed in order to compute the position and velocity [63] at the same times and it is self starting from given position and velocity. The plan is identical to the position Verlet except for the update of the velocity. In fact, the latter can be computed after the position. Moreover the calculations take an average value of forces applied into account at t and $t+\Delta t$. The Velocity Verlet algorithm is formalised as follow :

$$\begin{cases} x(t+\Delta t) = x(t) + v(t)\Delta t + \dfrac{(\Delta t)^2}{2} a(t) \\ \\ v(t+\Delta t) = v(t) + \dfrac{a(t)+a(t+\Delta t)}{2}\Delta t \end{cases} \tag{4.13}$$

By computing the position and the velocity at the same time, the phase space, which has x and v for coordinates, can be described. Moreover the data on the system energy are available by updating over the dynamics. By developing the Taylor expansion the technique minimizes the local truncation error at the third derivative. This allows modifications on velocity by scaling them up or down with a thermostat. The algorithm is applied by the following strategy. In the first step we compute a velocity v' half a time step ahead. Then $x(t+\Delta t)$ is calculated by this v' and to finish $v(t+\Delta t)$ is computed. During the treatment of position and velocity the forces are updated.

$$\begin{aligned} 1^\circ) \quad & v' = v(t) + \frac{1}{2}\Delta t \frac{d^2x(t)}{dt^2} \\ \\ 2^\circ) \quad & x(t+\Delta t) = x(t) + v'\Delta t \\ \\ 3^\circ) \quad & v(t+\Delta t) = v' + \frac{1}{2}\Delta t \frac{d^2x(t+\Delta t)}{dt^2} \end{aligned} \tag{4.14}$$

Choice of an algorithm

The Euler method is an algorithm used for teaching and demonstrating numerical techniques of integrating. But this method presents a lot of deficiencies like the adaptability of the time step which can bring on numerical errors. Verlet-like methods are symmetric which means that the trajectory is reversible in time ($t \to -t$). Conservation of total energy is not guarantee

for long time numerical simulations by accumulating errors on positions and velocities. Due to the dependence on local truncation and rounding errors, energy conservation is a guarantee on accuracy of integration and conservation of momenta (L,P). The velocity Verlet algorithm generates a trajectory which can instantaneously deviate from the exact trajectory. However, it has been shown that it conserves the volume of the explored phase space. This is why the Velocity Verlet algorithms are mostly used in the field of MD. Likewise, in this thesis work all the results from the simulations or numerical experiments presented here have been done with velocity Verlet integration. Indeed, it allows possibility to set a time step, an easy modifications of total energy and angular momentum.

4.4 Autocorrelation function

Autocorrelation function is an excellent tool which indicates on how much time the parameters are highly correlated or not. Its value is between -1 and 1 which respectively represents anti-correlation and correlation. The value of zero indicates a decorrelation between variables but this is not reciprocity because autocorrelation is an average on time.

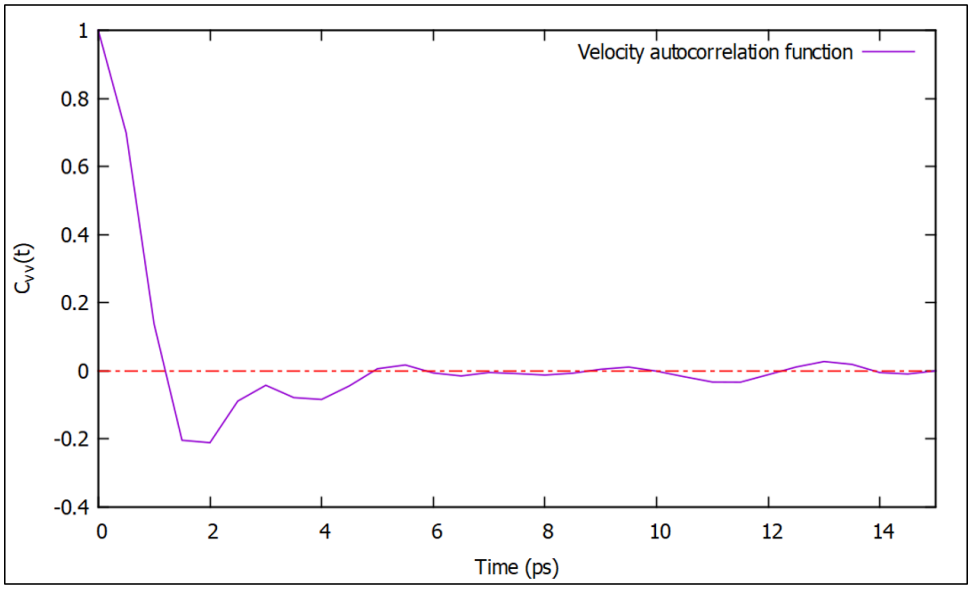

Figure 4.3: Velocity autocorrelation function obtained with CLUSTER code simulation of a HeND 2500

Figure 4.3 represents the velocity autocorrelation function of a simulation computed by the CLUSTER code for an HeND of 2500 atoms. At the beginning the velocities are completely correlated. Then the autocorrelation function oscillates one time before fading to zero. The minimum of the autocorrelation function can be considered as a collision between two atoms. The destroying of the oscillation is explained by the diffusive motion because after rebound-

ing the atoms migrate in the cluster. After 5 ps the system forgets the influence of the initial velocities. The expression of the autocorrelation for a A parameter is:

$$C_A(\tau) = \frac{\sum_i^N A_i(t)A_i(t+\tau)}{\sum_i^N A_i(t)A_i(t)} \tag{4.15}$$

where N is the number of points of autocorrelation function and τ a time step in relation to the calculated point. Autocorrelation functions are powerful tools which can be related to experimental spectra, transport coefficients and the dynamics in the fluid of interest.

4.5 Thermostat

Setting a temperature on a system implies to work in the canonical ensemble or NVT according to statistical mechanics. In these conditions, the system of interest (in contact with a heat bath), has a probability to be found in a energy state given by the Maxwell-Boltzmann distribution. The average squared velocity of the particle according to α=x,y,z in the large system can be calculated for a set temperature with N_{fd} degrees of freedom with the following relation:

$$k_B \mathrm{T} = \frac{m\langle v_\alpha^2 \rangle}{N_{fd}} \tag{4.16}$$

In MD, the setting of a temperature is done by a thermostat included in the software of the simulation.

4.5.1 Berendsen thermostat

The thermostat of Berendsen [64] presents some similarities with the Andersen thermostat [65]. In fact, the system interacts with a large heat bath in order to attain the aimed temperature by using non-explicit collisions but in a deterministic way by computing eq. (4.16) to evaluate the temperature at a given time t. A velocity correcting factor f_{corr} [66] is calculated and can be expressed as:

$$f_{corr} = \sqrt{1 + \frac{\Delta t}{\tau}\left(\frac{\mathrm{T}_{aim}}{\mathrm{T}} - 1\right)} = \sqrt{1 + \frac{\Delta t}{\tau}\left(\frac{N_{fd} k_B \mathrm{T}_{aim}}{\sum_{i,\alpha} m_i v_{i,\alpha}^2} - 1\right)} \tag{4.17}$$

τ is the relaxation time fixed by the user to allow more or less fast correction in accordance with virial theorem. However, the Berendsen thermostat is not recommended to simulate NVT

ensemble due to breaking of the virial theorem. The corrected velocity is $v_{corr} = f_{corr} v(t)$ which can be easily implemented in the Velocity Verlet algorithm when the system is equilibrating.

In our simulation of NVE ensemble, the temperature T is not explicitly used. The thermostat serves to set the total energy of the system close to the cluster experimental temperature. It is applied on all the equilibration phases of the MD calculations made in this thesis work.

4.6 Setting initial conditions

In our simulation the setting of the initial conditions for applying a special velocity to atoms needs a configuration file. It contains a complete list of particle positions and velocities at a time t. These configuration files are used to start the MD simulations and can be modified by internal and/or external programs to investigate physical phenomena we want to observe such as doping, photodissociation and cluster rotation or simply to store a spatial configuration. An example of the configuration file is given in Appendix D.1.

4.7 Application of an angular momentum

HeND evolves in a NVE ensemble so there is conservation of total energy, linear and angular momenta. Most trajectories were computed with L_{tot} = 0 and P_{tot} = 0. This is easily achieved by resetting all velocities to zero for a configuration which does not correspond to a potential minimum i.e a configuration with non-zero forces. The total energy can be increased back to a target value by velocity scaling without violating L_{tot} = 0 and P_{tot} = 0 conditions. Indeed, a simulation can be launched after resetting all velocities to zero according to α = x,y,z. The new configuration file shows velocities different to zero because of interacting forces between atoms and by scaling velocities with a factor f we obtain for P:

$$\begin{aligned} P_{tot,\alpha}(t) &= \sum_i m_i v_{i,\alpha}(t) = 0 \\ f P_{tot,\alpha}(t) &= \sum_i m_i f v_{i,\alpha}(t) = 0 \end{aligned} \tag{4.18}$$

likewise for L

$$\begin{aligned} \vec{L}_{tot,\alpha}(t) &= \sum_i m_i (\vec{r}_{i,\alpha} \times \vec{v}_{i,\alpha}(t)) = \vec{0} \\ f\vec{L}_{tot,\alpha}(t) &= \sum_i m_i (\vec{r}_{i,\alpha} \times f\vec{v}_{i,\alpha}(t)) = \vec{0} \end{aligned} \tag{4.19}$$

Initial random Maxwell-Boltzmann velocities lead to random L_{tot} and P_{tot}. These conditions are undesirable. A desired value for P_{tot} can be easily obtained by assigning random v_i to all particles but one and by assigning velocity components computed according to α = x,y,z to the

last particle. So that

$$\begin{aligned} \mathrm{P}_{N-1,\alpha} &= \sum_{i}^{N-1} m_i v_{i,\alpha} \\ v_{N,\alpha} &= \frac{\mathrm{P}_{tot,\alpha} - \mathrm{P}_{N-1,\alpha}}{m_N} \end{aligned} \tag{4.20}$$

By modifiying the rotational velocity of each atom of the cluster according to an axis of the Cartesian space in the laboratory framework and their center of mass, the global rotational motion of the HeND changes. To introduce the process the angular momentum of a system composed by many body [67–69] is given by :

$$\vec{\mathrm{L}} = \sum_i \vec{l_i} = \sum_i m_i \left(\vec{r}_i \times \vec{v}_i\right) = \mathrm{I}\vec{\omega} \tag{4.21}$$

Equation (4.21) can be written as:

$$\vec{\mathrm{L}} = \sum_i m_i \left[\vec{r}_i \times \left(\vec{\omega}_i \times \vec{r}_i\right)\right] = \mathrm{I}\vec{\omega} \tag{4.22}$$

Where I represents the tensor of inertia and ω the angular velocity then the rotational energy is equal to

$$E_{rot} = \frac{1}{2}\omega \mathrm{L} = \frac{1}{2}\mathrm{I}\omega^2 \tag{4.23}$$

The droplets are constituted by several elements which at a given moment can be considered as a rigid body of N-point particles of masses m_i. Then I can be written as a 3×3 matrices (Appendix B) where the diagonal elements can be expressed as:

$$\begin{aligned} \mathrm{I}_{xx} &= \sum_i m_i \left(y_i^2 + z_i^2\right) \\ \mathrm{I}_{yy} &= \sum_i m_i \left(x_i^2 + z_i^2\right) \\ \mathrm{I}_{zz} &= \sum_i m_i \left(x_i^2 + y_i^2\right) \end{aligned} \tag{4.24}$$

and the other elements are given by:

$$\begin{aligned} \mathrm{I}_{xy} &= -\sum_i m_i x_i y_i = \mathrm{I}_{yx} \\ \mathrm{I}_{xz} &= -\sum_i m_i x_i z_i = \mathrm{I}_{zx} \\ \mathrm{I}_{yz} &= -\sum_i m_i y_i z_i = \mathrm{I}_{zy} \end{aligned} \tag{4.25}$$

To impose a new angular momentum $\vec{\mathrm{L}'}$ to the system the velocity of each helium atoms is modified by adding to the original angular velocity the difference between the target and the actual angular velocity of the atoms to attain the desired angular momentum. By using eq.

(4.22) the new angular momentum can be expressed as:

$$\vec{\mathrm{L}}' = \sum_i m_i \left[\vec{r}_i \times \left(\vec{\omega} \times \vec{r}_i + \left[\vec{\omega}' - \vec{\omega} \right] \times \vec{r}_i \right) \right] = \mathrm{I}\vec{\omega}' \tag{4.26}$$

where

$$\vec{\Delta} v_i = \left[\vec{\omega}' - \vec{\omega} \right] \times \vec{r}_i \tag{4.27}$$

so that

$$\vec{\mathrm{L}}' = \sum_i \vec{l}_i = \sum_i m_i \left[\vec{r}_i \times \left(\vec{v}_i + \vec{\Delta} v_i \right) \right] \tag{4.28}$$

Chapter 5

Interaction potentials

5.1 MD interaction potentials

The MD simulations in this work are carried out using two types of potentials, namely the Lennard-Jones potential [70] and the Morse potential [71].

5.1.1 Lennard-Jones potential

The Lennard-Jones potential is a two-parameter function commonly used to describe the interaction between two neutral particles that are weakly bound, like noble gas atoms. The mathematical expression of this kind of potential as a function of the distance r between the atoms is given by:

$$V(r) = 4\varepsilon_0 \left[\left(\frac{r_e}{r} \right)^{12} - 2 \left(\frac{r_e}{r} \right)^{6} \right] \tag{5.1}$$

where ε_0 is the well depth and r_e is the equilibrium distance. For short distances ($r \to 0$) $V \to \infty$, the atoms are subject to the repulsion because there is electronic overlap. In eq. (5.1), the repulsive term is represented by $(1/r)^{12}$. At the minimum of energy, the interacting atoms are stable. From the minimum of energy to the asymptote V $\to 0$ the atoms are stabilised and attracted by the London dispersion represented mathematically by $(1/r)^6$. In fact at long range, the dispersion interaction arises from the attraction between a fluctuating dipole and a dipole induced by the electric field of this instantaneous dipole which leads to $(1/r)^6$ dependence. An example of Lennard-Jones potential is shown in Figure 5.1.

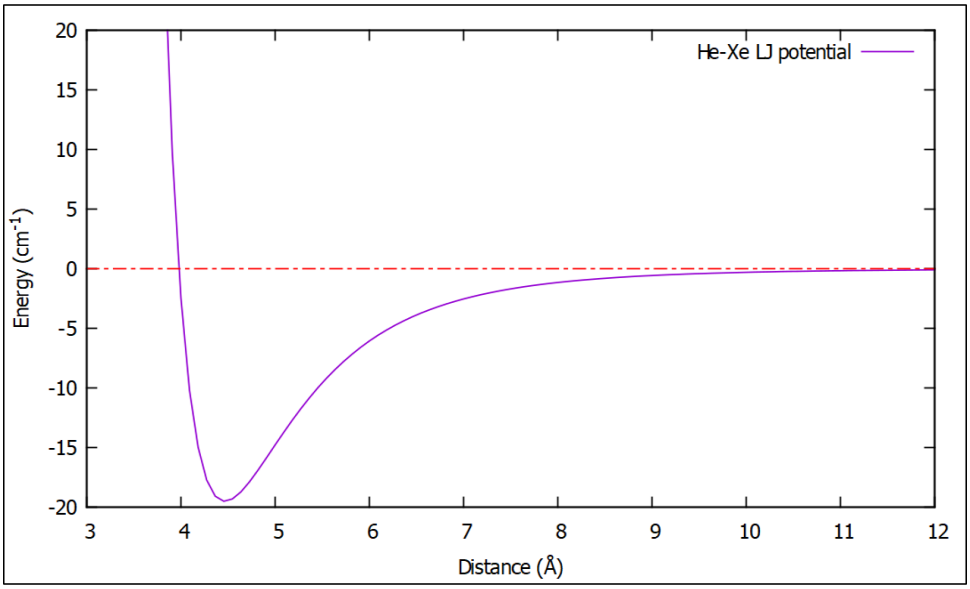

Figure 5.1: He-Xe Lennard-Jones potential

For some simulations of dopant impacts and aggregation, the Lennard-Jones potential was used because those calculations involve electronically neutral atoms of argon, helium, iodine, krypton and xenon. The parameters ε and r_e are given in Table A.1 in the Appendix A.

5.1.2 Morse potential

The Morse potential is an interatomic potential which models diatomic molecule interactions. In fact, it models the fragmentation and the vibration of molecules in bound and unbound state according to the quantum mechanics. It is mathematically expressed as:

$$V(r) = D_e \left[1 - e^{-a(r-r_e)}\right]^2 \tag{5.2}$$

Where a is a parameter expressed as a function of the force constant of the molecular bond k and D_e is the well depth (from the mathematical minimum) of the Morse potential function. The parameter is expressed as $a = \sqrt{k/(2D_e)}$. r_e is the equilibrium distance of the atoms in the molecule. Globally, this is a better approximation compared to the quantum harmonic oscillator for describing the vibrational motion of molecules. This potential has been chosen to model the interaction inside molecular iodine which undergoes the photodissociation and then can vibrate or dissociate into two iodine atoms. Morse potential parameters are described in Table A.2 in Appendix A. The choice of an effective potential for the helium-helium interaction is motivated by the fact that at 0.5 K with quantum effective potential the nanodroplet is less rigid than Lennard-Jones potential. Indeed, Figure 5.2 shows mean squared displacement for Morse potential V_{Morse}(D_e = 0.8 cm^{-1}; r_e = 4.0 Å; a = 1.1 $Å^{-1}$) and Lennard-Jones potential

$V_{LJ}(\varepsilon = 0.8\,\mathrm{cm}^{-1}; r_e = 4.0\,\text{Å})$ over 100 ps. During this computed time, helium atoms positions fluctuate more from their reference positions under V_{Morse} than under V_{LJ}. In fact, the deviation of positions for V_{Morse} attains 30,000 pm^2 ($\simeq$ 1.73 Å) and 10,000 pm^2 ($\simeq$ 1.00 Å) after 100 ps.

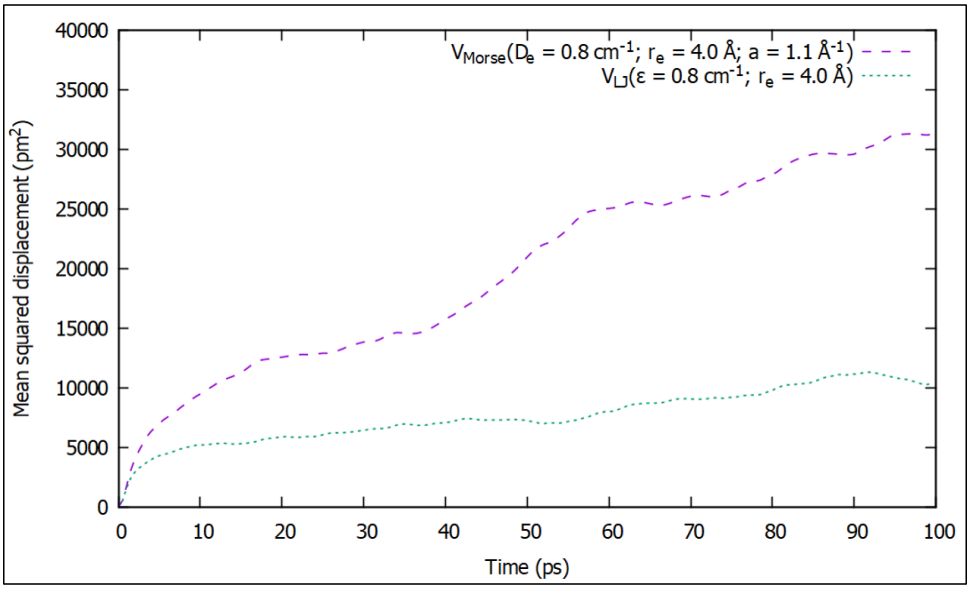

Figure 5.2: Mean squared displacement of atoms in HeND 2500 for Morse and Lennard-Jones potentials

5.2 The effective He-He potential

5.2.1 Idea of effective potential

The idea of effective potential in MD is well known. From the works of Feymann and Hibbs [72, 73], who proposed this concept, quantum effects can be partially included in classical simulations. Indeed, works on neon and water [74, 75] computed potentials by this technique. Another example is to take the ground state from quantum calculations as classical potential minimum, which means that potentials computed by quantum calculations are deeper than classical potentials.

This idea of effective potential can be applied by a convolution of classical potentials with probability densities of interacting atoms. To achieve that, atom wave functions have to be defined for helium atoms in our case. In fact, using the wave-particle duality and particularly the de Broglie wavelength allows to determine the amplitude of delocalisation of an atom. This wavelength is expressed as follows:

$$E = h\nu = \frac{hc}{\lambda} = pc \Leftrightarrow \lambda = \frac{h}{p} \tag{5.3}$$

Then the relation between k, the norm of the wave function, and the de Broglie wavelength λ in 1D is:

$$k = \frac{2\pi}{\lambda} = \frac{mv}{\hbar} \tag{5.4}$$

According to the equipartition theorem the average kinetic energy of a particle in an equilibrated system is expressed by the degree of freedom N_{fd}, the Boltzmann constant k_b and the temperature T :

$$E_k = \frac{N_{fd}}{2} k_b T \tag{5.5}$$

The relationship between the momentum and the kinetic energy is given by :

$$E_k = \frac{p^2}{2m} \tag{5.6}$$

By using eqs. (5.5), (5.6) and (5.3) the general expression of the de Broglie wavelength for a particle with N_{fd} degrees of freedom is given by :

$$\lambda = \frac{h}{\sqrt{N_{fd} m k_B T}} = \frac{2\pi\hbar}{\sqrt{N_{fd} m k_B T}} \tag{5.7}$$

Using eq. (5.7), helium atoms are delocalised over a distance of 6 Å at T = 0.5 K which is the same order of magnitude as the average distance between helium atoms in HeND. Overlapping of presence density contributes to show a non-crystalline structure according to the pair correlation function of He-He which qualifies HeND like a quantum liquid.

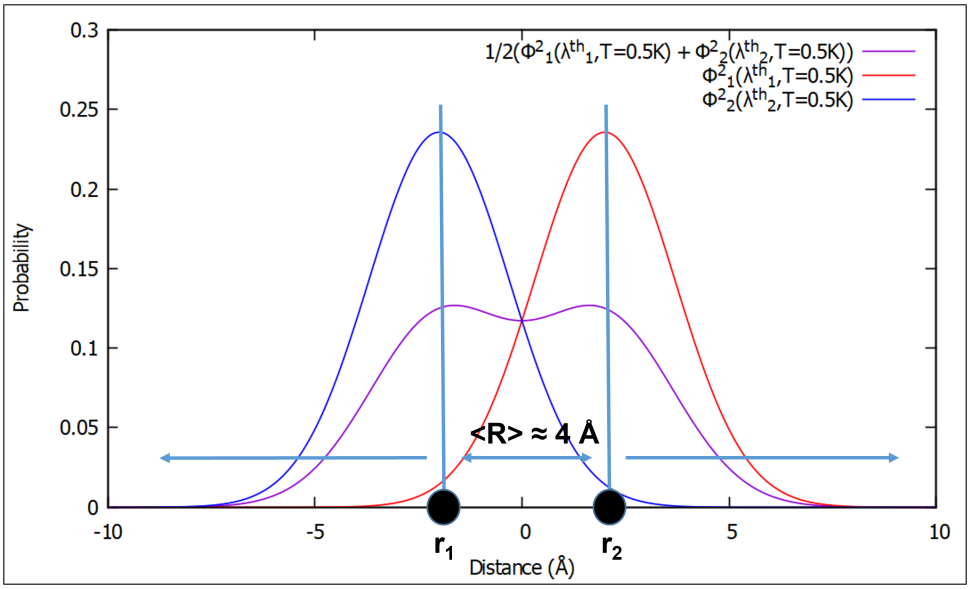

Figure 5.3: Presence probability of two helium atoms in 1D at T = 0.5 K. Blue and red curves are normalised presence densities for each atom and purple curve represents the normalised density probability for both atoms.

This is illustrated in Figure 5.3 where black points represent helium atoms with their own presence probabilities in the hypothesis of free particles where there are no interactions between them. It also shows the resulting probability of presence of two particles like helium atoms with overlap of their own probabilities of presence ϕ_i^2. The wave function of each helium atom is the product between the plane wave function $\exp(ikz)$, where k is defined in eq. (5.4), and $P(k)$ the Maxwell-Boltzmann distribution because atoms have no precise velocities. Then the expression of ϕ_i over 1D is given by:

$$\phi_i(z) = \int_{-\infty}^{+\infty} P(k) exp(ikz)\,\mathrm{d}k \tag{5.8}$$

$\phi_i(z)$ is a superposition of plane waves $exp(ikz)$ with weights $P(k)$ where the Maxwellian distribution function in the z direction is given by:

$$P(v_z) = \left(\frac{m}{2\pi k_B T}\right)^{1/2} \exp\left(-\frac{mv_z^2}{2k_B T}\right) \tag{5.9}$$

Eq. (5.9) has to be modified according to eq. (5.3) in order to get the wave vector k as parameters:

$$k = \frac{2\pi}{\lambda} \tag{5.10}$$

Then the relationship between k and v is given by :

$$k = \frac{2\pi mv}{h} = \frac{mv}{\hbar} \tag{5.11}$$

Now a variable transformation can be done for incorporating it in eq. (5.8):

$$\mathrm{d}k = \frac{m}{\hbar}\mathrm{d}v \tag{5.12}$$

Likewise from eq. (5.11) the squared velocity in eq. (5.9) can be written as:

$$v^2 = \frac{\hbar^2 k^2}{m^2} \tag{5.13}$$

Using the previous expressions, eq. (5.8) can be expressed as:

$$\phi_i(z) = \frac{m}{\hbar}\left(\frac{m}{2\pi k_B T}\right)^{1/2} \int_{-\infty}^{+\infty} \exp\left(-\frac{\hbar^2 k^2}{2mk_B T}\right) \exp(ikz)\,\mathrm{d}k \tag{5.14}$$

Rewritten as:

$$\phi_i(z) = \frac{m}{\hbar}\left(\frac{m}{2\pi k_B T}\right)^{1/2} \int_{-\infty}^{+\infty} \exp\left(-\frac{\hbar^2 k^2}{2mk_B T} + ikz\right) \mathrm{d}k \tag{5.15}$$

Previous eq. (5.15) can be written to make an easy recognition of a remarkable identity. To simplify the terms in the exponential parts a variable named A is introduced as:

$$\begin{gathered} -\frac{\hbar^2 k^2}{2mk_BT} + ikz \\ A = \frac{\hbar^2}{2mk_BT} \end{gathered} \tag{5.16}$$

Then a factorisation can be done according to the following expressions:

$$-A\left[k^2 - \frac{iz}{A}k\right] \tag{5.17}$$

Eq. (5.17) shows a incomplete remarkable identity of the form $(a-b)^2$. An identification of a and b has to be done as follows:

$$\begin{cases} a^2 = k^2 \\ \\ 2ab = \dfrac{ikz}{A} \end{cases} \Leftrightarrow \begin{cases} a = k \\ \\ b = \dfrac{iz}{2A} \end{cases} \tag{5.18}$$

The remarkable identity showed is not completed. So the expression can raise the following formulas:

$$-A\left[k^2 - \frac{iz}{A}k + \left(\frac{iz}{2A}\right)^2 - \left(\frac{iz}{2A}\right)^2\right] \tag{5.19}$$

Rewritten as:

$$-A\left[\left(k - \frac{iz}{2A}\right)^2 + \frac{z^2}{4A^2}\right] = -A\left(k - \frac{iz}{2A}\right)^2 - \frac{z^2}{4A} \tag{5.20}$$

Now with eq. (5.20) incorporated into eq. (5.15) taking the simplification in eq. (5.16) into account gives:

$$\phi_i(z) = \frac{m}{\hbar}\left(\frac{m}{2\pi k_BT}\right)^{1/2} \int_{-\infty}^{+\infty} \exp\left(-A\left[k - \frac{iz}{2A}\right]^2 - \frac{z^2}{4A}\right) dk \tag{5.21}$$

Rewritten as:

$$\phi_i(z) = \frac{m}{\hbar}\left(\frac{m}{2\pi k_BT}\right)^{1/2} \int_{-\infty}^{+\infty} \exp\left(-A\left[k - \frac{iz}{2A}\right]^2\right) \exp\left(-\frac{z^2}{4A}\right) \mathrm{d}k \tag{5.22}$$

The wave function of free particles depends on a gaussian form indepedent of k so the expres-

sion is given as:

$$\phi_i(z) = \frac{m}{\hbar}\left(\frac{m}{2\pi k_B T}\right)^{1/2} \exp\left(-\frac{z^2}{4A}\right) \int_{-\infty}^{+\infty} \exp\left(-A\left[k - \frac{iz}{2A}\right]^2\right) \mathrm{d}k \tag{5.23}$$

Then the probability of presence which is the square is given by:

$$\phi_i^2(z) = \left(\frac{m}{\hbar}\right)^2 \left(\frac{m}{2\pi k_B T}\right) \exp\left(-\frac{z^2}{2A}\right) \left(\int_{-\infty}^{+\infty} \exp\left(-A\left[k - \frac{iz}{2A}\right]^2\right) \mathrm{d}k\right)^2 \tag{5.24}$$

The interesting part is the exponential one where the thermal de Broglie wavelength appears by using eq. (5.7). The expression is presented as:

$$\exp\left(-\frac{z^2}{2A}\right) = \exp\left(-z^2 \frac{m k_B T}{\hbar^2}\right) \tag{5.25}$$

By taking the square of eq. (5.7) the formula is:

$$\lambda^2 = \frac{4\pi^2 \hbar^2}{N_{fd} m k_B T} \Leftrightarrow \frac{\hbar^2}{m k_B T} = \frac{N_{fd} \lambda^2}{4\pi^2} \tag{5.26}$$

Then the thermal de Broglie wavelength can appears in the eq. (5.25) for giving:

$$\exp\left(-z^2 \frac{m k_B T}{\hbar^2}\right) = \exp\left(-z^2 \frac{4\pi^2}{N_{fd} \lambda^2}\right) \tag{5.27}$$

The probability of presence of the eq. (5.24) can be expressed as:

$$\phi_i^2(z) \sim \exp\left(-z^2 \frac{4\pi^2}{N_{fd} \lambda^2}\right) \tag{5.28}$$

This function depends on the de Broglie wavelength which represents the ability of delocalisation of a particle at a given temperature. But the hypothesis of free particle does not include the He-He interactions in the process which is an important aspect in simulations.

5.2.2 Quantum effective potential and Zero Point Average Dynamics (ZPAD)

The strategy is to create an effective potential which takes moderate quantum effects of liquid helium and He-He interactions into account. An iterative process builds the effective potential $V_{eff}(R_{12})$ based on the double convolution of the classical He-He potential at first then combined with the probability of presence of the two helium atoms. Figure 5.4 presents how the He-He effective potential is built. The mathematical expression of the effective potential used

in MD is given as :

$$V_{eff}(R_{12}) = \int\int V_{12}(S)\Phi_1^2(r_1)\Phi_2^2(r_2)\mathrm{d}r_1\mathrm{d}r_2 \tag{5.29}$$

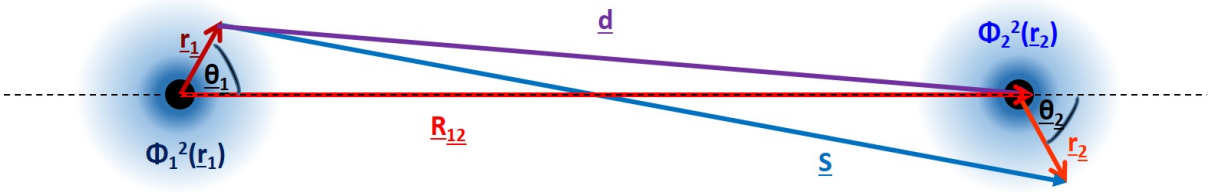

Figure 5.4: Model of the construction of the effective potential He-He

The S can be calculated according to the following conditions :

$$\begin{aligned} \vec{R_{12}} &= \vec{r_1} + \vec{d} \Leftrightarrow \vec{d} = \vec{R_{12}} - \vec{r_1} \\ \vec{S} &= \vec{d} + \vec{r_2} \Leftrightarrow \vec{S} = \vec{R_{12}} - \vec{r_1} + \vec{r_2} \end{aligned} \tag{5.30}$$

Taking the previous relationship in eq. (5.30) between vectors the eq. (5.29) can be rewritten as :

$$V_{eff}(\vec{R_{12}}) = \int\int V_{12}(\vec{R_{12}} - \vec{r_1} + \vec{r_2})\Phi_1^2(\vec{r_1})\Phi_2^2(\vec{r_2})\mathrm{d}r_1\mathrm{d}r_2 \tag{5.31}$$

This technique does not explicitly use the zero point energy (ZPE), the solvent density and the pair correlation function. An iterative method was developed by Slavicek, Jungwirth, Lewerenz, Nahler, Farnik and Buck where each helium atom position is replaced by their probability of presence $\Phi_i^2(r_i)$ [54]. Then the calculation starts with a classic He-He potential $V_{cl}(R)$ = $V_{q,0}(R)$ where R = |**R**| is the He-He distance. The process is repeated until V_{eff} does not change anymore. The process is self-consistent. The first objective is to get a pair correlation function $P_n(R)$ with MD where we make the calculations with a classical potential $V_{q,0}(R)$. The second step is the convolution of the pair correlation function $P_n(R)$ previously obtained with the density of the last step of the atom to get a quantum pair correlation function.

$$P_{q;n+1}(|r'|) = \int P_n(|r|)\Phi_n^2(|r - r'|)\,\mathrm{d}r' \tag{5.32}$$

The third step is the construction of the radial potential taking the quantum pair correlation function $P_{q;n}$ with the classical potential $V_{cl}(R)$ illustrated in Figure 5.5.

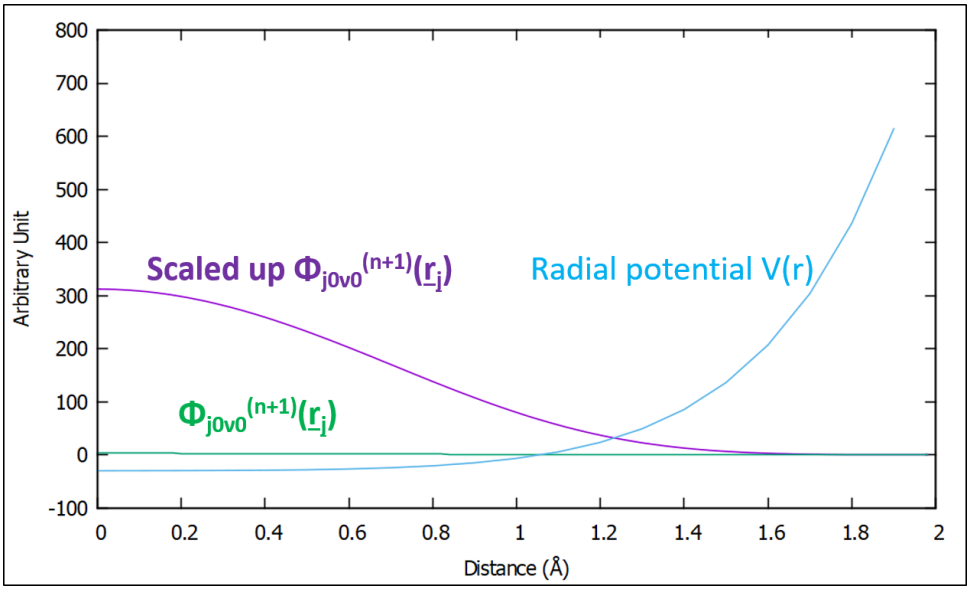

Figure 5.5: Model of construction of the quantum pair correlation function He-He

$$V_{rad;n+1}(|r_i|) = \int V_{cl}(|r - r_i|) P_{q;n+1}(r)\,\mathrm{d}r \tag{5.33}$$

The fourth stage is the resolution of the Schrödinger equation from $V_{rad;n+1}$ by Vibvar code [76] to find the wave functions Φ_{n+1}(r) for each particle in the mean field of others. The finalisation of the machinery is the convolution of the effective potential with the quantum distributions.

$$V_{q,n+1}(R_{12}) = \int\int V_{cl}(|R_{12} - r_1 + r_2|)\Phi^2_{n+1;1}(|r_1|)\Phi^2_{n+1;2}(|r_2|)\,\mathrm{d}r_1\,\mathrm{d}r_2 \tag{5.34}$$

Repeating the ZPAD self-consistent process by starting from a classical description of the He-He potential where the well depth is overestimated and the equilibrium distance is underestimated takes a dozen of cycles, which depends on the criterion for convergence. Figure 5.6 shows the third, fifth and twelfth ZPAD iteration.

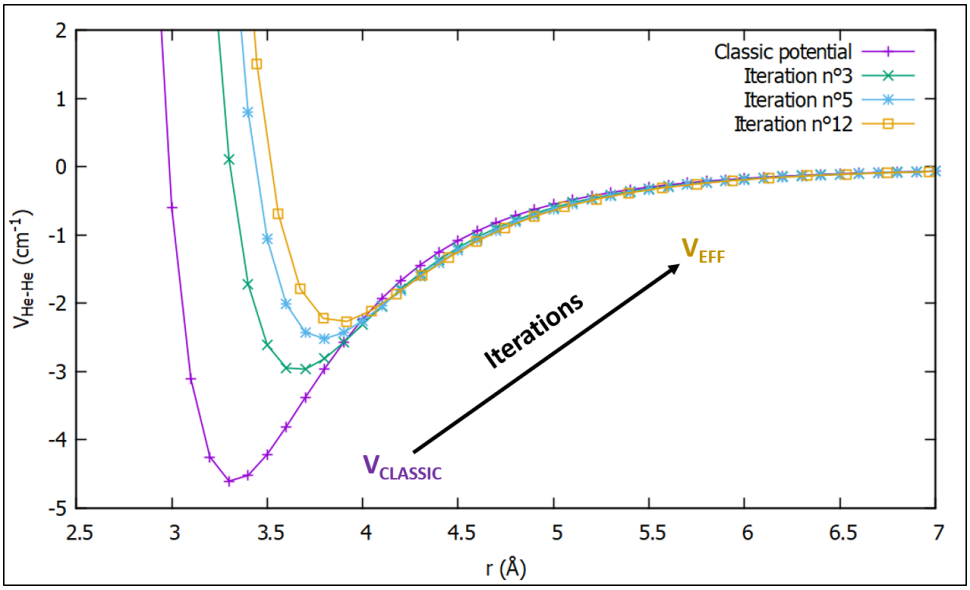

Figure 5.6: ZPAD potential construction with He2500

The effective interaction potential obtained has a well depth of 2.27 cm^{-1} and gives a helium density of 0.022 $He.Å^{-3}$. This well is still too attractive such that over long simulation HeND becomes solid at 0.5 K. Moreover, the helium evaporative energy for this potential is higher than the experimental value of 5 cm^{-1} [77]. To resolve this, an adjustment has been made and the simulations use a Morse potential with r_e = 4.1 Å, D_e = 0.8 cm^{-1} and a = 1 $Å^{-1}$. This potential is approximately close to the experimental value of the helium evaporative energy and needs a correction to be closer which motivates to look for another potential. Despite all, this Morse potential will be used for the numerical experiment with the new one described in the following chapter.

5.3 Computation of the 3D density

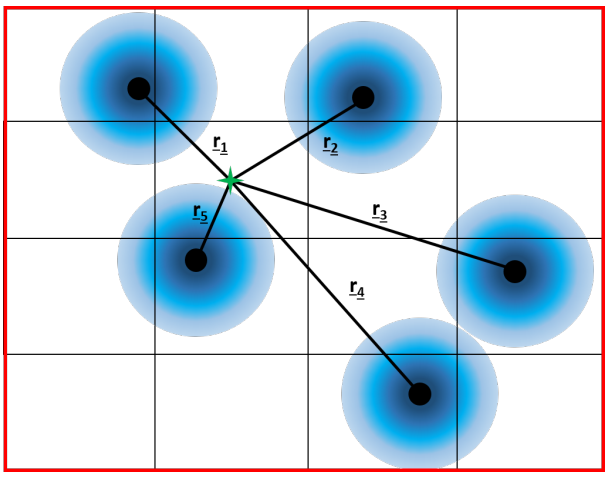

Figure 5.7: Boxes and density of helium atom

The goal is the transformation of a classical point density into a smooth 3D density by integrating over all the atom contributions and taking into account their delocalisations with the helium wave function at the ground state. The 3D density could be visualised by graphic tools from fluid dynamics or MD. We currently visualise the droplets with VMD [78]. Considering the quantum nature of helium at very low temperature the representation as balls and points is not realistic. The idea is built on the use of boxing. The program BOXANDENSITY has been written during this thesis. It works by determining the edges of the nanodroplets to define a master box which is subdivided into a certain number of smaller boxes. The master box is represented in red in the Figure 5.7 itself divided in mini-boxes. The center of the minibox which is defined as a point of convergence to avoid the risk to not take into account an atom in the corner of the red box. The estimation of the number of atoms is made by the probability of presence $\phi^2_{j0v0}(r_i)$ in each minibox j in masterbox i of volume V and it is calculated as:

$$N_{He} = \sum_i \sum_j \phi^2_{j0v0}(r_{i,j}) V^{minibox}_{i,j} \tag{5.35}$$

The project has not been pushed forward and remains a basis for starting a kind of specific visualisation software.

5.4 The chemical potential of HeND

5.4.1 Heat of vaporisation

The study of the vapor pressure of ^{4}He motivated the creation of an international standard for thermometry in a range of temperature from 1 to 5.2 K. In fact, the first measurements of thermodynamic temperature in the cited range were made with gas thermometers filled with ^{4}He in liquid helium. This permitted to determine vapor pressure-temperature relation [79]. This convention was adopted in the 1958 ^{4}He Vapor Pressure Scale of Temperatures according to the experimental works of the Kamerlingh Onnes laboratory in Leiden and the U.S. Naval Research Laboratory in Washington on the helium vapor pressure. According to those data, a table of vapor pressure of ^{4}He was written and with the relation between vapor pressure-temperature the heat of vaporisation, at T = 0 K, was calculated yielding μ = 59.62 J/mol [80] which represents about 5 cm^{-1}. Within the liquid drop model [81] the energy $E(N)$ of a droplet with N particles is expressed as:

$$E(N) = a_v N + a_s N^{2/3} + a_c N^{1/3} \tag{5.36}$$

Where the only interest resides in the volumic coefficient a_v which describes the minimal energy to apply to the system for evaporating an element from its ensemble. a_s and a_c are respectively the surface coefficient, related to the surface tension, and the curvature coefficient.

The objective of the following work was to reshape the effective potential used for temperature around 0.5 K with the Morse potential parameters of Table A.2, particularly the well depth, to get a chemical potential closer to the experimental conditions of work where the temperature is around 0.37 ± 0.05 K [35].

Two methods have been used and are presented in the following section to adjust the effective potential to reproduce the average evaporation energy of 5 cm^{-1} at the experimental temperature. The first one is a small MC calculation by averaging the total energy of a helium atom randomly picked. The second method is an series of calculations of the total energy for different sizes of HeND.

5.4.2 Methodology

Determination of $\mu(N)$ by MC

The chemical potential μ is the minimum energy required to remove an atom from its ensemble. This variable is related to thermodynamics. Indeed, internal energy U for a multiple component

system according to μ is expressed as:

$$\mathrm{d}U = \mathrm{T}\mathrm{d}S - P\mathrm{d}V + \sum_i \mu_i \mathrm{d}N_i \tag{5.37}$$

where T is the temperature, S the entropy, P the pressure, V the volume, μ_i the chemical potential and N_i the number of particle. Because the HeND is considered as a closed system at constant temperature and pressure, the Gibbs free energy G is used as the thermodynamic variable to represent the system. The expression of G is:

$$G = H - TS = U + PV - TS \tag{5.38}$$

The derivative of G is expressed as:

$$\mathrm{d}G = \mathrm{d}U + P\mathrm{d}V + V\mathrm{d}P - T\,\mathrm{d}S - S\mathrm{d}T \tag{5.39}$$

Using eq. (5.37) in eq. (5.39), G can be expressed as:

$$\mathrm{d}G = V\mathrm{d}P - S\mathrm{d}T + \sum_i \mu_i \mathrm{d}N_i \tag{5.40}$$

so that the chemical potential μ_i at constant temperature and pressure is given by :

$$\mu_i = \left(\frac{\partial G}{\partial N_i}\right)_{P,T} \tag{5.41}$$

Eq. (5.41) shows that the difference in free energy between the HeND_N and HeND_{N-1} is the chemical potential. In order to study this phenomenon a program of MC based on the uniform pseudo-random numbers described in chapter 7 has been programmed. Considering the method to create pseudo-random numbers, each cycle of MC on a HeND uses a maximum number of 30 uniform random numbers. By picking a random helium atom and calculating its total energy contribution in the system HeND and making an average of energy on all the atom chosen, a chemical potential can be estimated. The main problem with this method was the fact that by removing one helium atom the chemical potential was biased. In fact, the system need a time of relaxation which is not allowed in this small MC calculations. To illustrate this, a MC calculation, with the potential V(D_e = 0.80 cm^{-1}; r_e = 4.1 Å; a = 1 $\mathrm{Å}^{-1}$) by removing only surface atoms, has been made on a He_{2500} giving $\mu(\mathrm{He}_{2500}) \simeq 10.40\,\mathrm{cm}^{-1}$ which is an overestimation of the chemical potential.

Determination of $\mu(N)$ by MD

To resolve the bias in chemical potential cited in the previous section, a strategy with the MD has been chosen by fitting the computed total energy of different HeND sizes according to eq. (5.36) by Levenberg-Marquardt method. The definition of the size is the number of helium atoms which composes the droplets. The study has been realised on a range of HeND size from He_0 to He_{9000} starting from the potential in Table A.2 at 0.5 K and by adjusting the well depth to get closer to the $5\,cm^{-1}$ of chemical potential.

The strategy is to deduce the chemical potential μ by calculating the total energy for different sizes of HeND. This principle is based on the following formula considering eq. (5.41) where $\Delta N = 1$:

$$\mu = \frac{E(N+1) - E(N)}{\Delta N} \tag{5.42}$$

Then a fitting on the collected total energy gives the chemical potential according to eq. (5.36). The protocol for the MD starts from a pure HeND configuration file containing 9000 atoms, obtained by successive merging of smallest droplets by MD, where their Cartesian position and velocity coordinates are written from the nearest to the farthest atom to the center of mass of the HeND. Then the selection of the droplet size is done by choosing the number of atoms taken into account in the calculation by removing the farthest atom. Then a phase of equilibration at 0.5 K simulating a physical time of 1 ns with a time step of 10 fs and 100,000 time steps is run. This process ensures a good energy stabilisation of the nanodroplet and uncorrelated atoms velocities. This step of computing is repeated a second time. The last phase of the protocol is done by a constant energy simulation with time simulated of 1 ns with a time step of 10 fs and 100,000 time steps. The Morse potential computed is V($D_e = 0.80\,cm^{-1}$; $r_e = 4.1$ Å; a = $1\,Å^{-1}$) after ZPAD potential adjustment. The trajectories are integrated with a velocity Verlet algorithm. The relative energy fluctuation of the simulation is about 10^{-7} which shows excellent energy conservation along the calculations. At the end, the simulation the CLUSTER code computes the kinetic, potential and total energy of the system E(N). The energy system is collected for determining the chemical potential for several HeND sizes.

The Levenberg-Marquardt fitting of the different total energies of the pure HeND over different size ranges from 0 to 9000 atoms gives $\mu \simeq 6.149 \pm 0.022\,cm^{-1}$ at 0.5 K which shows that the chemical potential is somewhat overestimated. In order to resolve this latter bias, the only way is to reduce the well depth, D_e, by adjustment of the Morse potential and by keeping the same equilibrium distance ,r_e, in order to conserve the density of the helium droplet which is about $0.023\,He/Å^3$ and with the same a parameters. The tested Morse potentials at experimental temperature of 0.37 K are:

- V(D_e = 0.55 cm^{-1}; r_e = 4.1 Å; a = 1 $Å^{-1}$)
- V(D_e = 0.63 cm^{-1}; r_e = 4.1 Å; a = 1 $Å^{-1}$)
- V(D_e = 0.65 cm^{-1}; r_e = 4.1 Å; a = 1 $Å^{-1}$)
- V(D_e = 0.68 cm^{-1}; r_e = 4.1 Å; a = 1 $Å^{-1}$)

The results presented in Table 5.1 are those coming from the potential V(D_e = 0.65 cm^{-1}; r_e = 4.1 Å; a = 1 $Å^{-1}$) which gives a chemical potential $\mu \simeq 5.565 \pm 0.426\,cm^{-1}$ at 0.37 K. The size range for the fit is He_{357} to He_{4749}. The data have been fitted with the Levenberg-Marquardt method and the results give for the volume parameter $\mu \simeq$ - $5.565 \pm 0.426\,cm^{-1}$ which is the chemical potential, for the surface parameter $a_s \simeq 20.59 \pm 10.99\,cm^{-1}$, related to surface tension, and the curvature parameter $a_c \simeq$ - $53.01 \pm 69.03\,cm^{-1}$. The value of the found chemical potential in this study does not correspond exactly to the experimental value but considering the other results for the different Morse potential, it is the best one:

- V(D_e = 0.55 cm^{-1}; r_e = 4.1 Å; a = 1 $Å^{-1}$) the chemical potential is equal to $a_v \simeq$ - $4.016 \pm 0.109\,cm^{-1}$ which is too low.
- V(D_e = 0.63 cm^{-1}; r_e = 4.1 Å; a = 1 $Å^{-1}$) the chemical potential is equal to $a_v \simeq$ - $4.698 \pm 0.935\,cm^{-1}$ which is slightly too low.
- V(D_e = 0.68 cm^{-1}; r_e = 4.1 Å; a = 1 $Å^{-1}$) the chemical potential is equal to $a_v \simeq$ $5.717 \pm 0.193\,cm^{-1}$ which is too high.

The best well depth for a temperature near 0.37 K is 0.63 $cm^{-1} < D_e <$ 0.65 cm^{-1}.

HeND size (Number of He)	**Total energy (cm^{-1})**
0	0
357	- 1323.340
710	- 2726.695
1000	- 4027.288
1299	- 5418.163
1822	- 7755.408
2462	- 10685.26
2643	- 11484.67
3034	- 13513.31
3439	- 15125.27
3891	- 17051.44
4244	- 18862.91
4749	- 21738.18

Table 5.1: Total energy of HeND depending on their size for He-He Morse potential V(D_e = 0.65 cm^{-1}; r_e = 4.1 Å; a = 1 $Å^{-1}$)

The first observation is that the total energy in absolute value increases with the droplet size increases because the more there are helium atoms in the cluster the more there are interactions and stabilisation of the ensemble. The convention adopted in the CLUSTER code is that all energies are measured relative to E = 0 cm^{-1} corresponding to total dissociation such that a bound state always has E < 0 cm^{-1}. Figure 5.8 plots the data in Table 5.1 and DMC calculations which compute parameters [76] of eq. (5.36). The calculated Morse potential V(D_e = 0.65 cm^{-1}; r_e = 4.1 Å; a = 1 $Å^{-1}$) slightly overestimated the DMC parameter calculations.

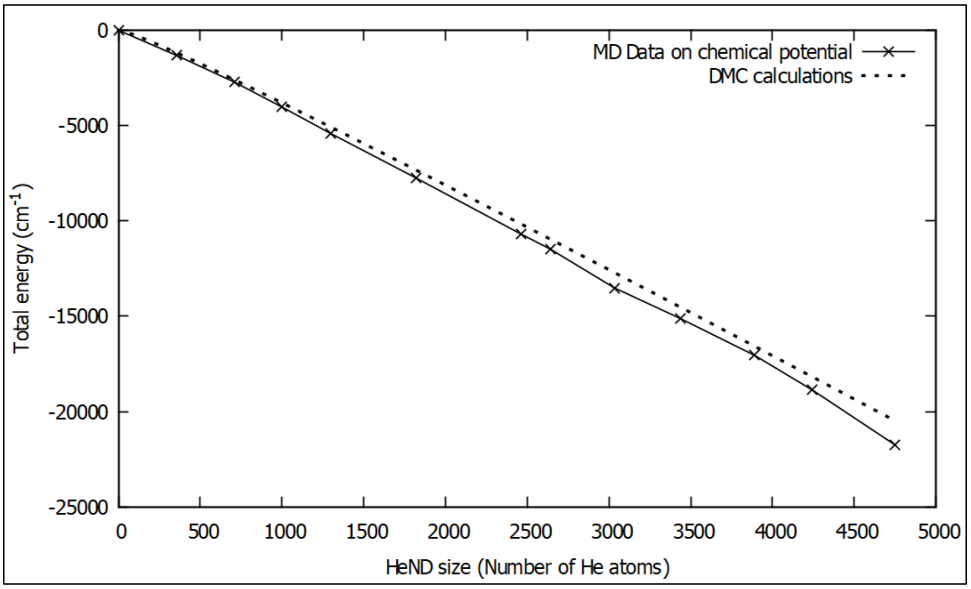

Figure 5.8: Total energy vs droplet size for calculated Morse potential V(D_e = 0.65 cm^{-1}; r_e = 4.1 Å; a = 1 $Å^{-1}$) and DMC calculations

The chemical potential coming from this calculation satisfies our criterion of maintaining a liquid helium droplet at 0.37 K despite the fact that it is not exactly equal to 5 cm^{-1}. Further refinements could be made by a more complete exploration of the droplet size range.

Chapter 6

Fragment analysis by Complete Clustering Algorithm

An angular momentum applied to a HeND gives different outcomes on the structure of the object of interest due to centrifugal force. Indeed, multiple fragmentations occur in space throughout HeND rotational experiments giving a certain amount of subdroplets composed of N atoms. In order to identify and quantify their number a Complete clustering algorithm (CCA) was programmed during this thesis work for fragment analysis. The goal is to construct a network based on binary atom relations according to data science which is known as "clustering". Here, the relation is based on neighbouring. This algorithm is named "complete" because of the fact that each atom is part of a network. Then a connectivity graph can be elaborated to show the networks and the relations between atoms.

The idea of "clustering" can be illustrated by Figure 6.1 which shows three groups of atoms. Here, the criterion of clustering is the distance between atoms. They are considered as neighbours and part of a same cluster if dotted circles intercross. Indeed, the latter represent a cutoff distance based on pair correlation function.

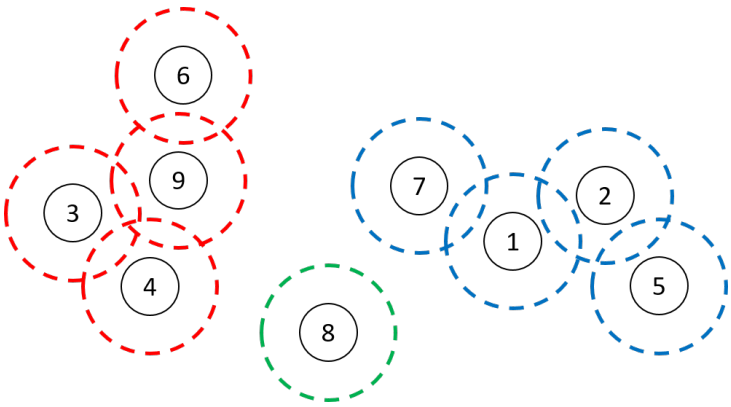

Figure 6.1: 2D example of atom cluster

It is shown that an atom can be a cluster if there are no neighbours in its environment like atom 8. Figure 6.2 represents the connectivity graph based on the "clusters" in Figure 6.1. The algorithm obeys to the depth-first logic to construct the tree. Figure 6.2 shows the path of the CCA with a color code. The red arrow is for selecting the first neighbour in terms of neighbouring distance (Cluster 1, atom 2). Then the algorithm finds the first neighbour of the first previous choice (atom 1). If the found atom is already discovered, in grey, then the green arrow indicates that the algorithm has to go back to the previous level. It looks for the second choice, represented by the blue arrow, which means the second neighbour in terms of distance (atom 5). If all the atoms in this group have already been visited the "cluster" is complet and the algorithm choose an atom that is not already in a cluster (atom 3).

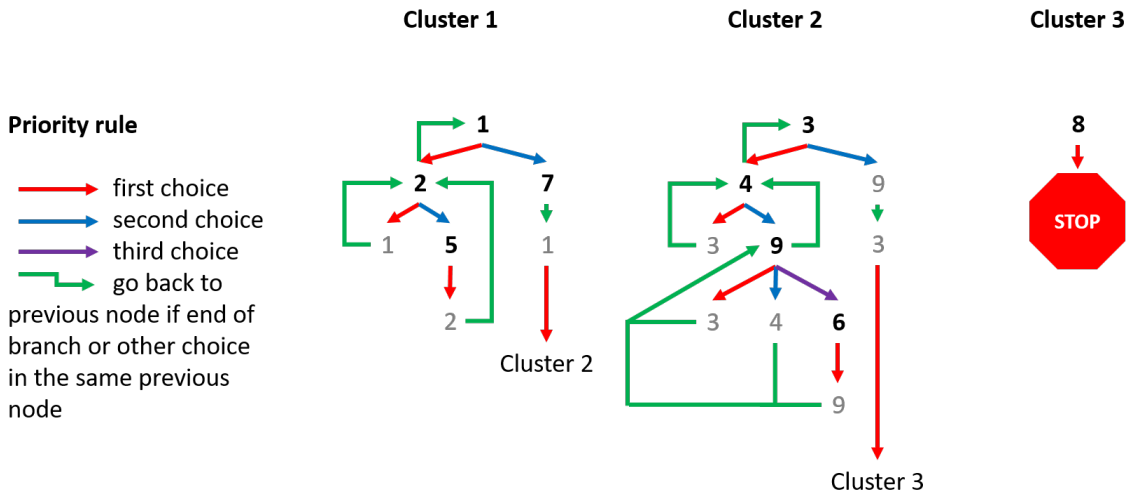

Figure 6.2: Tree graph of complete clustering algorithm

The algorithm shown below is compact, recursive and linear. Recursive because the depth-first logic always finds the first neighbour of a computed atom until the root, represented by the first computed object, is found again as a first neighbour. The logic can be interpreted by eq. (6.1) where the root r_1 is the first object and n_1 represented the first neighbour:

$$r_1 \xrightarrow{n_1} n_1(r_1) \xrightarrow{n_1} n_1[n_1(r_1)] \xrightarrow{n_1} \ldots \xrightarrow{n_1} n_1\{n_1[\ldots n_1(r_1)]\} = r_1 \tag{6.1}$$

The algorithm in Figure 6.3 is coded in Python with initialisation of the list of neighbours, the number of fragment (cluster) and the list of fragment number (in which cluster the atom is) for atoms which ensure the linearity by comparing the "cluster" location number (tree_id). This data is initialised to zero for all atoms. The main loop calls the CCA subroutine which attributes the same "cluster" location number to atom found according to the logic explained in eq. (6.1). The incrementation of fragment number (tree_number) occurs when the first "cluster" is completed through the CCA subroutine. The Fortran90 version is in Appendix E.3.

```
def append_to_list(object):
        global neighborhood, list, tree_number, tree_id  # global variables
        list.append(object)                              # add object to this tree
        tree_number[object-1] = tree_number              # object belongs to current tree
        for neighbor in neighborhood[object-1]:          # check the neighbors of object
                if tree_id[neighbor-1] == 0:             # is this neighbor in some tree?
                        append_to_list(neighbor)         # if not, add it to the current tree
************************************************
list = []
tree_id = [0]*atoms                                      # all objects are unassigned, tree_id=0
tree_number = 0                                          # no trees constructed yet
i = 1                                                    # object counter reset
while i <= atoms:                                        # there are unassigned objects
        if tree_id[i-1] == 0:                            # object is not yet part of a tree
                tree_number += 1                         # object starts a new tree
                append_to_list(i)                        # add object to this tree
        i += 1                                           # increase object counter
```

Figure 6.3: Python Complete Clustering Algorithm

The CCA which constructs the previous tree is linear, which means it depends only on the number of objects assign by comparing the "cluster" location number with zero meaning that the atom has not yet been computed through the CCA algorithm. To show the linearity of the CCA, a series of tests have been made by repeating 10,000,000 times the algorithm for three different sizes of HeND : 1500, 2500 and 9000 helium atoms. Figure 6.4 represents the obtained results for the execution time:

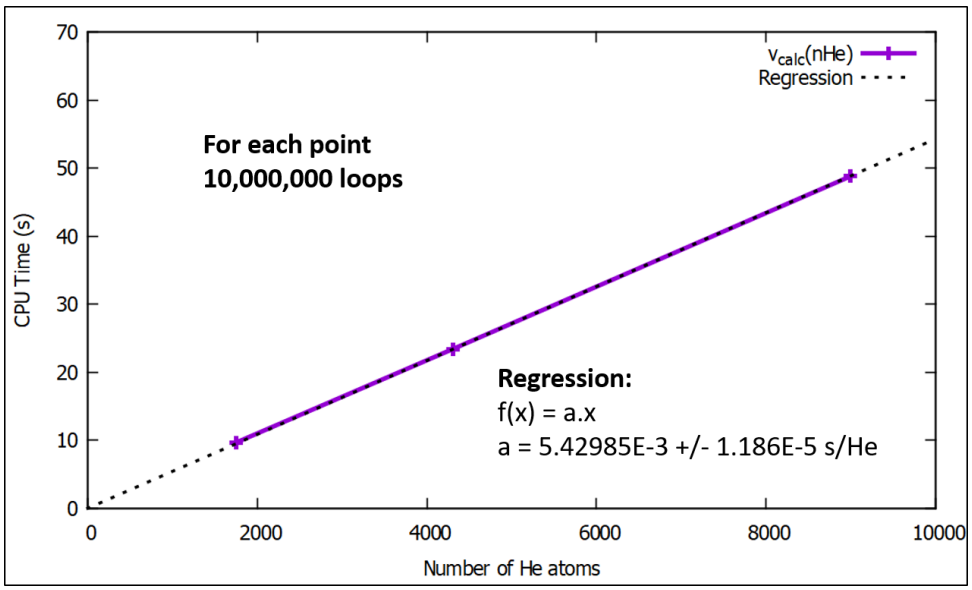

Figure 6.4: Linearity of the Complete Clustering Algorithm

A linear regression is calculated in Figure 6.4 to illustrate the fact that the execution time of the CCA depends linearly on the number of objects to analyse. The algorithm computes a

vector which is an ensemble of neighbours. These subclusters can be expressed as follow :

$$\{atom_i, ..., atom_n\} \subset Subset_i \tag{6.2}$$

This algorithm is useful to localise a dopants inHeND and to count the number of helium atoms surrounding. The application of this type of algorithm can be expanded to other field in data science by changing the criterion of neighbouring.

Chapter 7

Uniform and normal pseudo random numbers

In this thesis some phenomena need the use of random numbers to be modelled. Indeed, the initialisation of random collisions of HeND with dopant atoms and the determination of HeND chemical potentials by MC need respectively normal and uniform random numbers. This chapter describes some important techniques which were programmed in the present project. The development of these tools were inspired by Fortan90 subroutines [82].

7.1 Uniform deviates

To generate uniform random numbers ($0 \leq$ U $<$ 1 and probability P(U) = const), some generators are used which are called linear congruential generators (LCG). This kind of software creates a sequence of integers between 0 and $m-1$ by a recurrence relation based on a multiplier a, an integer b (here set to zero) and the modulus m, three positive integers:

$$x_{n+1} = (ax_n - b) \mod m \tag{7.1}$$

To start the algorithm an initial value named seed,x_0 has to be provided in the range between 0 and $m-1$. The uniform pseudo random numbers are computed from the real ratio U = x_{n+1}/m which gives a number U between 0 and 1. The major issue with this strategy of generating uniform deviates resides in the choice of a and m. To avoid the error of sequential correlation along the different calls of the subroutine, Lehmer [83] suggested to use a large prime number $m = 2^{31} - 1$, which is the largest number possible on 32-bit computer as modulus and a in the range $m-1$. This algorithm is known as prime modulus multiplicative linear congruential generator (PMMLCG) [84]. Another thing to consider is the multiplier a. In fact, a good choice of a gives a full period generator. In other words, the algorithm has to be periodic and cycles

when the initial value x_0 reappears after a period length of $m-1$ which is the full period. If a is not well chosen the generator behaves by generating a small period depending on the initial seed value which is a problem. Moreover, for a prime modulus there is a certain amount of multipliers a, which yields a full period. For $m = 2^{31} - 1$, one of the most privileged multipliers is $a = 16807$ according to the first suggestion of Lewis, Goodman and Miller in 1969 [85] and statistically studied by them. The generator passes through many numerical tests. Then Park and Miller proposed it as a "Minimal Standard" generator, which has a full period [86].

The latter generator has been programmed and used for different studies in this thesis. Knowing that it passed through many statistical tests, the 2D and 3D spectral test will be presented for the "Minimal Standard" and the RANDU generators. This kind of exercise was first discussed by Coveyou and Macpherson in 1967 [87]. They aimed to compare the distance between the parallel hyperplanes for different generators by using Fourier analysis. In 1968, Marsaglia proved that for some generators the numbers generated lie on hyperplanes in 3D whose number can be determined by the relation between the multiplier and the modulus: $(a!m)^{1/a}$. In the cube which takes into account the successive values x_n, x_{n+1} and x_{n+2} some parts of space are not covered by the generator between 0 and 1 and some are by the presence of hyperplanes. This shows that some uniform random value combinations will never appear in the sequence which is not a correct behaviour. This indicates a failure of a generator for this test.

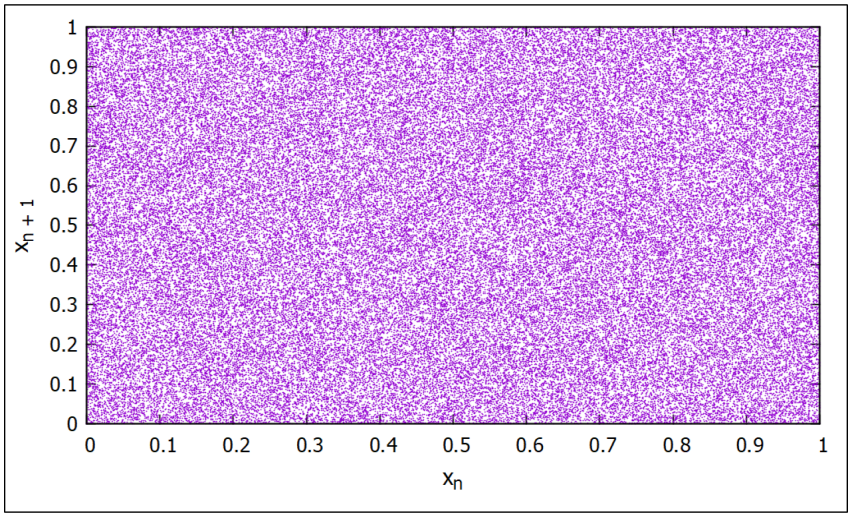

(a) 2D spectral test of RANDU LCG

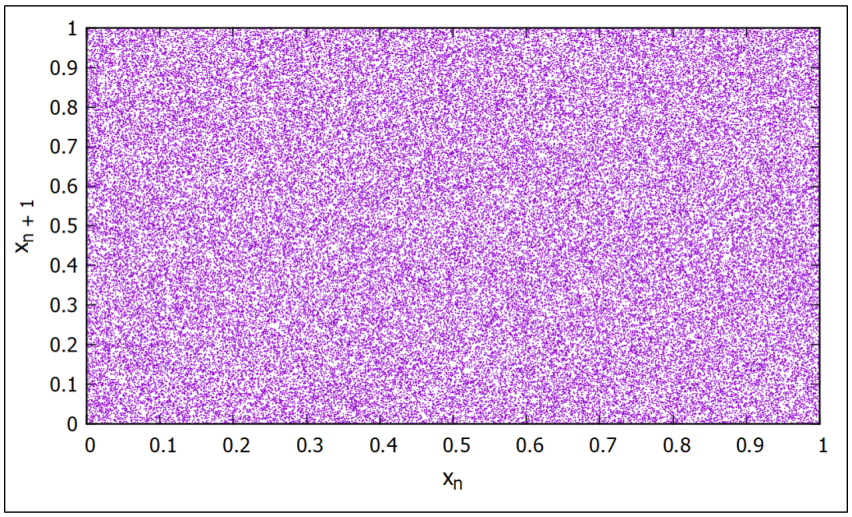

(b) 2D spectral test of Park-Miller LCG

Figure 7.1: 2D spectral for RANDU and Park-Miller LCG with x_0=1 and 100,000 values generated

Figure 7.1 shows the two 2D spectral tests for both kinds of generators where two successive numbers are plotted x_n against x_{n+1}. The observation is that there is no visible structure. The purple spots represent the numbers which have been generated and the blank ones those which have not been. With these graphs, the generators pass the 2D spectral test and the first impression is that they are equivalent despite the fact that the RANDU linear congruential generator (LCG) uses a=65539; m=$2^{31}-1$ and the Park-Miller LCG a=16807; m=$2^{31}-1$. The second test to do is the 3D spectral test where three values are taken into account x_n, x_{n+1} and x_{n+2}.

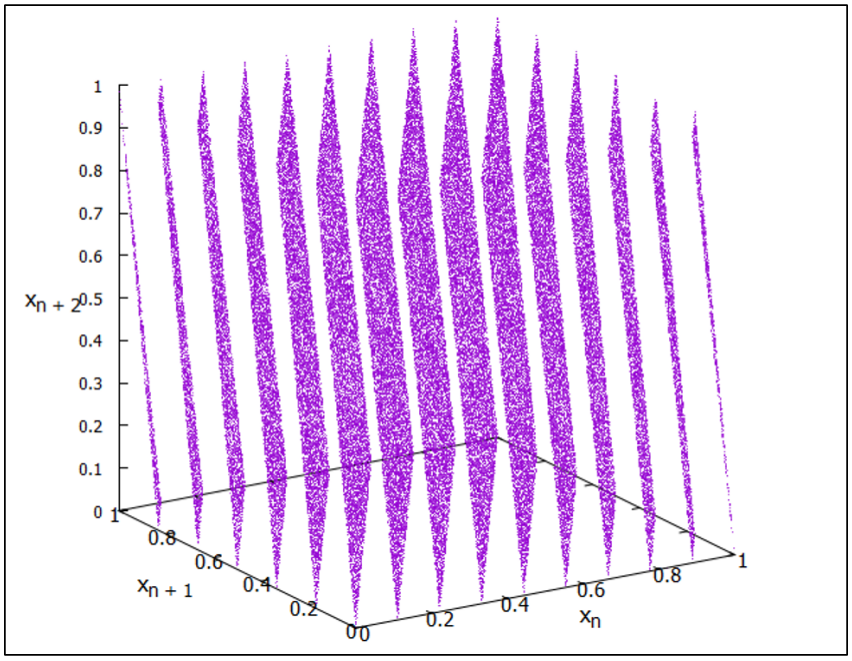

(a) 3D spectral test of RANDU LCG

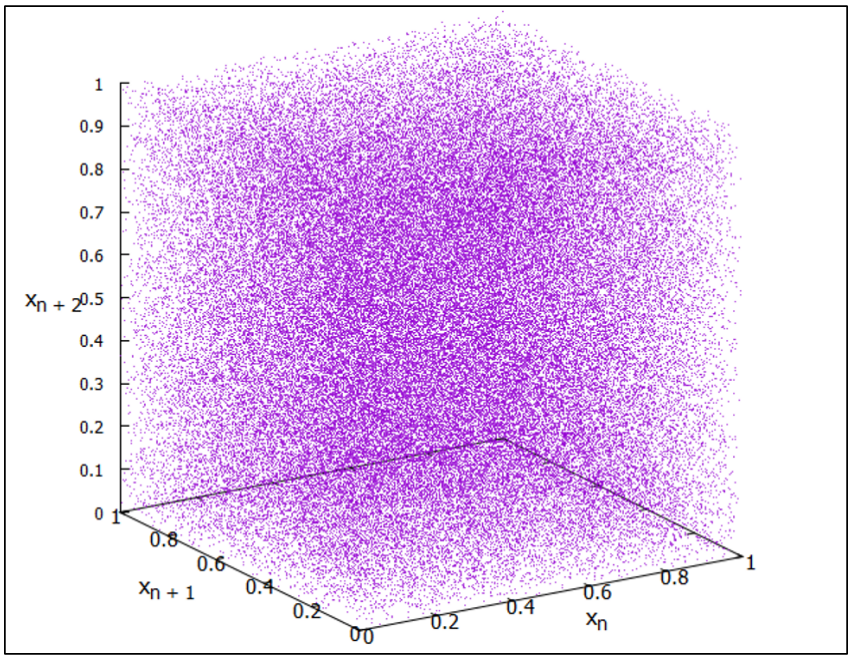

(b) 3D spectral test of Park-Miller LCG

Figure 7.2: 3D spectral for RANDU and Park-Miller LCG with x_0=1 and 100,000 values generated

With the 3D spectral test the difference between the two LCG is clearly visible. In fact as Marsaglia evoked in 1968, Figure 7.2 illustrates the hyperplanes and the areas not covered by the planes by the RANDU LCG. All the points of this generator fall in only 15 planes. It fails the criteria of randomness. The Park-Miller LCG passes the test which shows that it can be used

as a good uniform random number generator. No hyperplanes have been seen by exploration of the different angles of the cube. However, it is not perfect but by generating more values the uncovered area will become smaller until the limit which is $m-1$.

Another test is the calculation of the average and standard deviation of the Park-Miller LCG according to the number of call. Figure 7.3 represents the statistics for the uniform law, the two values of $\bar{x} = 0.5$ and $\sigma = \sqrt{1/12}$ respectively for the average and the standard deviation are not stable under 1,000 numbers generated. Between 1,000 and 100,000,000 pseudo random number generated, the Park-Miller LCG statistics exposes that they have not varied. So the method used is robust for our applications which demand a maximum of two or three pseudo random values. After 100,000,000 the weakness of this method displays its limit with a collapse.

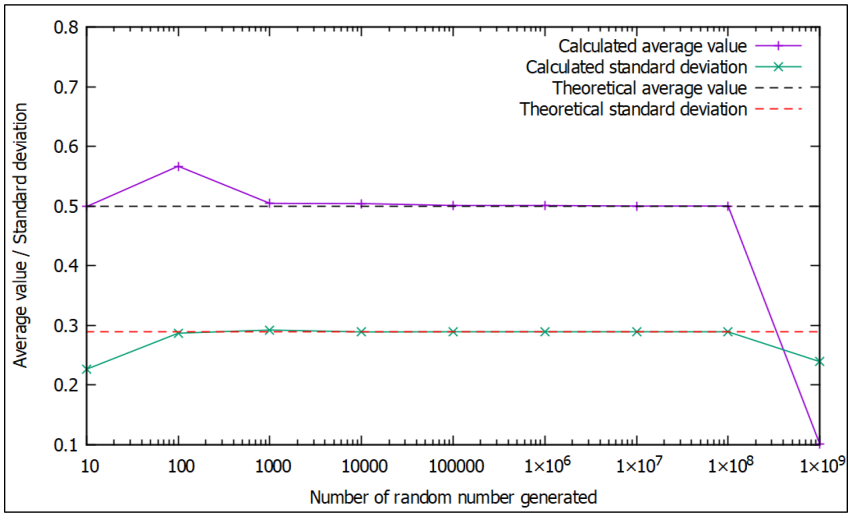

Figure 7.3: Average value and standard deviation for uniform law as a function of the number of pseudo random numbers generated

7.2 Normal deviates

A normal deviate is a random number generated according to a normal law $\mathcal{N}(\mu, \sigma^2)$ with the average value $\mu = 0$ and the standard deviation $\sigma = 1$. The method used for generating this type of pseudo random values is the Marsaglia polar method [88]. This one lands on the production of two random uniform numbers U_1 and U_2 to give two random normal numbers, $Z_{1,2}^{BM}$ for Box-Muller transform and $G_{1,2}$ for Marsaglia polar method at the end of the process. The latter application transforms uniform deviates U_1 and U_2 into V_1 and V_2 on [-1;1]. Then a calculation on a surface is done by $S = V_1^2 + V_2^2$ with $0 < S < 1$ which is a point on the unit circle. This strategy, known as Marsaglia polar method, avoids to compute the cosine and sine

compared to the Box-Muller transform [89] which is formalised as :

$$\begin{aligned} Z_1^{BM} &= \sqrt{-2\log(U_1)}\cos(2\pi U_2) \\ Z_2^{BM} &= \sqrt{-2\log(U_1)}\sin(2\pi U_2) \end{aligned} \tag{7.2}$$

The advantage of the Box-Muller method is that there is no condition to verify about the presence of the point in the unit circle. In Marsaglia polar method, the angular part, cosine and sine, is calculated by a trigonometric formula according to the axis of Cartesian space x and y represented by V_1 and V_2 and gives the following expression :

$$\begin{aligned} \cos(2\pi U_2) &= \frac{V_1}{\sqrt{S}} \\ \sin(2\pi U_2) &= \frac{V_2}{\sqrt{S}} \end{aligned} \tag{7.3}$$

The angular part obeys the uniform law which is multiplied by the radial part with a distribution as follow :

$$\int_0^R r\exp\left(-\frac{r^2}{2}\right)\mathrm{d}r \tag{7.4}$$

From the previous eq. (7.4) the radial part can be written by transformation as :

$$r = \sqrt{-2\log(S)} \tag{7.5}$$

Finally, the multiplication of the radial with the angular part gives a normal law pseudo random value computed as follows :

$$G_{1,2} = V_{1,2}\sqrt{\frac{-2\log(S)}{S}} \tag{7.6}$$

The average and standard deviation of a normal distribution is $\mu = 0$ and $\sigma = 1$. The first observation is the more there are numbers generated for the statistics the more the average and standard deviation converge towards $\mu = 0$ and $\sigma = 1$ as seen in Figure 7.4.

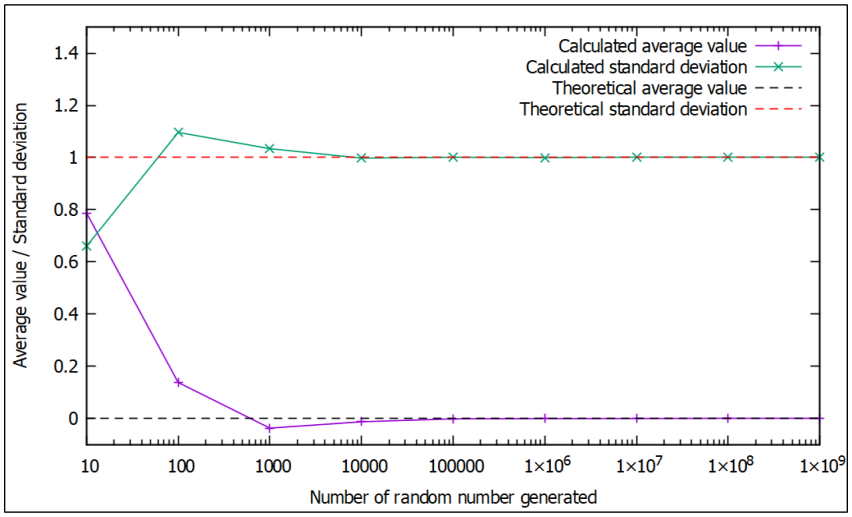

Figure 7.4: Average value and standard deviation for normal law as a function of to the number of pseudo random number generated

The Ziggourat algorithm is another technique to compute a lot of normal deviates. It is based on tabulated data and was developped by Marsaglia and Tang [90]. Considering the small amount of normal random number needed in our study, the method has not been pursued.

Part III

Numerical results

Chapter 8

Photodissociation of molecular iodine in HeND

8.1 Introduction

HeND are a subject of interest since three decades in different fields of physics and chemistry in order to characterise, to study the dynamics of aggregation and dissociation in a nanometric, finite, cold and liquid environment of molecules of interest [11, 20, 91–95]. Moreover the rapid and efficient energy transfer in the droplets lead to the formation of unusual molecular structures which have experimentally been studied like HF $\cdots$ HCN [96], X $\cdots$ HF [97], CH_3 $\cdots$ HF [98] and CH_3 $\cdots$ H_2O [99]. The reaction of photodissociation in bulk liquids has been studied and shown the cage effect phenomenon and recombination [41] of the fragments in few picoseconds and particularly for molecular iodine [100].

Modelisation of molecular iodine photodissociation follows the idea of Murrell, Stace and Dammel [101]. This theoretical work studied the photodissociation of this system in a dense inert gas. One phenomenon involved in this type of experimentation is the cage effect which was first described by Franck and Rabinowitch in 1934 [41]. The cage effect of a given solvent impacts the production rate of free radicals by photolysis. In a gas, excitation of a diatomic molecule above its fragmentation limit releases two photofragments in absence of collisions or photon emission. In a liquid system the photodissociation allows two scenarios. The first one is fast recombination due to collisions with solvent atoms which absorb and release the excess of kinetic energy by evaporation of the solvent. The second one is the long time survival of separated fragments. Indeed the photofragments follow a random path depending also on collisions with the host solvent atoms. But in a cluster environment a third scenario becomes possible, namely fragments leaving the cluster with or without attached cluster particles. All scenarios are illustrated in Figure 8.1. The study of Murrell *et al.* was done for molecular iodine embedded in CCl_4 at different pressures and temperatures.

In the works of Braun and Drabbels [42–44], photodissociation outcomes has been reported for the analogous systems CH_3I and CF_3I. Statistics on the velocity and fragment size distribution have been given. Those experimental data will be compared to the results of the simulation with the CLUSTER code. In this work, the mechanism of fragmentation and recombination of the molecular iodine is the subject of interest. Indeed, the molecular iodine has been studied by several experimentalists for photodissociation in rare gases and liquids [102–105]. The experimental results showed that the cage effect only depends on the density of the rare gas and it appears when the density is close to the liquid state. The modelling of the physics of the phenomenon occurring experimentally has motivated atomistic description of fragmentation in CCl_4 [101, 106] and a Langevin description for recombination [107]. Moreover, the quenching of the photolysis of halogen rare gas van der Waals complexes has been observed for rare gas atoms where atom cage effect occurs [108–110].

The present work which has been published in 2021 [56] reports the result of a model calculation based on a quantum effective potential He-He for helium clusters with 2500 to 9000 atoms. The I-I and I-He interactions are treated respectively as a Morse oscillator and as a Lennard–Jones potential adjusted to *ab initio* calculations [111]. Considering the quantum nature of helium at temperature below the λ-point (2.17 K), the simulation of HeND ideally requires a fully quantum time-dependent description. Some approximations on the delocalisation of helium atoms has been done by using the method of quantum effective potentials which has been originally developed for simulations of atom pickup by large helium clusters [112]. This method has been described in the previous subsection 5.2.2 and used for previous work on photodissociation in neon and argon clusters [54, 113] and for the fragmentation dynamics of neutral dopants within helium clusters following electron impact ionisation [55, 114, 115].

The HeNDs are treated with angular momentum L = 0 which might not reflect the true situation. According to the work of Gomez using ultra-fast X-ray imaging [45], the droplets present distortions bound to the condensation and smooth collisions during the helium atom selection through the nozzle in the apparatus in Figure 1.1 and 1.2.

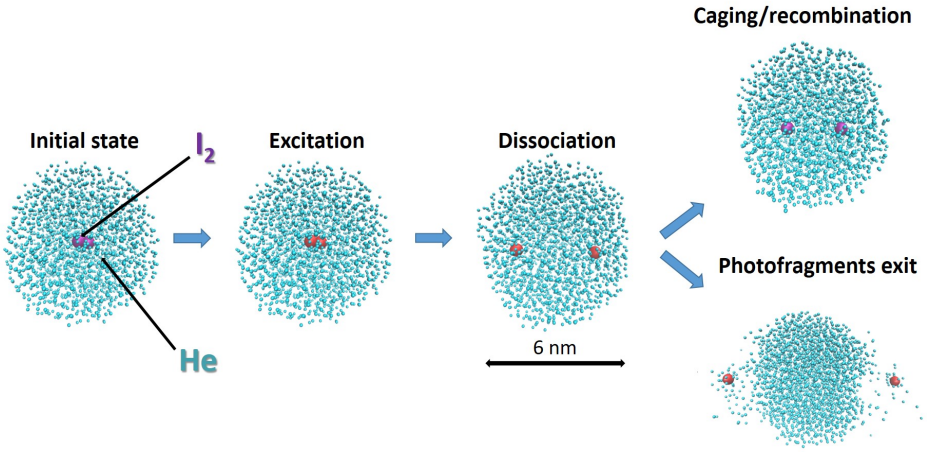

Figure 8.1: Possible outcomes of molecular iodine photodissociation in helium nanodroplet

8.2 Method and protocol

8.2.1 Modelling of molecular iodine photodissociation

Photodissociation is a chemical reaction involving a molecule and a photon with a certain amount of energy to break the molecular bond. Molecular iodine dissociation can be summarized as :

$$I_2 + h\nu \rightarrow 2I \tag{8.1}$$

Energy of dissociation of the molecular iodine in this model is about 1.55 eV. Excitation starts from the X state to the continuum of the A states [100]. Then, a deexcitation/relaxation to X state takes place which is assumed to be faster than the photodissociation [101]. The simulations start on the X state as seen in Figure 8.2. The repartition of the energy excess is isotropic considering the symmetry of the molecular iodine. Below the molecular iodine fragmentation all excitations represent a vibration mode of the molecule. Excitations just above the fragmentation limit place the molecular iodine into a rovibrational state in the continuum of the X ground state. In the simulations, the excitation is about 2.33 eV and the energy is applied by adding corresponding velocities to the initial iodine velocities to ensure the dissociation and the appearance of photofragments. However, the dissociation process is not exactly along the molecular bond because each iodine atom has initial velocity components proportional to the temperature of equilibration.

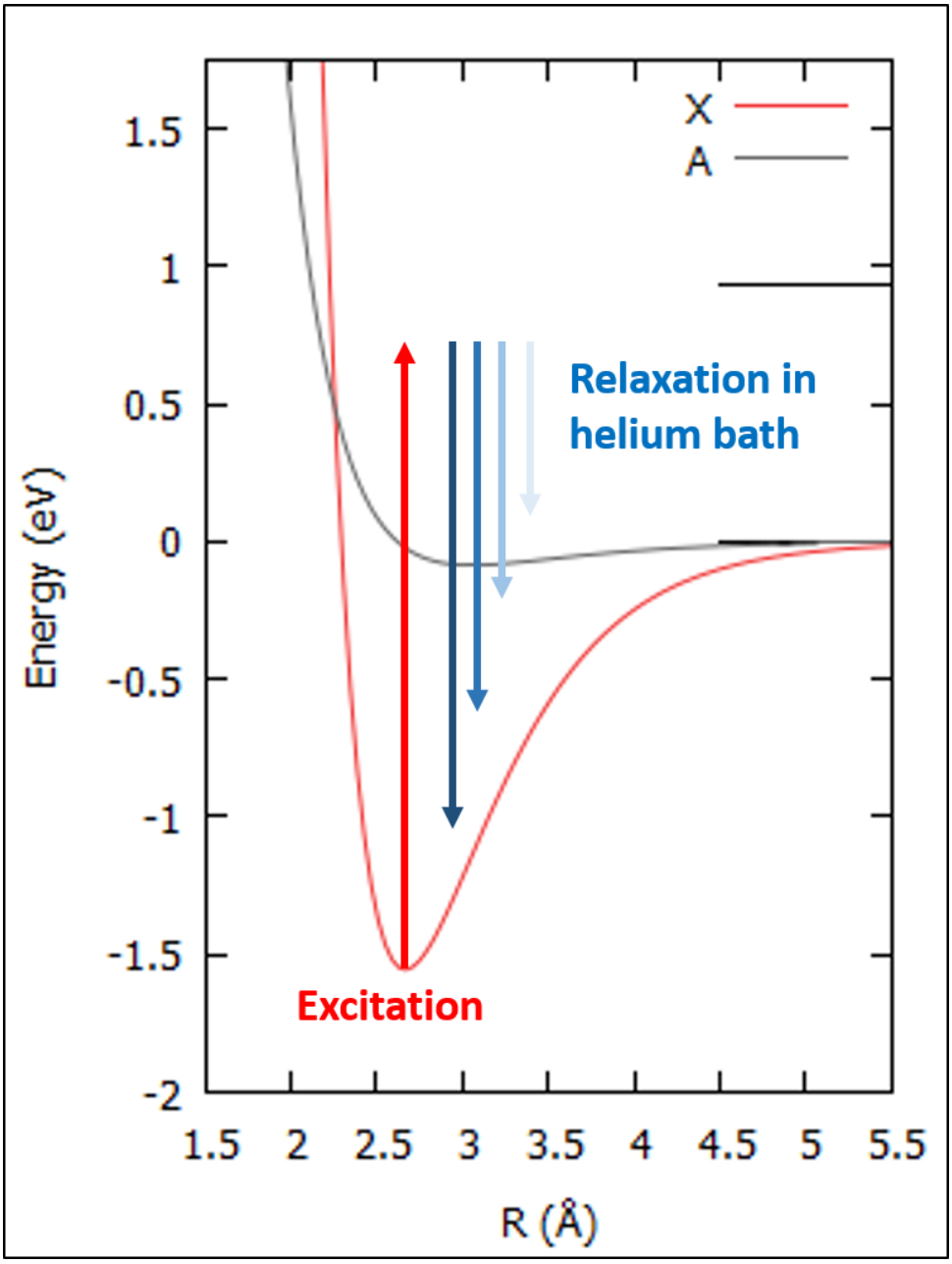

Figure 8.2: Potential energy diagram of the photodissociation of the molecular iodine from X ground state to A continuum excited state

8.2.2 Computational protocol

First thing computed in the protocol is the reduced mass of the molecular iodine. The latter is expressed:

$$\mu_{I_2} = \frac{m_I^2}{2m_I} = \frac{m_I}{2} \tag{8.2}$$

Photodissociation occurs on the molecular iodine bond so we use the collinearity between the vector of the relative velocity and the position of the I-I bond expressed as follow :

$$\vec{v}_{rel} = k.\vec{r} \tag{8.3}$$

By using eqs. 8.3 and 8.2 the relative kinetic energy can be given by :

$$E_{rel} = \frac{1}{2}\mu_{I_2} v_{rel}^2 = \frac{1}{4} m_{I_2} \left[k^2 \left(r_x^2 + r_y^2 + r_z^2\right)\right] \tag{8.4}$$

The expression of the collinearity parameter k can be deduced from eq. (8.4) :

$$k = \frac{2}{r}\sqrt{\frac{E_{rel}}{m_{I_2}}} \tag{8.5}$$

With eqs. 8.3 and 8.5 half of the relative velocity, named v_{Ex}, is added to the iodine atom thermal velocities v_{therm} giving a resultant velocity v_{T}, non-collinear to the molecular iodine bond.

$$v_{\mathrm{T}} = v_{\mathrm{therm}} + \frac{v_{rel}}{2} = v_{\mathrm{therm}} + v_{\mathrm{Ex}} \tag{8.6}$$

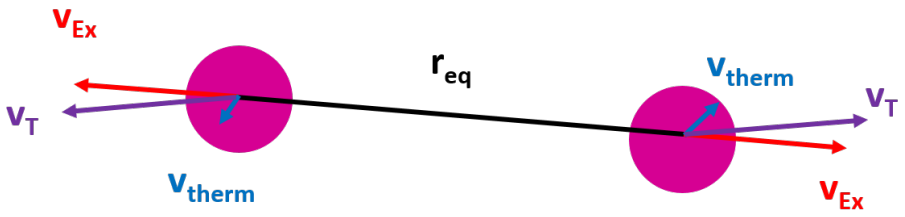

Figure 8.3: Model of the molecular iodine photo dissociation

The protocol of simulation of the system $I_2@He_n$ is done by an automation script of the different simulations named for equilibration EQUI, for the phase of photodissociation ZAPING and for the phase of relaxation EQZAP for nanodroplets containing 2500 to 9000 atoms for a predefined number of cycles. Before starting the automatic protocol, the HeND has been equilibrated at constant temperature at 0.5 K with a Berendsen thermostat [57, 64] for the effective He-He Morse potential V(D_e = 0.8 cm^{-1}; r_e = 4.1 Å; a = 1 $Å^{-1}$). Identical calculations have been done for V(D_e = 0.65 cm^{-1}; r_e = 4.1 Å; a = 1 $Å^{-1}$) at 0.37 K. During all the phases, the trajectories are integrated by using the velocity Verlet method [57, 61]. Moreover, the HeND are simulated without angular and linear momenta (L = 0; P = 0) and with a constraint of constant energy. So $E_{kin,int} = E_{kin}$ and the kinetic energy can be expressed with degree of freedom

[67–69] as:

$$E_{\text{kin}} = \frac{N_{df}}{2} k_b T = \frac{3n_{atom} - 7}{2} k_b T \tag{8.7}$$

Then, the HeND is ready to enter in the automation phases. To compute 1,000 trajectories the strategy was to divide the simulations in 20 parts of 50 chained simulations where the initial configuration files of the HeND are different from each other. This difference is notably observed on the velocity of atoms with different NVE states at 0.37 and 0.5 K. This guarantees the exploration of the phase space and an ergodic characterisation of the global study.

The phase of equilibration EQUI prepares an HeND at constant energy. The number of time steps is 10,000 and the time step is 10 fs simulating a physical time of 100 ps. Figure 8.4 below represents the pair correlation function of I-He for a droplet with 2500 helium atoms after the equilibration phase. The first observation is that the density peaks for the first and second helium neighbour of the iodine are at about 3 and 7 Å respectively which motivates the choice of considering helium atoms as neighbours in a sphere of 6 Å of radius for the different study in this document. The second observation is the density plateau around 0.023 He/Å^3 which represents the density of the droplets close to the bulk one [116, 117].

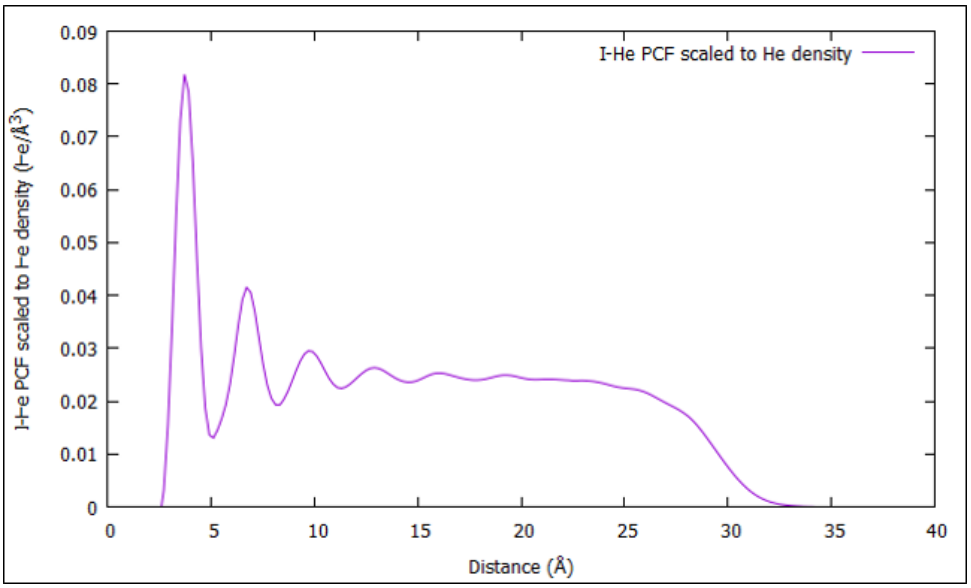

Figure 8.4: Iodine–helium pair correlation function scaled to helium density at equilibrium for a 2500 atom droplet

The second phase ZAPING is MD where photodissociation of the molecular iodine occurs. The number of time steps and the value of the time step have been changed respectively to 8,000 and 0.25 fs. This is motivated by the fact that photodissociation is a very fast phenomenon and needs a finer integration time step to capture all the violent energy transfers. In fact, the recombination occurs on a time scale of picoseconds which motivates our choice of time step and number of steps to simulate a physical time of 2 ps. The last EQZAP phase is the

monitoring of all the statistics and data on the photofragments with a time step of 3 fs over 10,000 steps which represents a physical time simulated of 30 ps. The different time steps have been chosen to maintain the relative energy fluctuation below 10^{-6}. The strategy of computing can be illustrated in Figure 8.5.

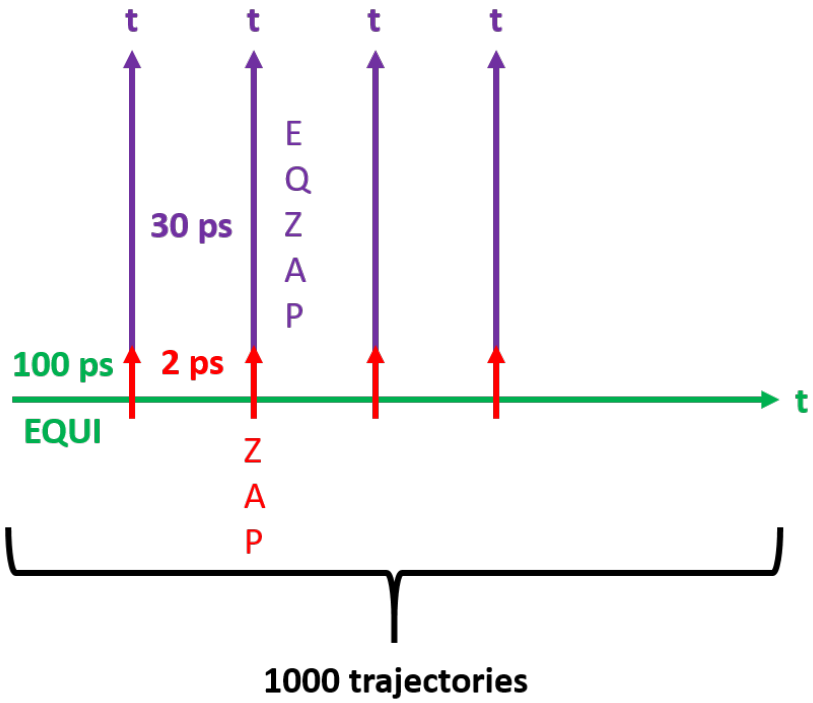

Figure 8.5: Computational protocol for molecular iodine photodissociation. Photodissociation trajectories are spawned from a long equilibrium trajectory

After the EQZAP, the HeND previously equilibrated at constant energy starts another EQUI phase giving another spatial arrangement of atoms which undergoes the process of ZAPING and EQZAP. The data stored come from an HeND better equilibrated than the previous one every 100 ps. Phases of the study are shown in Figure 8.6 where the energy of the iodine photofragment is plotted as a function of the time for one selected trajectory.

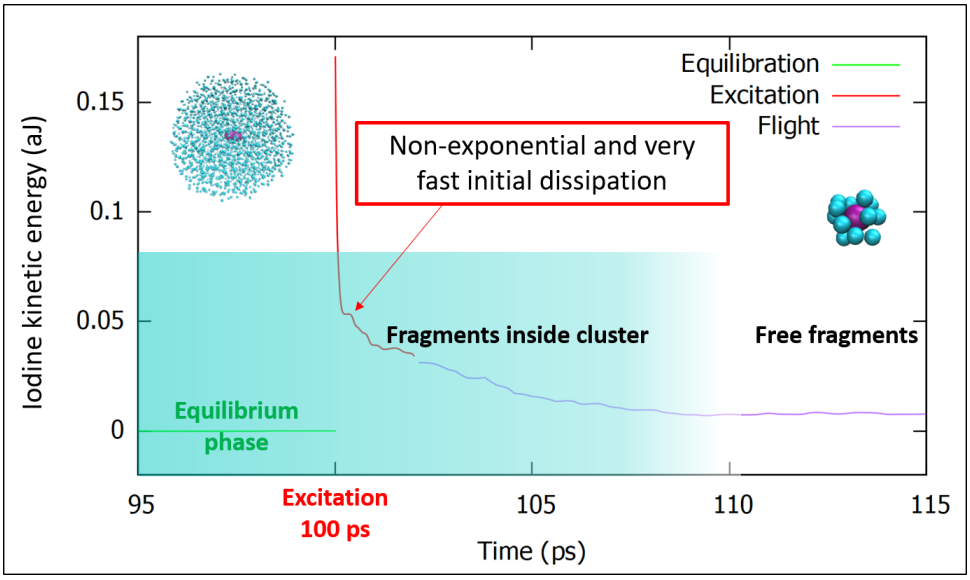

Figure 8.6: Photofragment energy dissipation for a HeND containing 2499 atoms and for an excitation of 2.33 eV

The shaded area symbolises the density of helium trough which the iodine atom travels in the nanodroplet. One observation is the decrease of this density until the exit of the photofragment composed by the iodine atom surrounded by several helium solvent atoms about 10 ps after the excitation. The second one is the very fast and non-exponential dissipation of energy in the HeND during the ZAPING phase simulating the application of a 532 nm Nd:YAG laser beam which is equivalent to 2.33 eV. The dissipation of most of the energy occurs in less than 2 ps which does not correspond to a classical fluid. The last part is the flight of the photofragment with an exponential profile and a remaining kinetic energy.

8.2.3 Dopant location in HeND

The dopant is generally in the center of the nanodroplet which corresponds to the minimum of its radial potential [118]. If the dopant goes away from the center the radial potential increases. In a simulation with a kinetic energy contribution the dopant can explore a volume around the center of mass of the nanodroplet. This is due to the Brownian motion. Figure 8.7 shows the diffusion of molecular iodine in a HeND 2500 projected onto the XY-plan observed in one of our trajectories. The dopant does not remain in the center of the droplet [119] and explores a certain volume during the time scale of 10 ns. The dopants move on a distance equivalent to 8 Å over a HeND radius of 30 Å which represents a significant degree of delocalisation. The study has been done for nanodroplets without constraint on the rotation. But according to recent experimental works, the droplets present a shape distortion which is the result of an inherent angular momentum. The prolongation of the present work would be to study the location of dopant in a rotating cluster which will probably show even stronger off center positions.

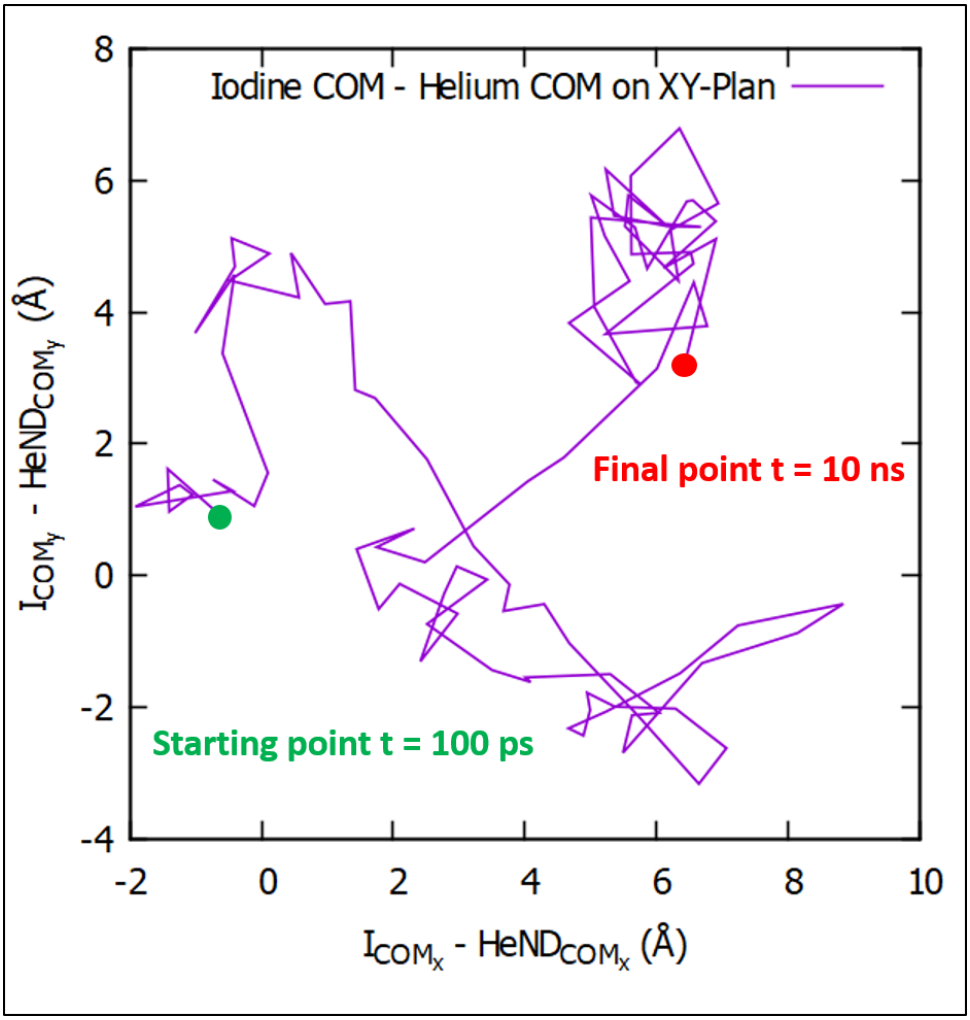

Figure 8.7: Diffusion of the molecular iodine in the HeND on the XY-plan

8.3 Results and discussion

8.3.1 Caging effect

The dissociation of molecular iodine becomes possible if the energy of excitation exceeds the threshold of 1.55 eV. However, in the HeND, which is a confined nano environment, the diverse processes involved in cage effect are shown. Indeed, the molecular bond breaking can occur followed by a phase of recombination which presents two parts [120, 121]. The primary recombination where the atomic fragments remain close to each other and they get back into molecular form within a few picoseconds. The secondary cage effect where radicals undergo diffusion and make some collisions with the solvent atoms before reforming the molecular structure within a few nanoseconds. These phenomena are possible because of the efficient energy dissipation in this medium.

Figure 8.8 shows the number of helium atoms in the vicinity of atomic iodine within a range of 6 Å (see Figure 8.4 as motivation). According to the criterion of neighbouring, the iodine atoms at rest are surrounded by about 25 helium atoms. By increasing the energy of excitation the solvent shell of helium tends to become smaller. The iodine atoms remain in the nanodroplet for excitation energies below 2 eV. In this regime of trapped photofragments, the molecular iodine explores vibrational mode. Between the fragmentation limit of 1.55 eV and about the 2 eV of excitation, molecular bound breaking occurs without release of photofragments. The iodine atoms experience the different types of recombinations which depend on the amount of energy deposited in the system. The threshold observed for photofragments leaving the cluster is about 2 eV which is the start of the free fragments regime.

The photodissociation works of Braun and Drabbels [42–44] shed light on the fact that the exit of heavy atoms is a direct non-thermal process where the dopants are expelled from the HeND because of their high initial velocities and masses which push away the helium atoms. An ejection process occurs during our simulations with an excitation twice lower than in Braun and Drabbels protocol.

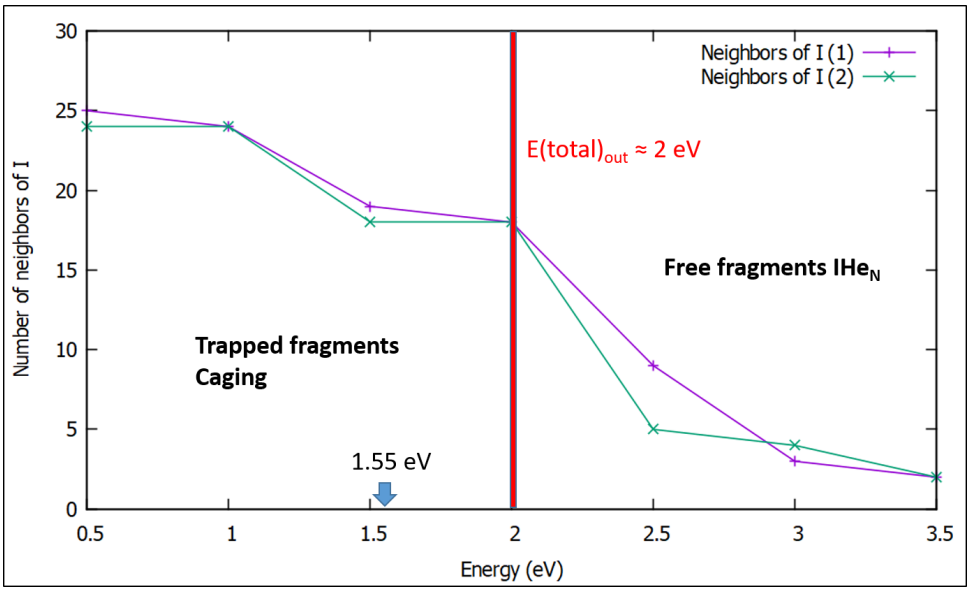

Figure 8.8: Number of helium atoms within a radius of 6 Å of iodine in the two photofragments I@He$_n$ for HeND 5000

8.3.2 Velocity distributions

The experimentalists use the Velocity Map Imaging (VMI) technique to analyse the behaviour of dopants in the HeND [42–44]. In this numerical work, 1,000 independent simulations have been computed following the procedure explained in subsection 8.2.2 with an energy of excitation of 2.33 eV which corresponds to a 532 nm Nd:YAG laser. This is half the energy used in

the experiment of Braun and Drabbels. At the end of each trajectory, data on the two generated photofragments are collected. The products of photolysis are iodine atoms surrounded by a certain amount of helium atoms.

From 1,000 trajectories the data on the velocities of these fragments are binned into histograms for different size of nanodroplets: 2500, 5000 and 9000. The data are compared to a Gaussian distribution where a χ^2 test has been performed. It results that the velocity distributions do not correspond to a Gaussian model. Expected amplitudes and corresponding error bars are shown as black lines along with the solid bars representing the computed fragment velocity distributions. For each histogram, the error bars correspond to the Poisson statistics standard deviation for the expected count rates. The average values of the velocity distributions for HeND containing 2500, 5000 and 9000 atoms are respectively $336 \pm 1.21\,\mathrm{m/s}$, $246 \pm 1.00\,\mathrm{m/s}$ and $192 \pm 1.32\,\mathrm{m/s}$ for Morse potential V($D_e = 0.8\,\mathrm{cm}^{-1}$; $r_e = 4.1$ Å; a = $1\,\mathrm{Å}^{-1}$) at 0.5 K presented in Figure 8.9 on page 88. The standard deviations of the velocity distributions for HeND containing 2500, 5000 and 9000 atoms are respectively $54\,\mathrm{m/s}$, $45\,\mathrm{m/s}$ and $59\,\mathrm{m/s}$. The same calculations have been done for Morse potential V($D_e = 0.65\,\mathrm{cm}^{-1}$; $r_e = 4.1\,\mathrm{Å}$; a = $1\,\mathrm{Å}^{-1}$) at 0.37 K and the results are $322 \pm 0.78\,\mathrm{m/s}$, $256 \pm 1.51\,\mathrm{m/s}$ and $187 \pm 1.91\,\mathrm{m/s}$ presented in Figure 8.10 on page 89. The standard deviation of the velocity distributions for HeND containing 2500, 5000 and 9000 atoms are respectively $35\,\mathrm{m/s}$, $67\,\mathrm{m/s}$ and $85\,\mathrm{m/s}$. The bigger the droplets are, the lower are the computed averages. This can be explained by the fact that during the travel to reach the droplet surface, the photofragments undergo dissipation of energy. More there are atom collisions more there is dissipation of energy.

Experimentally, the obtained distributions for analogous system (CH_3I and CF_3I) also do not correspond to a Gaussian model with a 266 nm Nd:YAG laser [42]. The average value of their velocity distribution is in the same range but higher than our numerical observations. Moreover, they observe a dependence of the kinetic energy of the photofragment with the size of the HeND. For now there are no experimental results for the system numerically studied.

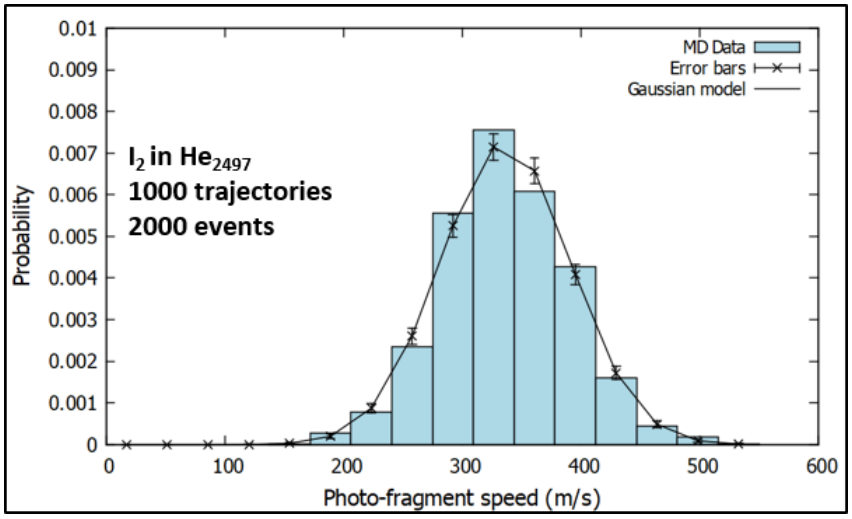

(a) Velocity distribution of HeND 2497

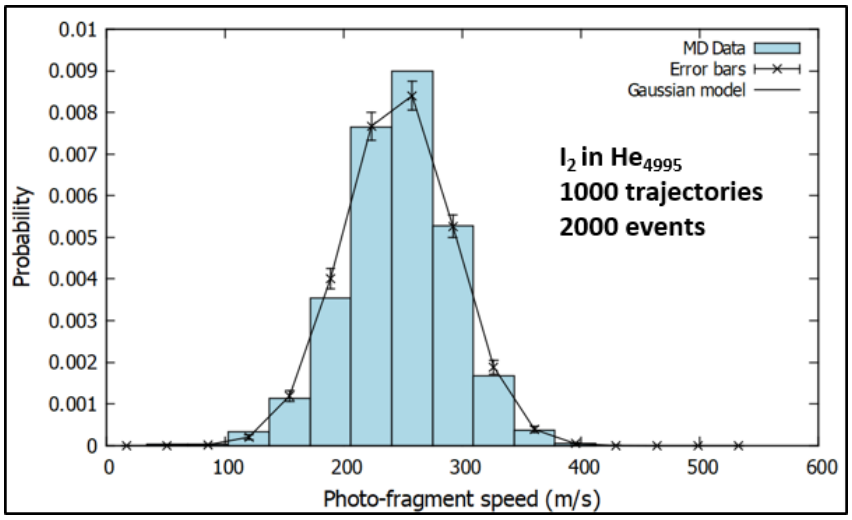

(b) Velocity distribution of HeND 4995

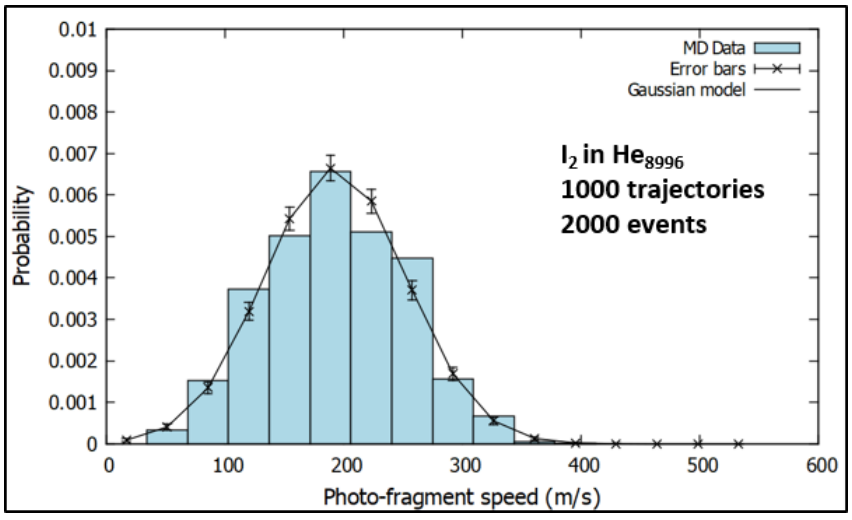

(c) Velocity distribution of HeND 8996

Figure 8.9: Photofragment velocity distributions computed for HeND 2500, 5000 and 9000 with V(D_e = 0.8 cm^{-1}; r_e = 4.1 Å; a = 1 $Å^{-1}$) at 0.5 K

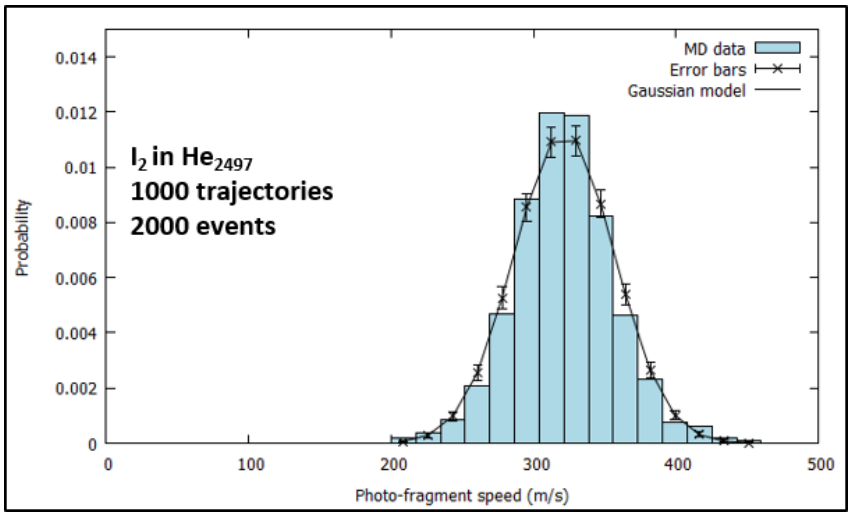

(a) Velocity distribution of HeND 2497

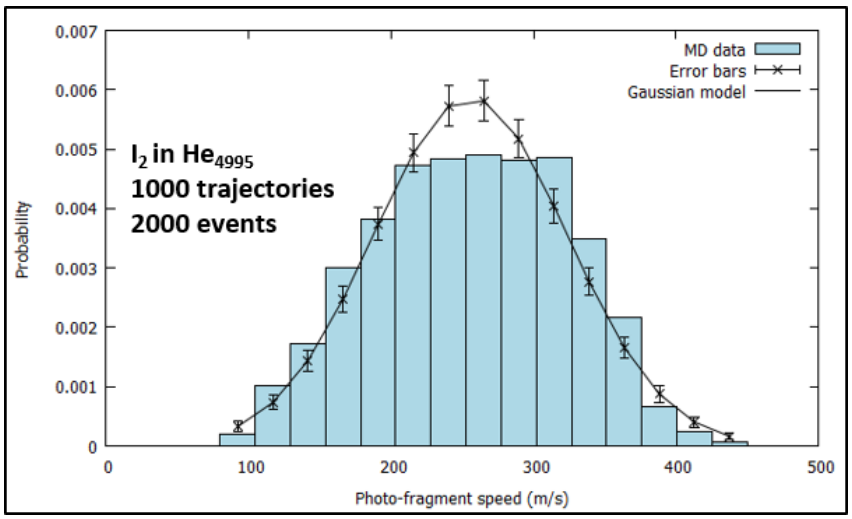

(b) Velocity distribution of HeND 4995

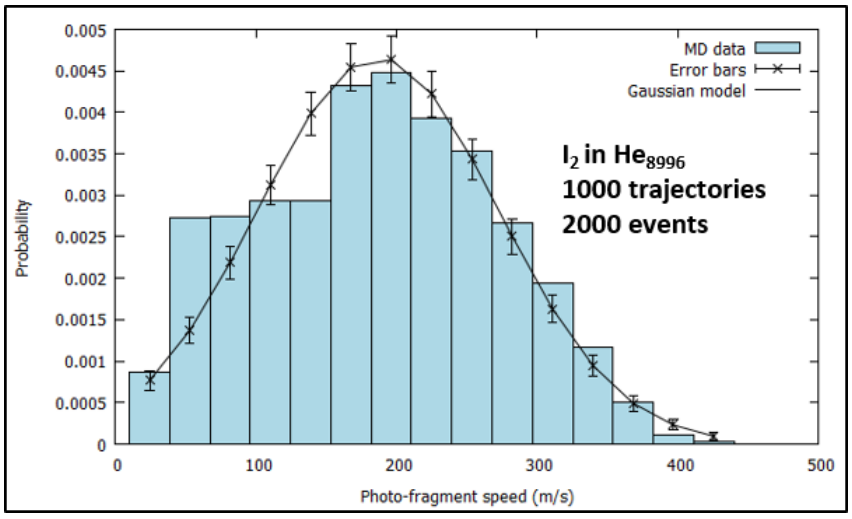

(c) Velocity distribution of HeND 8996

Figure 8.10: Photofragment velocity distributions computed for HeND 2500, 5000 and 9000 with V(D_e = 0.65 cm^{-1}; r_e = 4.1 Å; a = 1 $Å^{-1}$) at 0.37 K

8.3.3 Fragment size distributions

During the phase of photofragment analysis, another observable is the size of the photofragments which are composed of an iodine atom surrounded by helium atoms IHe_n. Photofragment size distributions were constructed by binning computed fragment sizes from 1,000 trajectories into histograms. According to the model of excitation presented earlier the products of photolysis are neutral. The distributions are not consistent with a Gaussian model. In this case, the slower the photofragment is, the more there are helium atoms as satellites of iodine atom. For the three size of HeND 2500, 5000 and 9000 and the Morse potential V(D_e = 0.8 cm^{-1}; r_e = 4.1 Å; a = 1 $Å^{-1}$) at 0.5 K the average values are respectively 6.4 ± 0.05 He, 9.3 ± 0.05 He and 13.2 ± 0.07 He presented in Figure 8.11 on page 91. The standard deviation of the fragment size distributions for HeND containing 2500, 5000 and 9000 atoms are respectively 2.4 He, 2.4 He and 2.9 He. Likewise, the study has been realised for the potential V(D_e = 0.65 cm^{-1}; r_e = 4.1 Å; a = 1 $Å^{-1}$) at 0.37 K which is the experimental temperature and gives as results 7.2 ± 0.04 He, 10.3 ± 0.08 He and 13.7 ± 0.09 He presented in Figure 8.12 on page 92. The standard deviation of the fragment size distributions for HeND containing 2500, 5000 and 9000 atoms are respectively 1.9 He, 3.7 He and 4.3 He. The obtained results are in accordance with the experimental ones over the dependence toward the size of the nanodroplet [43]. To continue, the average kinetic energies of the photofragments for the three sizes have been computed for both potentials. The following results are given by increasing size 2500 to 9000 helium atoms. For the potential where the calculations have been done at 0.5 K the results give 740 cm^{-1}, 424 cm^{-1} and 290 cm^{-1} and for the one at 0.37 K, 675 cm^{-1}, 468 cm^{-1} and 270 cm^{-1}. These kinetic energies are comparable for analogous systems like CF_3I and CH_3I for IHe_n fragments in Braun and Drabbels results [42]. The kinetic energy ranges from about 800 cm^{-1} to 1200 cm^{-1} for CF_3I and from 320 cm^{-1} to 360 cm^{-1} for CH_3I. Our outcomes are somewhat lower than the experimental ones because of the intensity of excitation.

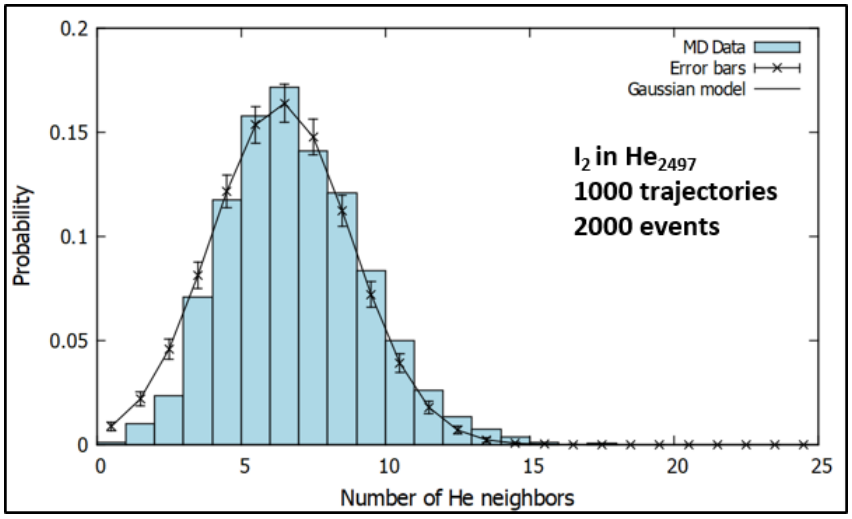

(a) Fragment size distribution of HeND 2500

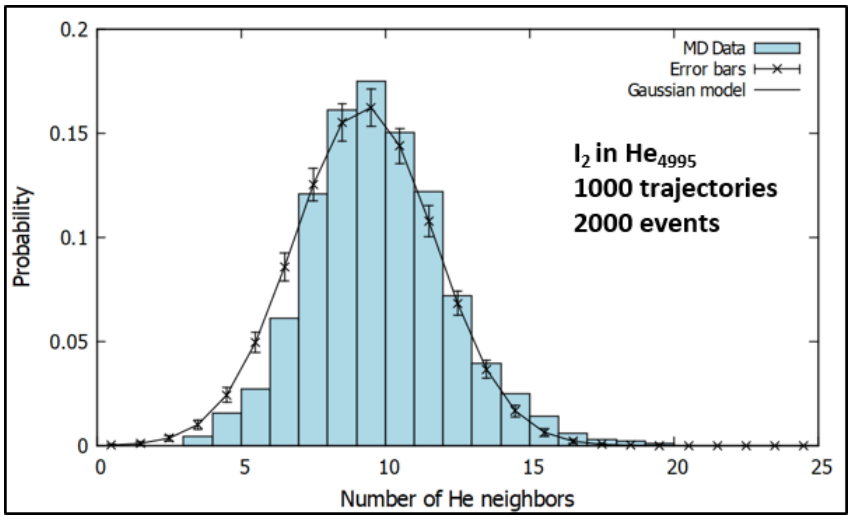

(b) Fragment size distribution of HeND 5000

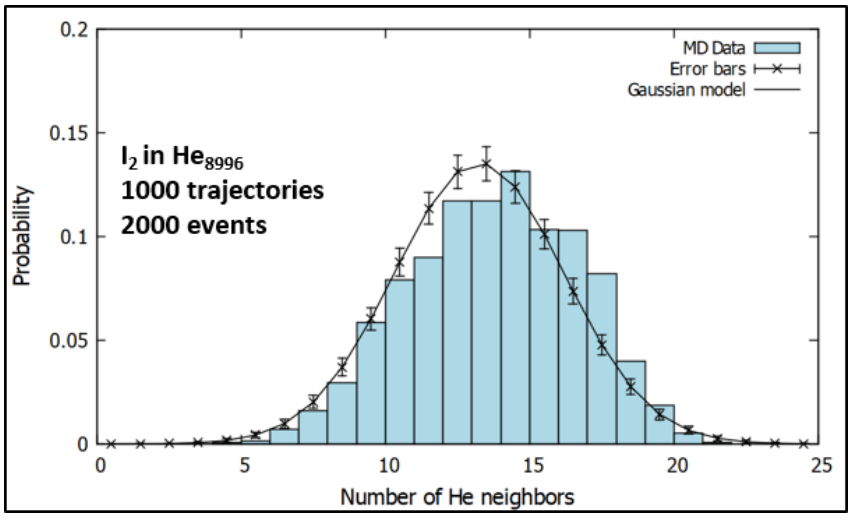

(c) Fragment size distribution of HeND 9000

Figure 8.11: Photofragment size distributions computed for HeND 2500, 5000 and 9000 with V(D_e = 0.8 cm^{-1}; r_e = 4.1 Å; a = 1 $Å^{-1}$) at 0.5 K

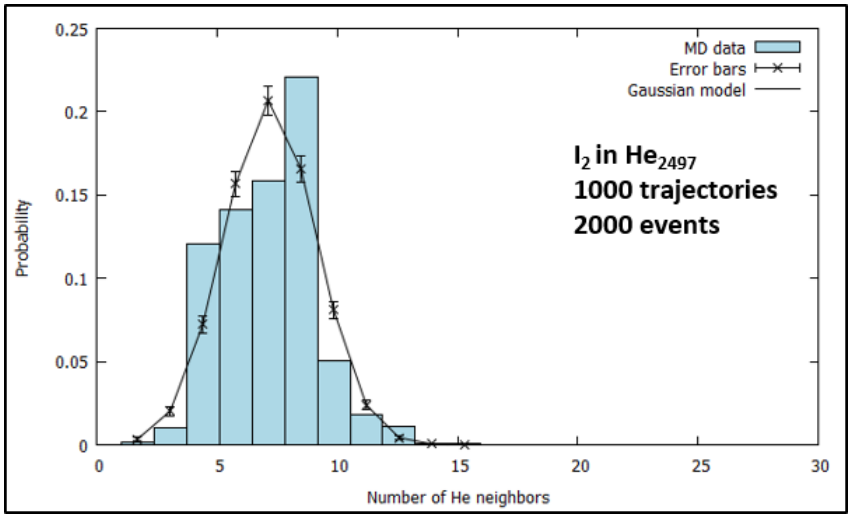

(a) Fragment size distribution of HeND 2500

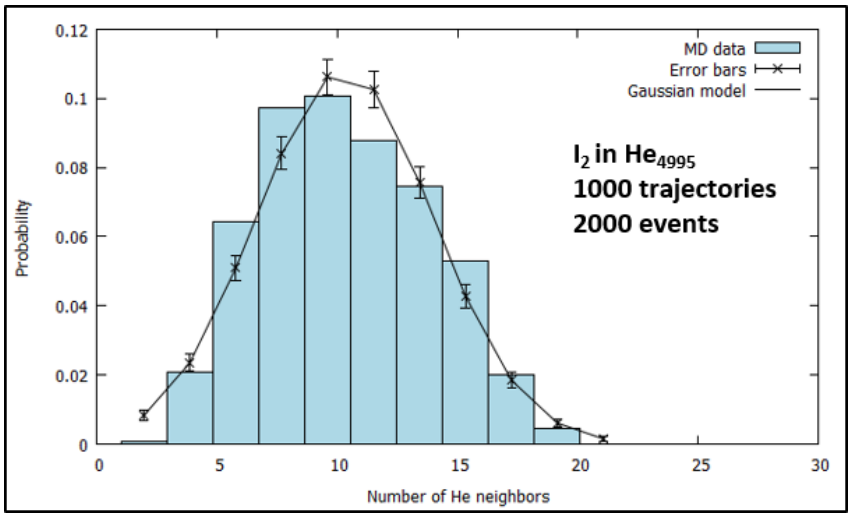

(b) Fragment size distribution of HeND 5000

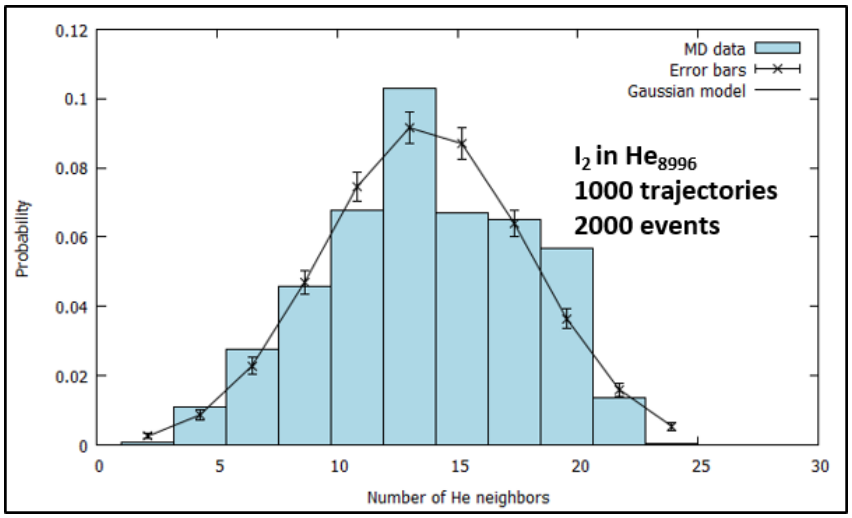

(c) Fragment size distribution of HeND 9000

Figure 8.12: Photofragment size distributions computed for HeND 2500, 5000 and 9000 with V(D_e = 0.65 cm^{-1}; r_e = 4.1 Å; a = 1 $Å^{-1}$) at 0.37 K

8.4 Conclusion

This study has shown that in a full atomic description with quantum effective potential the dopants undergo a diffusion through the HeND by Brownian motion. The mechanism of dissociation obeys different rules depending on the excitation energy deposited in the system. Below the threshold of 2 eV molecular iodine can vibrate in a continuum of vibration modes because it is computed classically. Likewise, near the molecular iodine fragmentation limit, iodine atoms diffuse and recombine into vibrating molecules on a time scale from picoseconds to nanoseconds. This recombination is followed by an evaporation of helium atoms which dissipates the energy liberated during the formation of molecular iodine. The results are consistent with the experimental reference for excitation energy twice higher than used in our simulations. Our computed velocity distributions peak at lower energies than the experimentally studied molecules CF_3I and CH_3I.

The computed simulations are perfomed for HeND with zero angular momentum (L = 0). The extension of this work would be to study the effect of the rotation on the diffusion and on the photodissociation of the dopants. It clearly appears that the previous phenomenon will induce an anisotropy in term of velocity and fragment size distributions because of the dopants proximity near the surface of the nanodroplets.

Chapter 9

Rotational and vibrational motion of I_2 in HeND

9.1 Introduction

The first spectroscopic experiment with doped HeND was performed in 1993 on embedded SF_6 molecules which were vibrationally excited [122]. This experiment showed that the absorption bands were sharp. Likewise in 1995 the rotational spectrum of the same molecule was resolved [35]. This experiment provided information about the nanodroplet temperature. The Grebenev's experiment on OCS [36] for its part, indicated the superfluid nature of HeND. The interest of the numerical study resides on the calculation of rotational and vibrational relaxation time of a molecular iodine. Indeed according to Figure 8.6 the translational relaxation is very efficient. It is interesting to examine the rate of relaxation for other motions like rotation and vibration. In fact, molecular dopants hitting the cold HeND carry thermal rotational and potentially vibrational energy in addition to translational energy.

9.2 Methodology

To study the rotational excitation of the molecular iodine, we use a code which allows the molecule to rotate for a given rotational energy. This code modifies the velocities of the iodine atoms as seen in section 4.7 of the thesis. The vibrational excitation of the molecules is done by the photodissociation method described in subsection 8.2.1.

9.3 Rotational relaxation

The idea is to study rotating iodine molecule at room temperature hitting a HeND and follow its relaxation. The molecular iodine has been excited for an average rotational energy at 298 K in a HeND containing 5000 atoms for the He-He potential at 0.37 and 0.5 K (Appendix A). This has been realised by a code written during the present work whose protocol is to compute the probability of occupying a rotational states according to the Boltzmann distribution.

$$p_{\mathrm{J}} = \frac{(2\mathrm{J}+1)\exp\left(-\mathrm{E}^{\mathrm{J}}_{\mathrm{rot}}/k_B\mathrm{T}\right)}{\sum_{j}^{j_{max}}(2\mathrm{J}+1)\exp\left(-\mathrm{E}^{\mathrm{J}}_{\mathrm{rot}}/k_B\mathrm{T}\right)} \tag{9.1}$$

where

$$\mathrm{E}^{\mathrm{J}}_{\mathrm{rot}} = \mathrm{BJ}\,(\mathrm{J}+1) \tag{9.2}$$

Then, the average rotational energy at 298 K to apply to molecular iodine is about $\langle \mathrm{E}_{\mathrm{rot}} \rangle \simeq k_B\mathrm{T}$ $\simeq 207\,\mathrm{cm}^{-1}$. The rotational energy corresponds to a linear velocity of 197.61 m/s applied to each iodine atom. Indeed, the angular momentum depends on the angular velocity related to linear velocity and the moment of inertia. Then a MD calculation is launched with 5,000 time steps of 10 fs giving a physical simulated time of 50 ps. The kinetic energy of each iodine atom is registered and plotted in Figure 9.1 as a function of time.

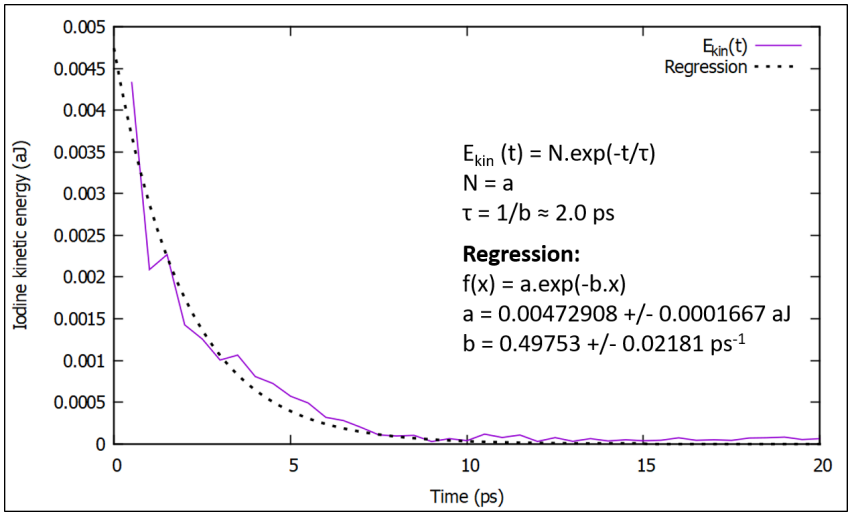

(a) Rotational energy relaxation of I_2 in HeND with He-He Morse potential V(D_e = 0.65 cm^{-1}; r_e = 4.1 Å; a = 1 $Å^{-1}$) at 0.37 K

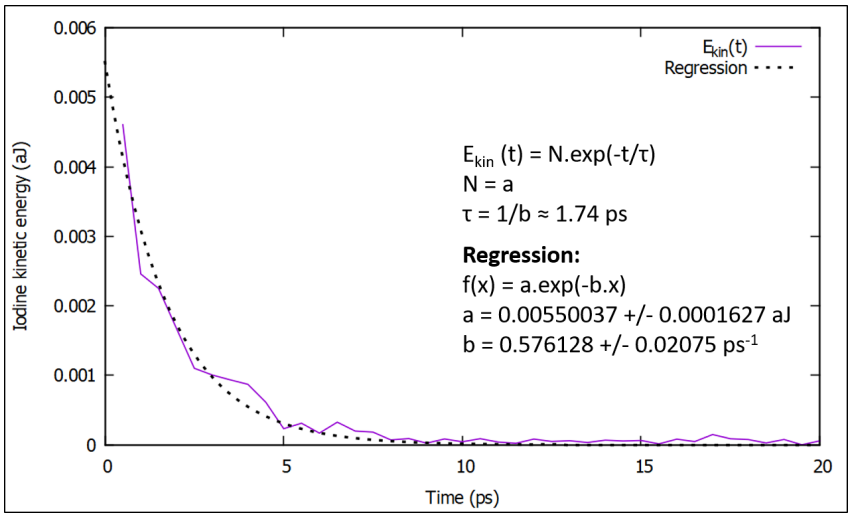

(b) Rotational energy relaxation of I_2 in HeND with He-He Morse potential V(D_e = 0.8 cm^{-1}; r_e = 4.1 Å; a = 1 $Å^{-1}$) at 0.5 K

Figure 9.1: Rotational energy relaxation of I_2 in HeND with different He-He Morse potentials

The upper graph represents the rotational energy dissipation of molecular iodine based on the kinetic energies of iodine atoms in HeND simulated with the He-He effective potential at 0.37 K. The lower graph is for the He-He effective potential at 0.5 K. In both graphics, an exponential fit has been performed in order to determine the time constant which gives an insight about the rotational relaxation time. For the He-He potential at 0.37 K, the time constant, represented by $b = 1/\tau$ is equal to 0.50 ps^{-1} and for the He-He potential at 0.5 K, 0.58 ps^{-1}. The relaxation is similar in both potentials where at 0.37 K it is equal to 2 ps and at 0.5 K 1.74 ps. This process occurs in few picoseconds in the nanodroplet whereas the experiments observe rotational relaxations with microwave spectroscopies on cyanoacetylene [123, 124], where the time scale is about the nanosecond. According to Choi *et al.* the rotational relaxation [93] is

very slow for heavy rotors where the rotational constant is below 1 cm^{-1} like molecular iodine (B = 0.03737 cm^{-1}).

At the end of the calculation and by applying the equipartition theorem on rotational motion (E = $3k_B$T/2) the temperature of the molecular iodine can be calculated. The obtained value is in the vicinity of 3 K which means that the rotating molecule is still thermally activated relative to the droplet.

9.4 Vibrational relaxation

The idea is to see what happens to a thermal vibrating molecular iodine at room temperature entering a cold HeND. Indeed the main goal is to determine the vibrational relaxation time of molecular iodine in HeND. The simulation has been done for the He-He effective potential at 0.5 K. The molecular iodine has been excited according to the average vibrational energy at 298 K in a HeND containing 5000 atoms. This has been realised by a code written during the thesis whose protocol is to compute the probability of occupying a vibrational states according to the Boltzmann distribution.

$$p_v = \frac{\exp\left(-\left(\mathrm{E}(v)-\mathrm{E}_0\right)/k_B\mathrm{T}\right)}{\sum_{v}^{v_{max}} \exp\left(-\left(\mathrm{E}(v)-\mathrm{E}_0\right)/k_B\mathrm{T}\right)} \tag{9.3}$$

where

$$\mathrm{E}(v) = \omega_e\left(v+\frac{1}{2}\right) - x_e\left(v+\frac{1}{2}\right)^2 \tag{9.4}$$

Then the average vibrational energy at 298 K applied on the molecular iodine is about $\langle \mathrm{E_{vib}} \rangle \simeq 120\,cm^{-1}$ which is equivalent to a linear velocity of 105.48 m/s for each iodine atom. Then, a chain of 21 MD calculations was launched, where each simulation was done with 5,000,000 time steps of 10 fs, giving a physical simulated time of 1.05 µs. The kinetic energy of each iodine atom is stored and plotted in Figure 9.2 as a function of time. Like for photodissociation simulations the system is expected to equilibrate by evaporative cooling but the simulation does not show vibrational relaxation on this time scale. In fact one would expect a damped oscillation but Figure 9.2 does not show any indication of damping. The kinetic energy still remains as high as the initial one at 120 cm^{-1}. Experimentally, there is exception like HF monomer which relaxes after 0.5 ms according to the work of Nauta and Miller [125]. Figure 9.2 shows the first picoseconds of the final simulation n°21 to 1.05 μs. By applying the equipartition theorem for vibrational motion (E=k_BT) the associated temperature is 173 K.

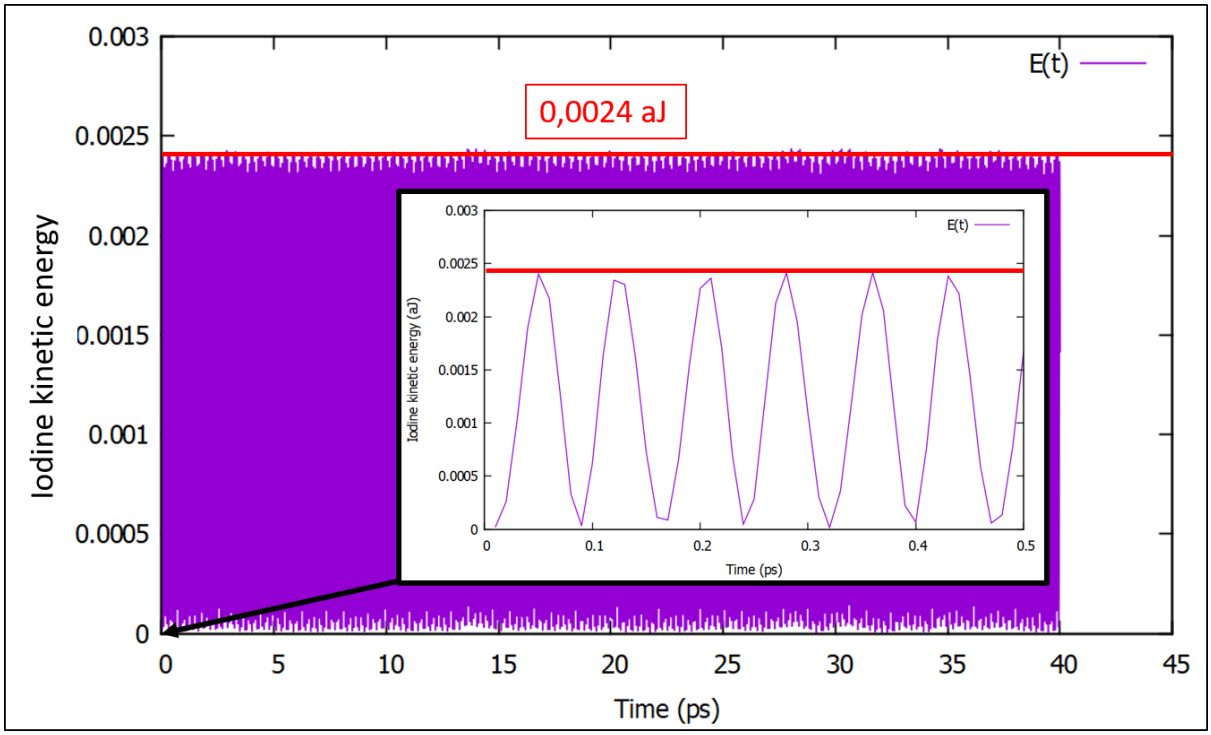

Figure 9.2: Vibrational energy relaxation of I_2. The inset shows an expanded section near the beginning

Considering the surprising result an investigation on a modified I-I Morse potential has been done by modifying the I-I well depth. According to the results presented in Table 9.1 and plotted in Figure 9.3, an extrapolation of relaxation time for I-I Morse potential can be done and gives a time equal to 0.59 s compared to DFT calulations made by Vilà *et al.* who found that the relaxation process of I_2 occurs on the nanosecond time scale [126].

Well depth D_e (cm^{-1})	**Relaxation time (ps)**
375	2
750	15
1500	60
3000	4500
6000	1,000,000

Table 9.1: Relaxation time of vibrating I_2 for modified well depth I-I Morse potentials in HeND computed by He-He Morse potential V(D_e = 0.80 cm^{-1}; r_e = 4.1 Å; a = 1 $Å^{-1}$) at 0.5 K

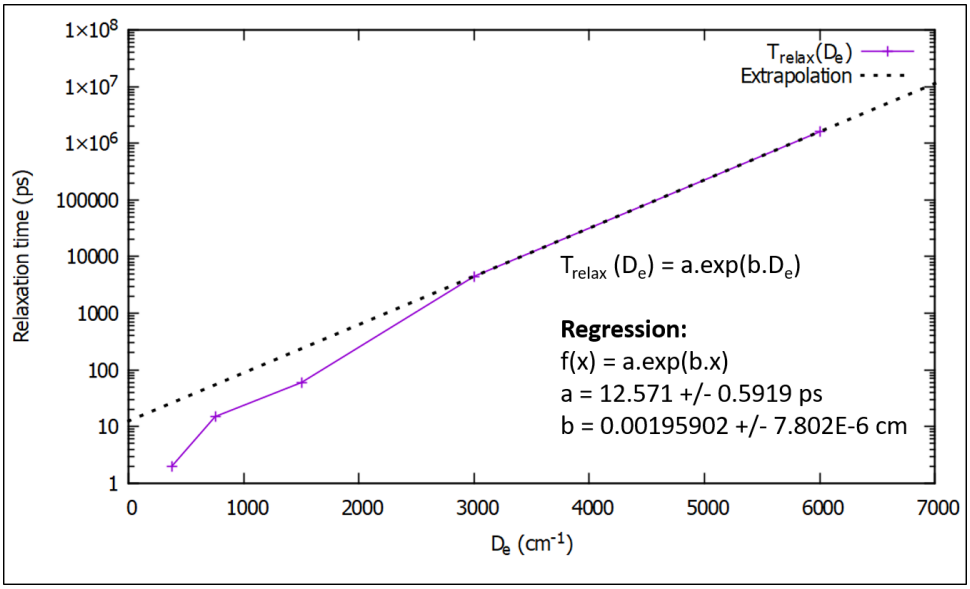

Figure 9.3: Graph of relaxation time of vibrating I_2 for modified well depth I-I Morse potentials in HeND computed by He-He Morse potential V(D_e = 0.80 cm^{-1}; r_e = 4.1 Å; a = 1 $Å^{-1}$) at 0.5 K

9.5 Conclusion

This work has shown exploratory studies of rotational and vibrational relaxation of molecular iodine. In the HeND the rotational relaxation excited at an average energy representative of 298 K exhibits a slow relaxation considering certain diatomic molecules studied experimentally. Moreover, this type of experiments was important to define the temperature of the nanodroplets. By this way the superfluid nature of HeND has been proved by resolving the rotational spectra.

An absence of vibrational relaxation of molecular iodine is another surprising observation found by MD with quantum effective potential at 0.5 K. The numerical experiments at 0.37 K would give the same results considering it is softer than the former one. For now there are no experiments on molecular iodine relaxation to correlate with the observations seen in this thesis.

Chapter 10

Rotating droplets: deformation and fragmentation

10.1 Introduction

Knowing that the droplets found in the gas expansion should carry angular momentum and considering X-ray experiments [45, 46, 127, 128], we decided to use our atomistic model to study distortions of rotating droplets. The phenomenon of shape distortion due to rotation is well known from continuum model [81] within the liquid drop model.

10.2 Method and protocol

The calculations has been made on three sizes of HeND : 2497, 4995, 8996 with two Morse potentials: V(D_e = 0.8 cm^{-1}; r_e = 4.1 Å; a = 1 Å^{-1}) at 0.5 K and V(D_e = 0.65 cm^{-1}; r_e = 4.1 Å; a = 1 Å^{-1}) at 0.37 K. Some extra work has been done in order to determine the pattern of simple and multiple splitting according to imposed angular momentum *a contrario* of the study of Vilesov *et al.* [47]. They have determined the angular velocity experimentally and theoretically by DFT calculations where they found respectively $\omega_{exp} = 2.26 \times 10^9$ rad/s and $\omega_{exp} = 2.23 \times 10^9$ rad/s. In our simulation, a range of angular momenta has been imposed from $2\hbar$/atom to 12 $\hbar$/atom giving angular velocity from 4.03×10^9 rad/s to 6.31×10^{10} rad/s. The convention for units in our MD calculations is $\hbar$/atom for angular momentum.

The starting point is an equilibration with a thermostat at 0.37 K or at 0.5 K depending on which Morse potential is used with the Berendsen thermostat [64]. 100,000 time steps of 10 fs has been simulated giving a physical time of 1 ns. The same operation is repeated but for a simulation at constant energy giving a relative energy fluctuation about 10^{-7}. Finally, the simulations of HeND rotation have been done over 125,000 time steps of 10 fs on the Y-axis,

the angular momentum L_x and L_z are set to zero. All the simulations were integrated with the Velocity Verlet algorithm [61].

10.3 Results and discussion

10.3.1 He2500

Numerical experiments of rotating pure helium clusters containing 2497 atoms have been done for both Morse potentials V(D_e = 0.65 cm^{-1}; r_e = 4.1 Å; a = 1 $Å^{-1}$) at 0.37 K and V(D_e = 0.80 cm^{-1}; r_e = 4.1 Å; a = 1 $Å^{-1}$) at 0.5 K. The results are presented in Figures 10.1 and 10.2 which show the evolution of the principal moments of inertia for different angular momenta. Indeed, the analysis of this evolution is a useful tool to visualise the shape distortions of pure rotating HeND. All simulations start with an essentially spherical droplet (L = 0 $\hbar$/atom) which implies that $I_B \simeq I_C \simeq I_A$.

In Figure 10.1.A in page 103 for L = 2 $\hbar$/atom, one clearly observes an evolution towards a situation with $I_B \simeq I_C > I_A$ which corresponds to a prolate shape between 600 ps and 1100 ps, which means elongation, followed by a further increase after 1100 ps indicating a fission process [129]. For an angular momentum of L = 4 $\hbar$/atom, shown in Figure 10.1.B, the evolution follows a similar general scheme with a strong asymmetry and fission. At even higher L values in Figures 10.1.C-F, the droplet shape evolves towards a more oblate structure, $I_C > I_B \simeq I_A$, and very rapid fragmentation which manifests itself by a growth $I_{ABC} \sim t^2$. Indeed, all elements of the inertia tensor (Appendix B) grow proportional to t^2 if the fragments are separated with constant final velocities.

In Figure 10.2.A on page 103 for L = 2 $\hbar$/atom for He-He interaction computed with Morse potentials V(D_e = 0.65 cm^{-1}; r_e = 4.1 Å; a = 1 $Å^{-1}$) at 0.37 K, the evolution of the principal moments of inertia shows an elongation of the cluster corresponding to a prolate form with a kind of stabilisation according to the plateau between 800 ps and 1100 ps. For other angular momenta, Figures 10.2.B-F show the fast fragmentation as explained above.

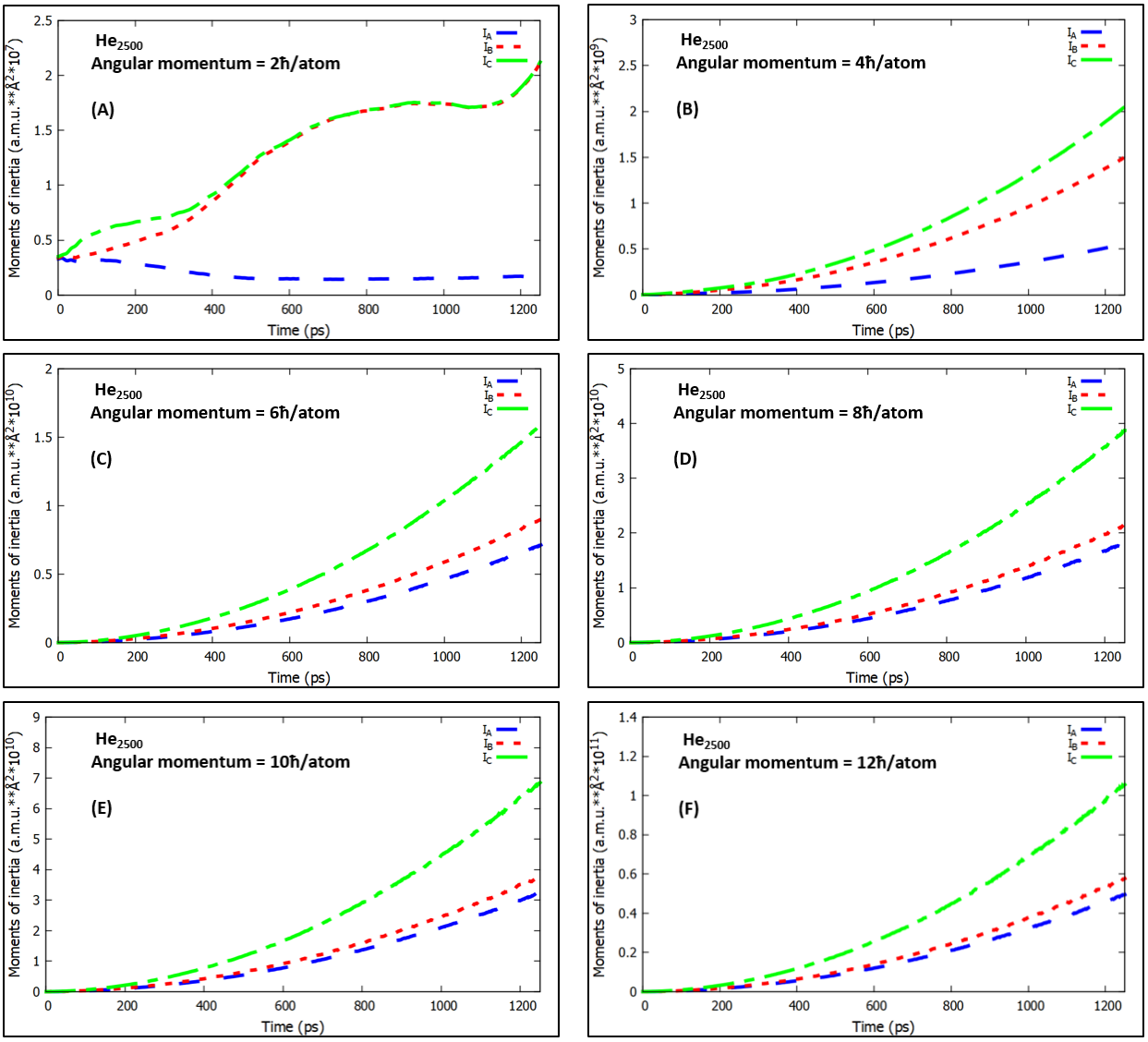

Figure 10.1: Time evolution of principal moments of inertia of HeND 2500 with V(D_e = 0.8 cm^{-1}; r_e = 4.1 Å; a = 1 $Å^{-1}$) at 0.5 K

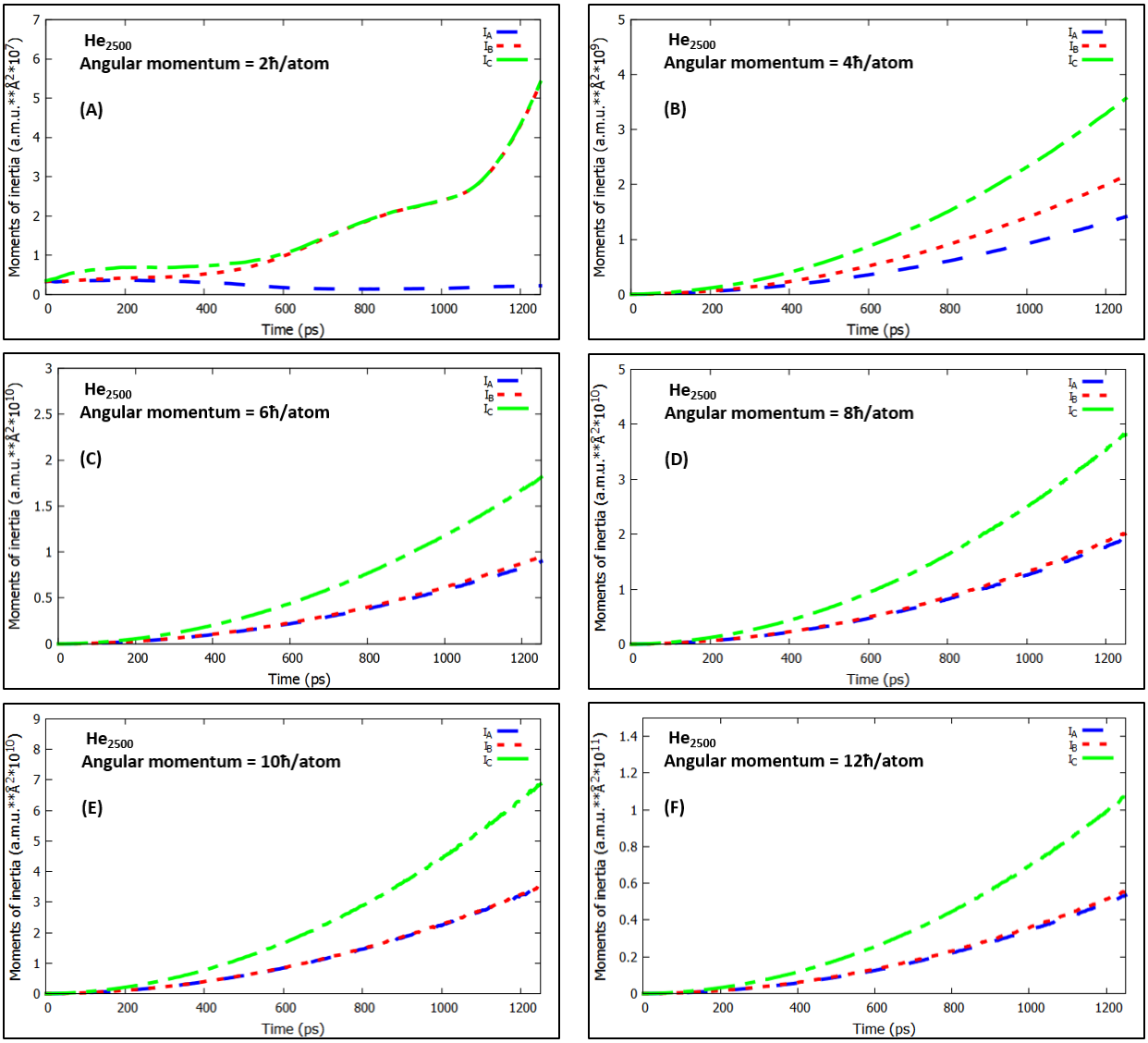

Figure 10.2: Time evolution of principal moments of inertia of HeND 2500 with V(D_e = 0.65 cm^{-1}; r_e = 4.1 Å; a = 1 $Å^{-1}$) at 0.37 K

Figure 10.3a shows outcomes for L = 2 $\hbar$/atom after 1.25 ns for the different potentials used in this work. This result presents the binary fission for the calculation at 0.37 K and at 0.5 K. This distortion is more pronounced for the effective He-He Morse potential at the lower temperature.

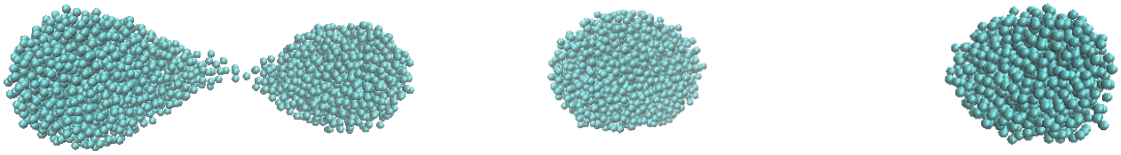

(a) HeND 2500 simulated with V(D_e = 0.8 cm^{-1}; r_e = 4.1 Å; a = 1 $Å^{-1}$) at 0.5 K at t = 1.25 ns

(b) HeND 2500 simulated with V(D_e = 0.65 cm^{-1}; r_e = 4.1 Å; a = 1 $Å^{-1}$) at 0.37 K at t = 1.25 ns

Figure 10.3: Comparison of MD outcomes on rotation at 2 $\hbar$/atom

From L = 4 $\hbar$/atom to L = 12 $\hbar$/atom in Figure 10.1 and 10.2, the fragmentation evolves from the situation described in Figure 10.3 to multiple oblate splitting presented in Figure 10.4.

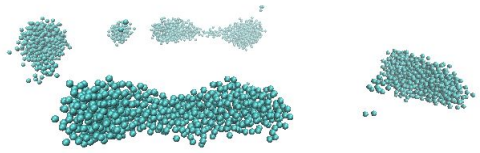

Figure 10.4: Multiple splitting of HeND 2500 simulated with V(D_e = 0.65 cm^{-1}; r_e = 4.1 Å; a = 1 $Å^{-1}$) at 0.37 K at t = 1.25 ns

The CLUSTER code also calculates the κ asymmetry parameter for each HeND. This variable computed from the rotational constants varies from -1 for prolate ($I_B \simeq I_C > I_A$) shape to +1 for oblate ($I_C > I_B \simeq I_A$). It brings direct information related to distortion informations. It is expressed by the following formula:

$$\kappa = \frac{2I_B - I_A - I_C}{I_A - I_C} \tag{10.1}$$

The evolution of asymmetry parameter has been followed for both potentials and it is represented in Figures 10.5a and 10.5b. This representation allows to show the shape evolution for several angular momentum values in a simple graph. In Figure 10.5a, for L = 2 $\hbar$/atom and L = 4 $\hbar$/atom, the asymmetry parameter indicates an evolution to prolate fission. From L = 6 $\hbar$/atom to L = 12 $\hbar$/atom the trend is an evolution to quasi-oblate fission. In Figure 10.5b, the same observations can be made but from L = 6 $\hbar$/atom to L = 12 $\hbar$/atom one observes a total oblate fission.

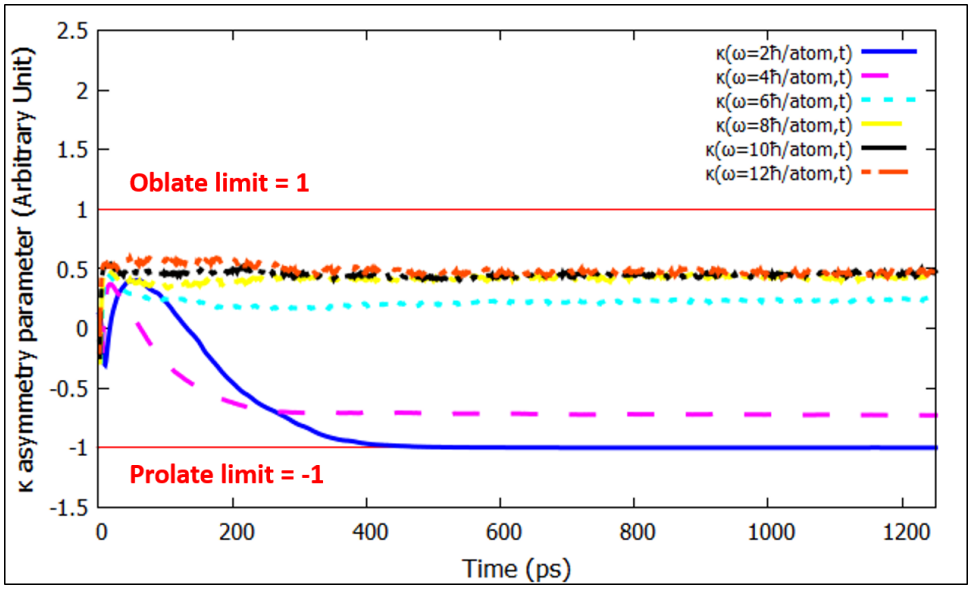

(a) Time evolution of the asymmetry parameter for HeND 2500 for V(D_e = 0.8 cm^{-1}; r_e = 4.1 Å; a = 1 $Å^{-1}$) at 0.5 K

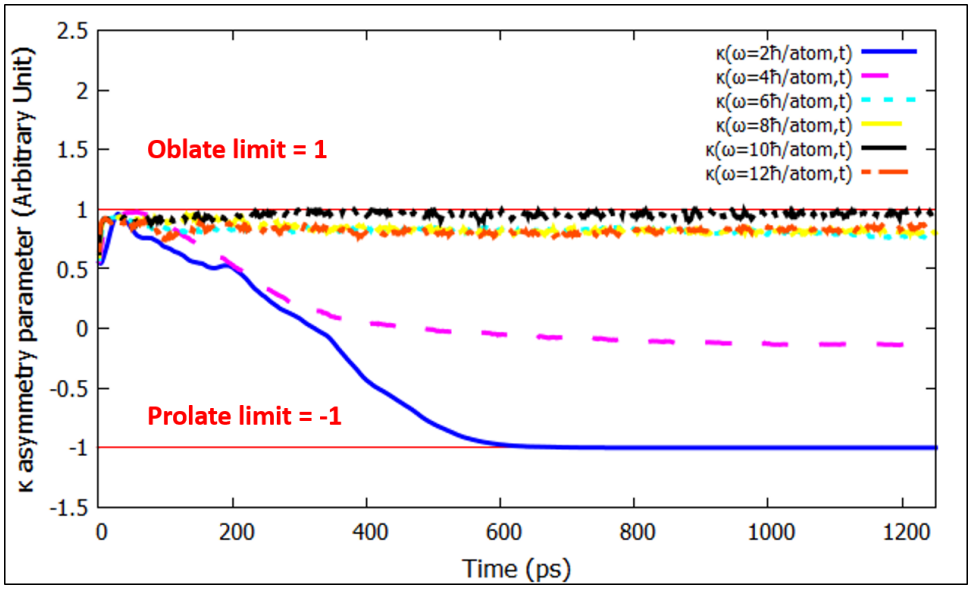

(b) Time evolution of the asymmetry parameter for HeND 2500 for V(D_e = 0.65 cm^{-1}; r_e = 4.1 Å; a = 1 $Å^{-1}$) at 0.37 K

Figure 10.5: Time evolution of the asymmetry parameter for HeND 2500 for different potentials

10.3.2 He5000

Figure 10.6 on page 108 represents the time evolution of the principal moments of inertia for a range of angular momenta starting from 2 ħ/atom to 12 ħ/atom on a pure HeND composed of 4995 atoms and simulated with the Morse effective potential V(D_e = 0.8 cm^{-1}; r_e = 4.1 Å; a = 1 $Å^{-1}$) at 0.5 K. In Figure 10.6.A for L = 2 ħ/atom, we observe a structure where $I_C > I_B > I_A$

which seems to be a transition from oblate to prolate without fission. For L = 4 $\hbar$/atom in Figure 10.6.B also shows the principal moments of inertia ordered like L = 2 $\hbar$/atom with a trend where I_B tends to be equal to I_A. This structure represents a stable oblate shape. At L = 4 $\hbar$/atom in Figure 10.6.C, I_B evolves to reach I_C which is characteristic to a prolate shape. This latter assumption is well confirmed in Figure 10.6.D at L = 8 $\hbar$/atom where $I_B \simeq I_C > I_A$ meaning a stable prolate form with the appearance of the plateau with could evolve by extending the simulation. In Figure 10.6.E-F, we observe the prolate fission because $I_B \simeq I_C > I_A$ with I_B and I_C proportional to t^2 which indicates an expansion at constant velocity.

For calculations with the Morse effective potential V(D_e = 0.8 cm^{-1}; r_e = 4.1 Å; a = 1 $Å^{-1}$) at 0.37 K in page 110, Figure 10.8.A at L = 2 $\hbar$/atom presents a transition to stable oblate seen in Figure 10.6.B for the case of L = 4 $\hbar$/atom above. Figure 10.8.B is similar to Figure 10.6.D with a short plateau and $I_B \simeq I_C > I_A$ specific for a stable prolate cluster. Figure 10.8.C shows a prolate fission where I_B and I_C are proportional to t^2. A fission without symmetry is shown in Figure 10.8.D where all moments of inertia are proportional to t^2. This represents a transition phase between prolate to oblate fission. At higher angular momenta Figure 10.8.E represents an evolution to oblate fission, which is completely oblate for L = 12 $\hbar$/atom where $I_C > I_B \simeq I_A$.

The multiple splitting case occurs at angular momenta above 12 $\hbar$/atom according to Figure 10.6. The transition from oblate to prolate shape takes place between 2 $\hbar$/atom to 4 $\hbar$/atom and the prolate to multiple splitting is around 6 to 10 $\hbar$/atom according to Figure 10.8. An investigation on this has been done with the Morse effective potential at 0.37 K for HeND 4997. The data in Table 10.1 on page 112 show the number of subclusters, evaporated atoms according to the angular momentum of the droplet. Subclusters are arbitrarily defined as small structures containing a minimum of 10 helium atoms.

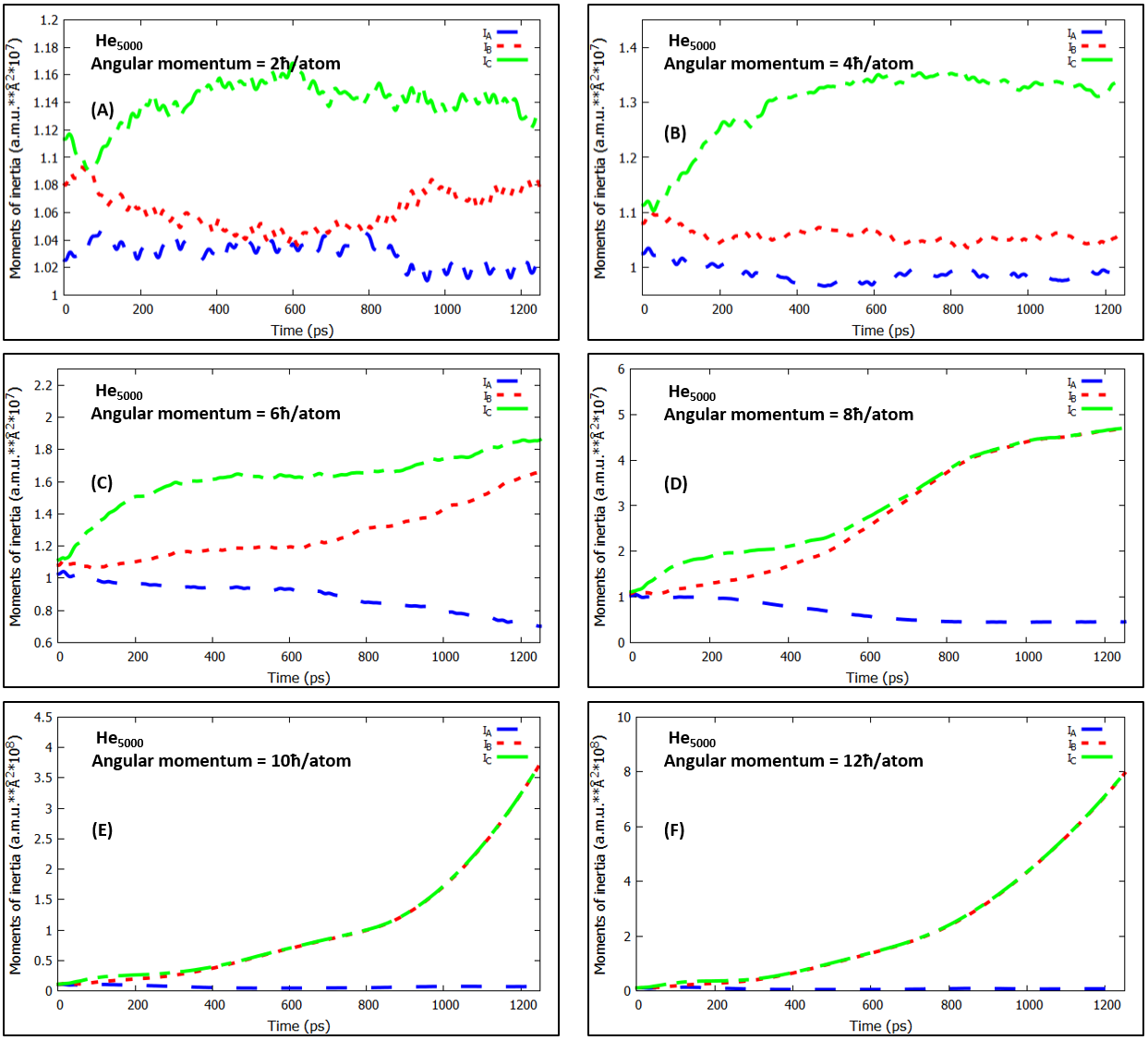

Figure 10.6: Time evolution of principal moments of inertia of HeND 5000 with V(D_e = 0.8 cm^{-1}; r_e = 4.1 Å; a = 1 $Å^{-1}$) at 0.5 K

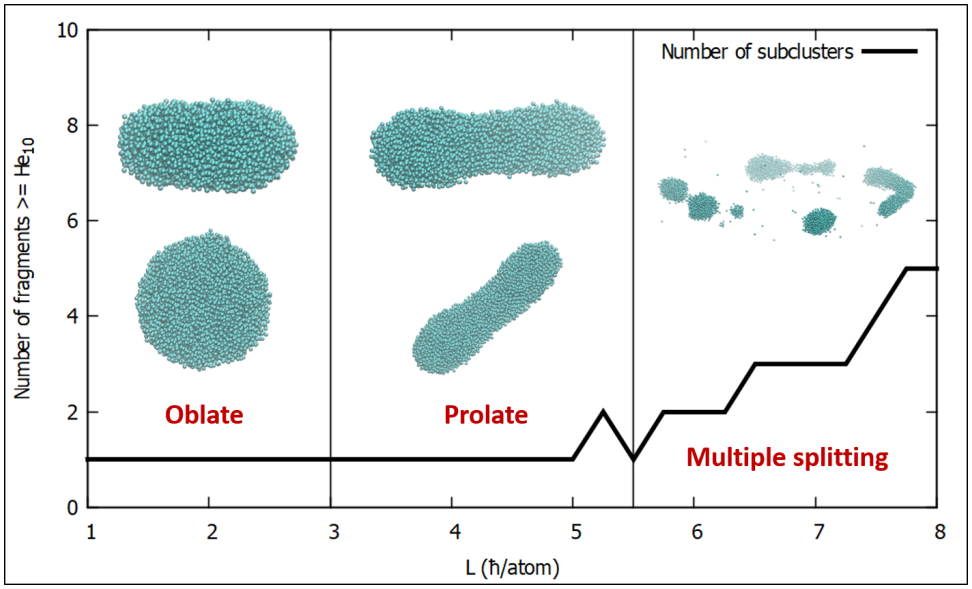

Figure 10.7: Shape of HeND 5000 depending on the angular momentum

To determine where transitions oblate/prolate occur Figure 10.7 presents the number of subclusters as a function of the angular momentum and the shape is reported. The transition from oblate to prolate stable shape appears near L = 3 $\hbar$/atom. A remark is that the prolate shape is observed at strong angular momentum. Then between L = 5 $\hbar$/atom and L = 6 $\hbar$/atom, there is the transition between prolate fission and oblate fission which can be named multiple splitting. At higher angular momenta, annular forms are observed giving subclusters. With the CCA (section E.3), it is possible to find the different clusters and store their configurations (cfg) in a cfg file (section 4.6 and Appendix D.1) in order to analyse them by MD.

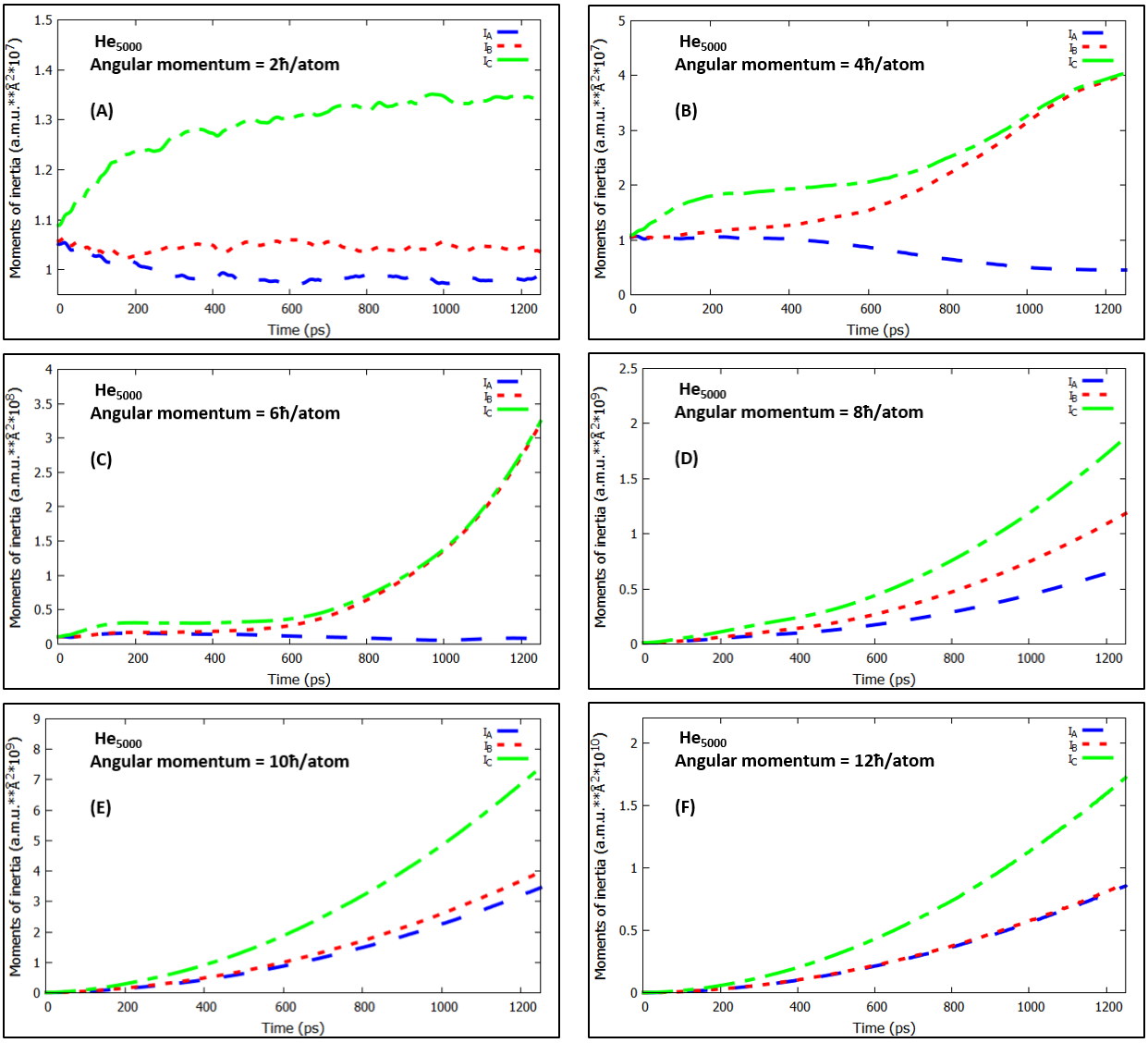

Figure 10.8: Time evolution of principal moments of inertia of HeND 5000 with V(D_e = 0.65 cm^{-1}; r_e = 4.1 Å; a = 1 $Å^{-1}$) at 0.37 K

The evolution of HeND 5000 distortions is followed looking the asymmetry parameter for both potentials along the MD. Figure 10.9a shows that for L = 2 $\hbar$/atom and L = 4 $\hbar$/atom the nanodroplet oscillates between a prolate and a oblate shape. By extending the simulation this oscillating behaviour could be observed as a droplet relaxation. At higher angular momentum, the HeND tends to become prolate with time after being slightly oblate. This phenomenon is faster when the angular momentum is larger. In Figure 10.9b, for L = 2 $\hbar$/atom, we observe an oblate oscillation.

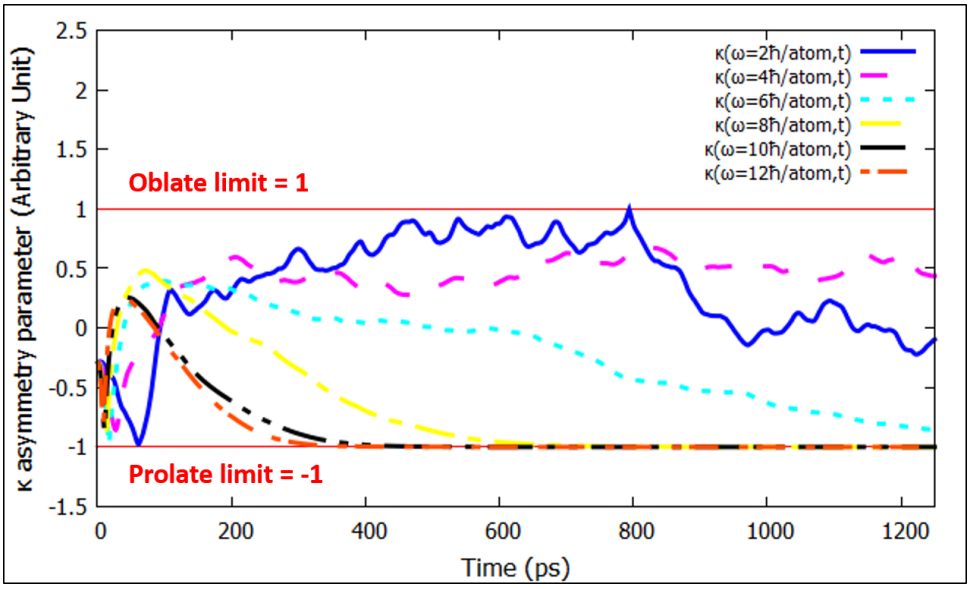

(a) Time evolution of the asymmetry parameter for HeND 5000 for V(D_e = 0.8 cm^{-1}; r_e = 4.1 Å; a = 1 $Å^{-1}$) at 0.5 K

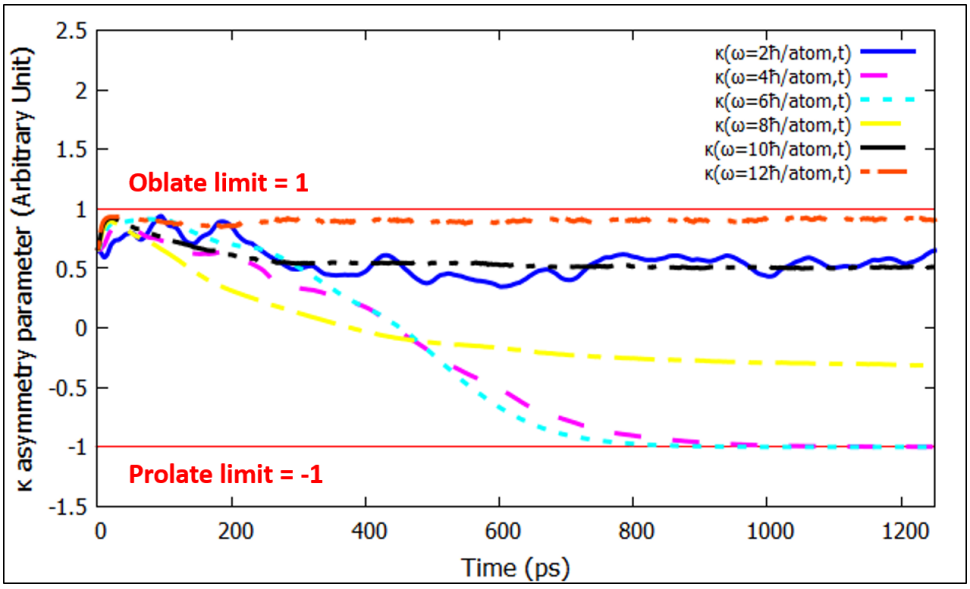

(b) Time evolution of the asymmetry parameter for HeND 5000 for V(D_e = 0.65 cm^{-1}; r_e = 4.1 Å; a = 1 $Å^{-1}$) at 0.37 K

Figure 10.9: Time evolution of the asymmetry parameter for HeND 5000 for different potentials

For L = 4 ħ/atom and L = 6 ħ/atom, the droplets become rapidly prolate. At the beginning the shapes of HeND is olate then evolve close to zero which indicates a transition state to finish as prolate. At higher angular momenta, we observe an oblate shape. The analysis of distortions gives information on the shape but not on the type of fragmentation of the droplet.

L ($\hbar$/atom)	**Total fragments**	**Fragments $\geq$ He_{10}**	**Fragment size (He atoms)**	**He atoms evap.**
2	1	1	4997	0
2.25	1	1	4997	0
2.5	1	1	4997	0
2.75	1	1	4997	0
3	1	1	4997	0
3.25	1	1	4997	0
3.5	1	1	4997	0
3.75	1	1	4997	0
4	1	1	4997	0
4.25	1	1	4997	0
4.5	1	1	4997	0
4.75	1	1	4997	0
5	1	1	4997	0
5.25	4	2	2339 2656	2
5.5	2	1	4996	1
5.75	8	2	2402 2589	6
6	7	2	1631 3361	5
6.25	8	2	1725 3265	7
6.5	21	3	1257 1512 1808	17
6.75	28	3	1071 1476 2425	25
7	51	3	169 1674 3106	48
7.25	66	3	1196 1569 2168	62
7.5	87	4	1049 1075 1190 1600	83
7.75	135	5	17 518 1328 1463 1540	129
8	193	5	64 799 1294 1302 1342	186
8.25	541	6	22 267 761 803 1255 1351	532
8.5	605	6	54 262 614 1077 1175 1208	588
8.75	659	7	43 465 495 583 713 779 1261	645
9	711	7	55 343 609 660 679 864 1064	691
10	601	11	17 24 59 144 301 411 498 552 764 810 820	583
12	1001	21	11 12 18 27 29 35 36 46 47 64 73 134 174 190 289 340 354 380 482 558 665	946

Table 10.1: Number of fragments, sublusters and their sizes and evaporated helium atoms depending on angular momentum for HeND 5000

10.3.3 He9000

Figure 10.10 represents the different moments of inertia for a range of angular momenta starting from 2 $\hbar$/atom to 12 $\hbar$/atom on a pure HeND composed of 8996 atoms and simulated with the Morse potential V(D_e = 0.8 cm^{-1}; r_e = 4.1 Å; a = 1 $Å^{-1}$) at 0.5 K. Figures 10.10.A-B shows a stable oblate shape without fission of the cluster. The transition from stable oblate to stable prolate occurs between L = 6 $\hbar$/atom and L = 12 $\hbar$/atom according to Figures 10.10.C-F with I_B which tends to reach I_C to finally have a prolate structure $I_B \simeq I_C > I_A$. These simulations need to be pushed further in time to clearly see the angular momentum effects on HeND like fragmentation.

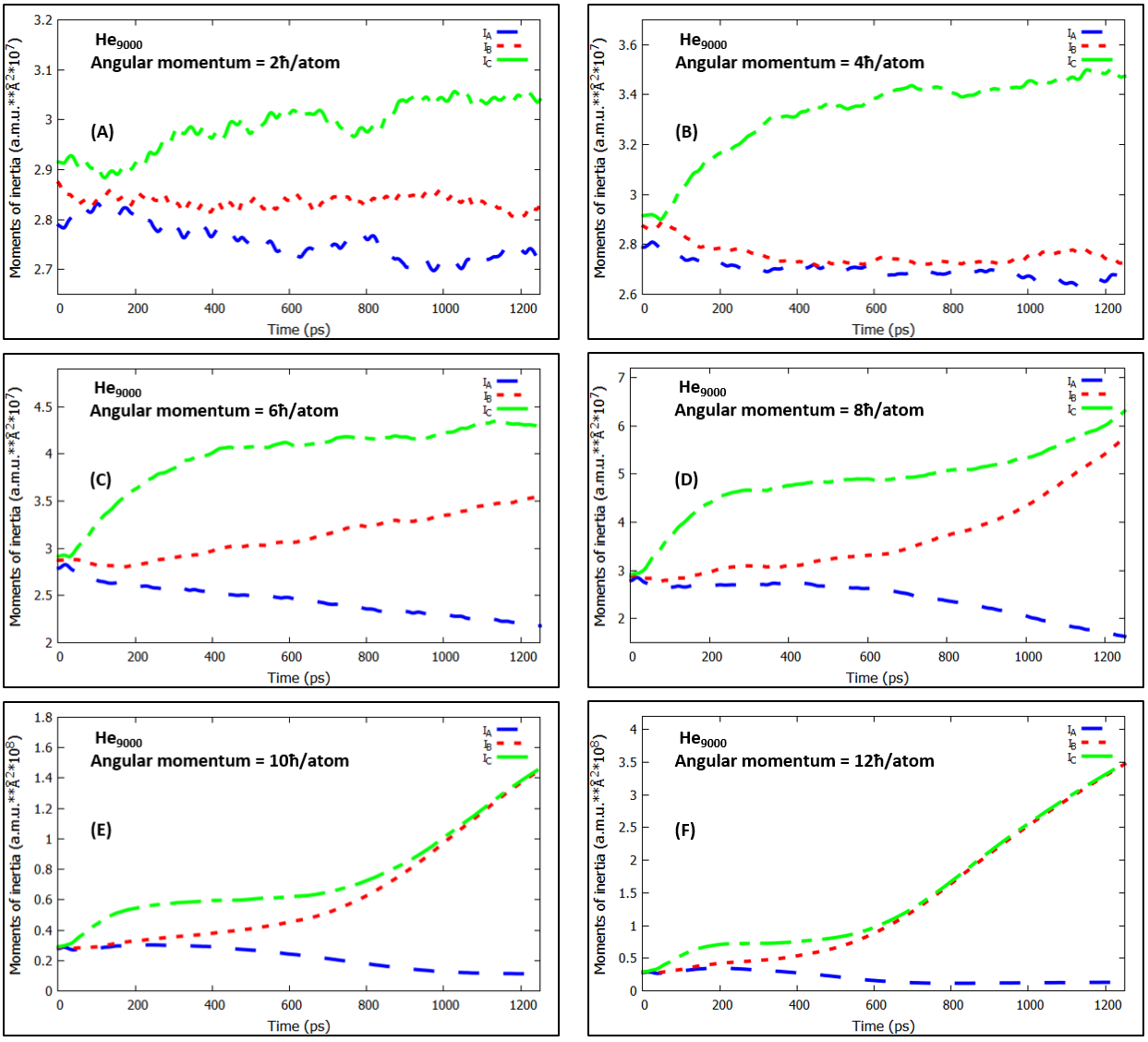

Figure 10.10: Time evolution of principal moments of inertia of HeND 9000 with V(D_e = 0.8 cm^{-1}; r_e = 4.1 Å; a = 1 $Å^{-1}$) at 0.5 K

The same study has been done for V(D_e = 0.65 cm^{-1}; r_e = 4.1 Å; a = 1 $Å^{-1}$) at 0.37 K in Figure (10.11). Figures 10.10.A-C shows a stable oblate shape transition where $I_C > I_B > I_A$. At L = 8 $\hbar$/atom in Figure 10.10.D there is a transition to prolate shape. This is confirmed by Figures 10.10.E-F where $I_B \simeq I_C > I_A$.

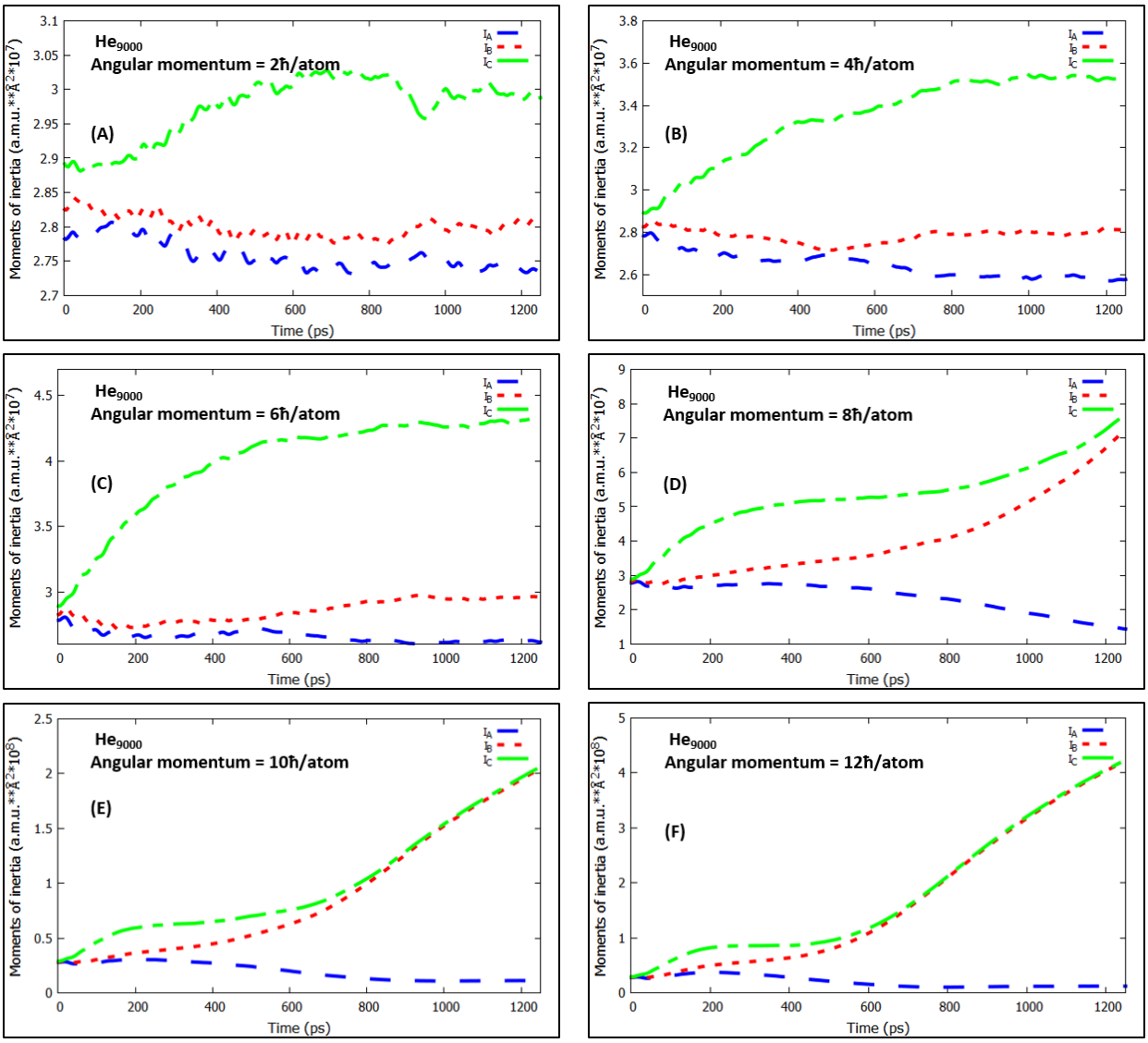

Figure 10.11: Time evolution of principal moments of inertia of HeND 9000 with V(D_e = 0.65 cm^{-1}; r_e = 4.1 Å; a = 1 $Å^{-1}$) at 0.37 K

As a complement to the moments of inertia analysis which showed no fragmentations, the asymmetry parameter is given in Figure 10.12. For L = 2 $\hbar$/atom and L = 4 $\hbar$/atom in Figures 10.12a and 10.12b we observed shape oscillations of the HeND. At higher angular momenta, the droplets undergo a transition between stable oblate to stable prolate form.

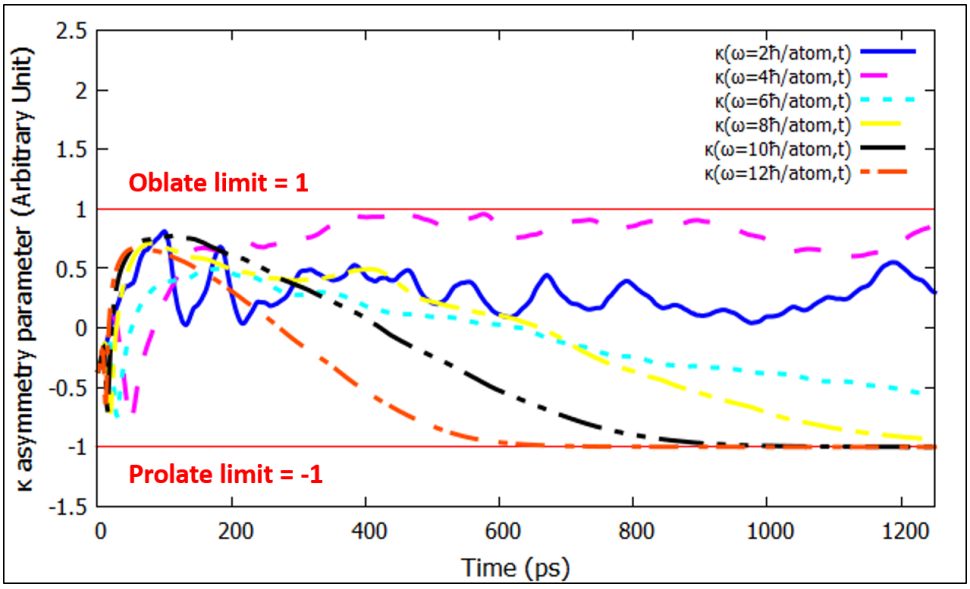

(a) Time evolution of the asymmetry parameter for HeND 9000 for V(D_e = 0.8 cm^{-1}; r_e = 4.1 Å; a = 1 $Å^{-1}$) at 0.5 K

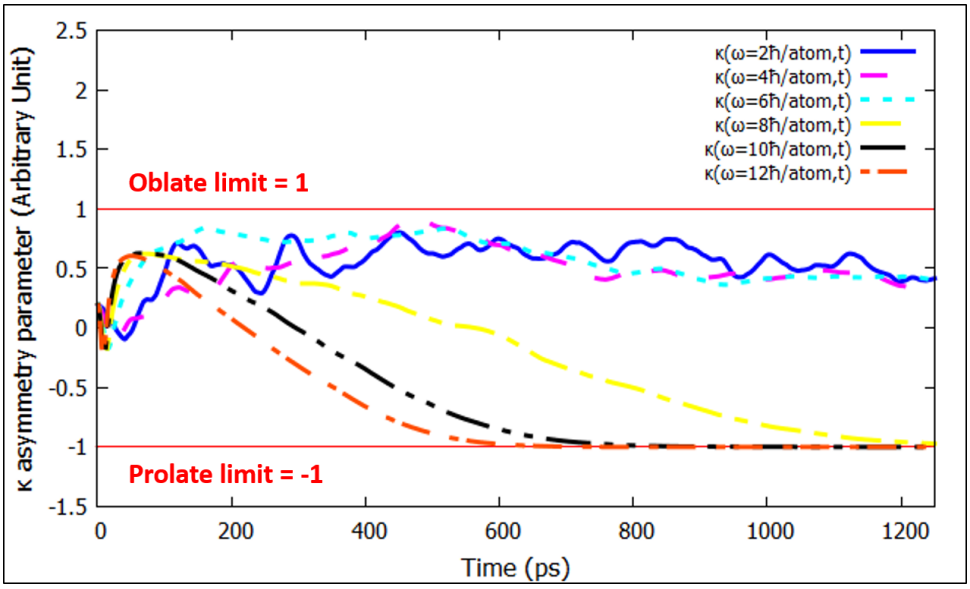

(b) Time evolution of the asymmetry parameter for HeND 9000 for V(D_e = 0.65 cm^{-1}; r_e = 4.1 Å; a = 1 $Å^{-1}$) at 0.37 K

Figure 10.12: Time evolution of the asymmetry parameter for HeND 9000 for different potentials

10.4 Conclusion

The study of the rotation of HeNDs of different sizes shows similar outcomes with the experimental work depending on the angular momentum. The droplets undergo deformations starting from a spherical nanodroplet at rest to an oblate and/or prolate shape before complete

splitting. The shape depends on the number of helium atoms present in the cluster. Indeed, the more there are atoms the less the droplet is deformable. The moments of inertia and the κ asymmetry parameter are diagnostics of huge help to track the phenomena of oblate and prolate expansion. An oblate expansion can be deduced by the fact that all the moments of inertia of the droplets are proportional to t^2 and $\kappa = 1$. All the subclusters or evaporated atoms explore a space whose limits are determined by an anisotropic volume. For the prolate expansion, two of three moments of inertia have to be t^2-dependent. This leads to a splitting mainly into two parts. The last pattern of expansion is the multiple splitting where the rotation causes the formation of a pre-annular to an annular splitting depending on the magnitude of the angular momentum given to the system. This phenomenon does not occur in the helium experiments. As outlook, the combination with the developed code of CCA in chapter 6 can bring physical informations on the subcluster by fragment analysis where the positions and velocities of atoms composing a subset are available. With that the study of the type of rotation, the temperature and the time of relaxation are accessible with the CLUSTER code calculations.

Chapter 11

Impact of dopants on HeND

11.1 Introduction

The doping of HeND is an important process preceeding the analysis of a dopant of interest in a liquid environment which presents weak interaction with it [130–132]. Likewise, the specific internal structure of superfluid nanodroplets with quantum vortices allows the formation of new materials which presents potential interest like the synthesis of metallic nanowires composed of silver, nickel, chromium, gold and silicon [39, 94, 133, 134] assembled from atoms evaporated by laser ablation [135–138] in the pickup cell. Moreover, the synthesis of core-shell nanoparticles [139–141] is an important part of researches on HeND which presents interest in medicine.

All the described processes have one thing in common, they all include a phase of impacts on nanodroplets. This work aims to study different phenomena which occur during the dopant impacting the HeND. The size range of the droplets is about 2500, 5000 and 9000 helium atoms. Three rare gas atoms play the role of dopant because of their simple interactions: argon, krypton and xenon. Moreover these impacts on HeND have been studied experimentally. They are easier to model than metal atoms or molecules. Xenon has an atomic mass close to the iodine atom which was the dopant in the previous simulation of photodissociation. Firstly, the general strategy of the doping simulation will be presented. Then, from the numerical experiments the average penetration depth, the angular and linear momentum transmission and the doping rate for the dopants previously mentionned are studied. The results obtained will be discussed and compared to an experimental reference [33]. Indeed, linear momentum transmission is a key part of the scattering-deflection technique for the analysis of droplets size distributions. Another quantity of interest is the velocity of the evaporated He atoms following the dopant impact. Distribution of the evaporated He atoms are computed in order to compare them to the Boltzmann distribution which would imply equilibrium is reached and then a temperature can be deduced.

Moreover, aggregation dynamics in nanodroplets is studied by multiple impacts of xenon and unveils the presence of well-known metastable structures of snowballs [142]. Helium atom organisation around the dopant atom seems crystalline which is a remarkable arrangement.

11.2 Method and protocol

To simulate the dopant impacting on the HeND a specific arrangement has been chosen. In fact, all the collisions of the rare gas dopants with the HeND take place on the surface XY of the droplet according to Cartesian space. The rotational and the linear momentum of the HeND is set to zero (L = 0 and P = 0) which ensures no distortions of the cluster which remains quasi-spherical and no translation motion in any direction of space. According to the previous conditions, the HeND is considered as a non-moving object and the collision is set on a plane of the droplet so that the motion of the dopant takes place on the orthogonal axis to the surface of impact where the initial dopant position is fixed at a sufficient large distance from the cluster (100 Å). The other velocity components are equal to zero. The idea is that the reference framework is not the laboratory but the HeND. In the experiments the droplets move rapidly in a well defined direction and hit background gas with random zero mean cartesian velocity components. Here, the dopant has the velocity of the cluster and the HeND is motionless. Both concepts represent the same collision physics. To achieve that the program (Appendix E.6), which manages the random impact point of the dopant on the HeND, computes an optimised radius of the spherical cluster which is the radius averaged over the radii on the impact surface to avoid missing shots. The point of impact and the velocity of the dopant are respectively randomly picked by a uniform and normal deviates (Appendices E.1 and E.2). The uniform deviate selects a set of coordinates on the impact surface which is within the circle determined by the droplet radius. Figure 11.1 illustrates the doping process strategy used in different simulations.

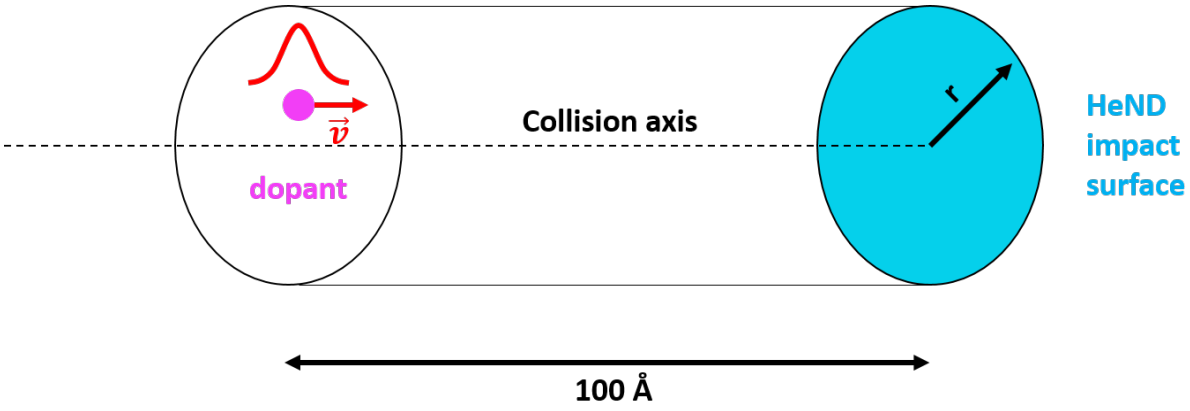

Figure 11.1: Scheme of doping process strategy. The dopant is randomly place inside the circle on the left and approaches the droplet with a random gaussian relative velocity

The generated normal random number computes the orthogonal velocity component of the dopant according to the Maxwell-Boltzmann distribution of speed which is a Gaussian-like function. The mean value of this distribution is the experimental velocity v_{agreg} of HeND ($\approx 500\,\mathrm{m/s}$) and the standard deviation is $\sigma = \sqrt{k_B \mathrm{T}/m}$ where T is the temperature, k_B the Boltzmann constant and m the dopant mass. The computation of the new dopant velocity is given by:

$$v = g\frac{k_B \mathrm{T}}{m} - \langle v_{agreg} \rangle \tag{11.1}$$

Where g represents the normal random number, $\sigma = \sqrt{k_B \mathrm{T}/m}$ the standard deviation and $\langle v_{agreg} \rangle$ the average velocity of the dopant in the experiments. The addition or subtraction of $\langle v_{agreg} \rangle$ depends on the initial positions of the dopant and the droplet. This has to be set to ensure a collision. This procedure has been used for the two kinds of numerical doping experiments done in this work. The first is the single impact and the second is the multiple impact to study the formation of structures seen in experiments as multiple aggregation and nanowires. Both processes have been automatised for multiple repetitions of equivalent events to ensure good statistics (Appendices E.7 and E.8). The process before the simulations of the single and multiple impact prepares the dopant as explained previously. The velocity of the dopant is randomly picked at a temperature T = 298 K and $\langle v_{agreg} \rangle = 480\,\mathrm{m/s}$.

For the single impact, only one phase of simulation is included in the automation. For each dopant and each HeND size, the process is realised in 20 chains of 50 repetitions. The simulation is configured with a number of time step equal to 15,000 with a time step of 10 fs which represents a physical time of 150 ps. Then, several specifically developed programs gather the data for calculating the average penetration depth, the angular and linear momentum transmission and the doping rate as well as the velocity of the evaporated atoms from the generated configuration file (section 4.6). Thus, another simulation is launched with another dopant velocity and dopant position on the impact surface on the same pure nanodroplet. In practice, this is done by adding a dopant atom with properly chosen initial positions and velocities to a pure droplet configuration by a program written during the thesis (Appendix E.6).

For the multiple impact, which studies the aggregation of xenon inside the HeND, the protocol requires more simulation phases. The first phase is an equilibration of the HeND with a number of time steps equal to 10,000 with a time step of 10 fs at constant energy where the linear and angular momenta are set to zero (L=0; P=0). The second phase parameterises firstly the dopant velocity and the position on the impact surface of the HeND and secondly the simulation of the dopant impact is done with 15,000 time steps of 10 fs at constant energy. After that an ensemble of specifically written codes analyse evaporated He atoms, track the main doped cluster and collect the needed data from the configuration files. Because we reuse the same nanodroplet for the multiple doping, there is evaporation of helium atoms and to properly

impact the main cluster the CCA (Appendix E.3) is used to identify the atoms belonging to the remaining droplet and to ensure the repeatability of the mechanics. Finally, a last computation is done to re-equilibrate the previously doped droplet to reset the momenta to zero with a Berendsen thermostat [64] at 0.37 K for 10,000 time steps of 10 fs with the adapted potentials at the working temperature (Appendix A). This last equilibration is needed because we assume a complete relaxation of HeND during experiments. Indeed, a HeND undergoes collisions at intervals on a time scale of several microseconds, which is out of range of our MD calculations. This means that the droplet has enough time to relax by evaporative cooling. In the simulation, we use a thermostat to rapidly bring the HeND back to the equilibrium temperature. Then, the process of three simulation phases is repeated n times for n impacts. For this work a HeND with 9000 atoms has been chosen for 20 impacts of xenon. The total physical time simulated by the automation is 7 ns. All the simulations were integrated with the Velocity Verlet algorithm [61].

11.3 Results and discussion

11.3.1 Average Penetration Depth

The simulation of the impact of rare gas dopant as argon, krypton and xenon on HeND shows three steps before the immersion in the nanodroplet. The first phase is the flight of the dopant towards the cluster. As seen in the Figure 11.2, which plot the evolution of the kinetic energy of a xenon atom for doping a nanodroplet containing 9000 helium atoms, the kinetic energy is constant until a certain point. The point is where the kinetic energy increases due to the attractive pair interactions with the helium atoms [143]. Then, the phase is followed by a decrease of the energy and as consequence on the velocity of the xenon due to dissipation. In fact, there is a translational relaxation of the xenon dopant which follows an exponential decay. During the energy decreasing the dopant undergoes collisions with the atoms of the bath until equilibration of the system by evaporation of solvent atoms. By applying the equipartition theorem for translational motion, the final temperature of the xenon is about 1 K.

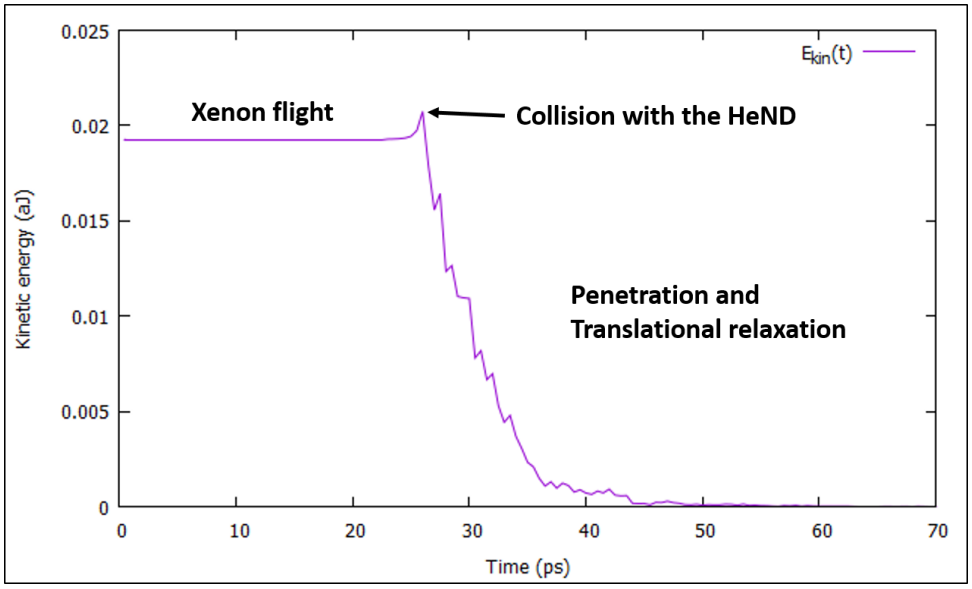

Figure 11.2: Evolution of the xenon kinetic energy during an impact on HeND with 9000 atoms

The main scheme of the dopant behaviour has been described and an important point is to know if the dopant comes to rest in the center of the droplet or not. The previous study on photodissociation has shown that the dopant, initially put in the center of the droplet, diffuses away from the center. The mechanism of impact with atoms of rare gas on different HeND size does not change this fact. Figure 11.3 shows the distance covered by the dopant as a straight line from the impact point to the end of the simulation in the helium cluster for argon, krypton and xenon. The main observation is that the heavier the dopant is, the more it travels in the droplet. The distance does not vary a lot with the size of the nanodroplets.

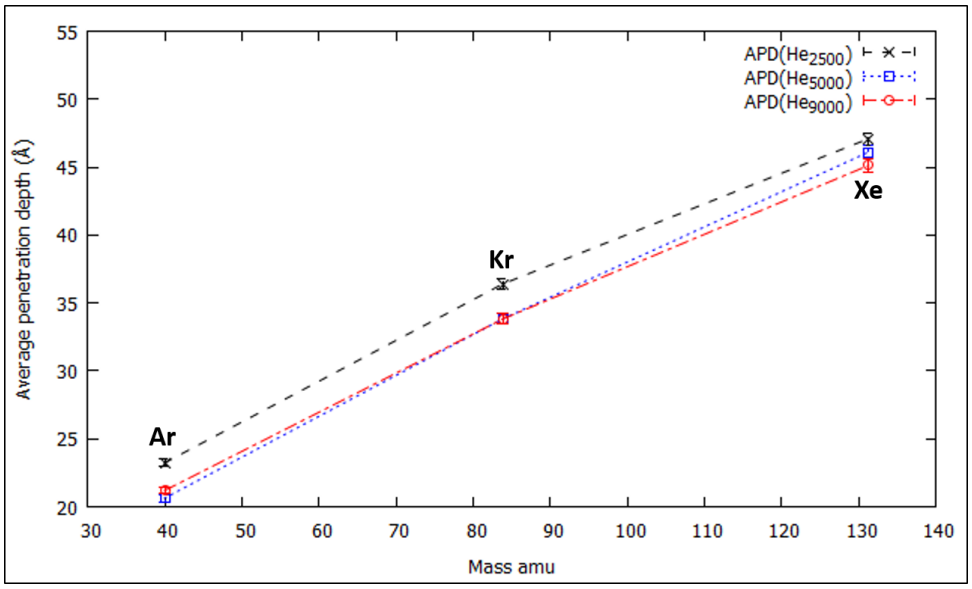

Figure 11.3: Average penetration depth of dopants in different HeND sizes

HeND size (n_{He})	**2500**	**5000**	**9000**
d[Argon] (Å)	23.23 ± 0.29	20.63 ± 0.27	21.19 ± 0.26
d[Krypton] (Å)	36.39 ± 0.40	33.82 ± 0.40	33.81 ± 0.39
d[Xenon] (Å)	47.09 ± 0.43	46.11 ± 0.47	45.12 ± 0.48

Table 11.1: Average penetration depth for rare gas dopants

By comparing the previous data with the following Figure 11.4, which shows the radial distribution of helium atoms in droplets of different sizes, the dopants, on the time scale of the simulations, travel about half of the radius of the droplets. Table 11.1 resumes the computed results where the mean standard deviation represents the error. There is clearly a preference of the dopant for the region about the center of the droplet for all droplet sizes.

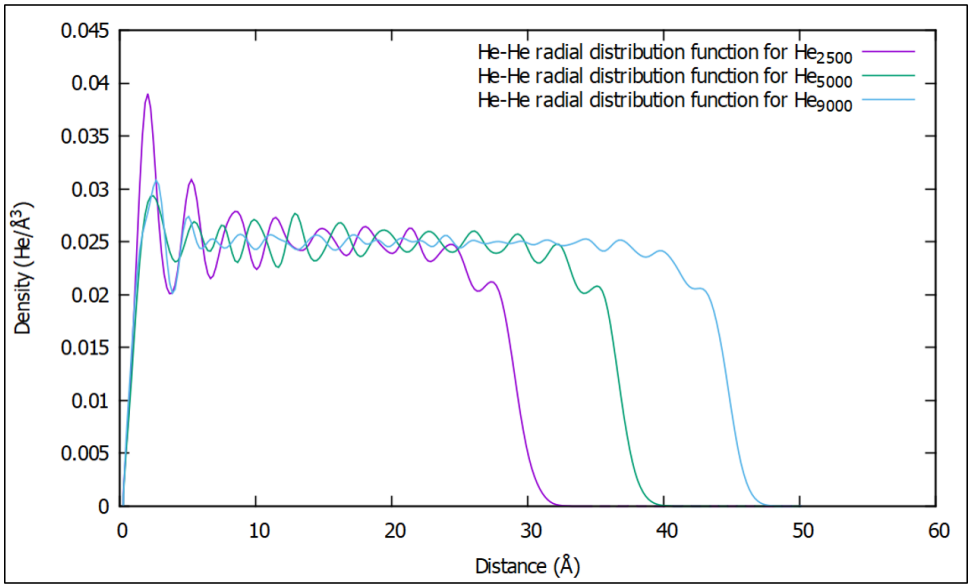

Figure 11.4: Radial distribution of helium atoms in pure droplets of different sizes before impact

11.3.2 HeND doping rate

The simulation counts the number of dopant atoms retained by the HeND as a function of the number of impacts. In fact, certain dopants can go through the nanodroplets especially those which make an impact on the borders of the cluster. The radial distribution functions in Figure 11.4 illustrate that the density of helium decreases near the edges and the retention probability of the dopant is weak compared to an impact on the center of the droplet in particular if the velocity of the incoming object is high. Figure 11.5 shows the doping rate of the three chosen dopants (Ar, Kr and Xe) for different HeND sizes. Table 11.2 summarises the data collected from the work on the doping rate. The errors are determined from the mean standard deviation

of the data sets. The first observation is that the doping rate increases with the size of the nanodroplet especially for krypton and xenon. The case of argon remains almost identical for each droplet size. The numerical results obtained here are comparable to experimental ones [33]. In fact, they measured the capture cross section, similar to the doping rate here, for droplet having an average size of 2500 atoms. They found for argon 94 %, for krypton 74 % and for xenon 58 % of capturing. These results are qualitatively close to the numerical ones computed in this work with the MD with adjusted quantum effective potential.

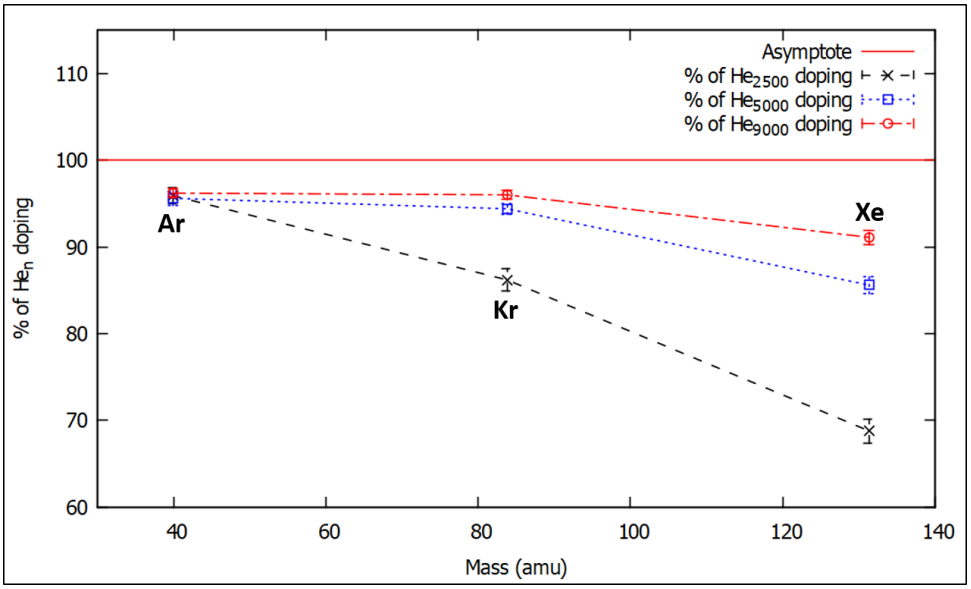

Figure 11.5: Doping rate for rare gas dopants and different HeND sizes

HeND size (n_{He})	**2500**	**5000**	**9000**
% [Argon]	95.9 ± 0.9	95.6 ± 0.8	96.2 ± 0.5
% [Krypton]	86.2 ± 1.3	94.4 ± 0.6	96.0 ± 0.5
% [Xenon]	68.8 ± 1.4	85.6 ± 1.0	91.1 ± 0.8

Table 11.2: HeND doping rate for argon, krypton and xenon

The explanation of that phenomenon resides in the fact that for the same kinetic energy, the momentum p and the mass of the dopant increase because the kinetic energy is conserved and has to be equal to $(3/2)k_B$T. Moreover, the number of atoms in capacity to make collisions to equilibrate the system after an impact is an important criterion for energy transfer. The more there are atoms in the droplet the more there are collisions the more the relaxation is efficient. As shown in Figure 11.6, which plots the number of evaporated helium atoms, smaller the droplet is the more there is evaporation. A relation can be done with the number of evaporated atoms and the kinetic energy they transport (subsection 11.3.3). Table 11.3 resumes the

collected data from the simulations with an error based on the mean standard deviation.

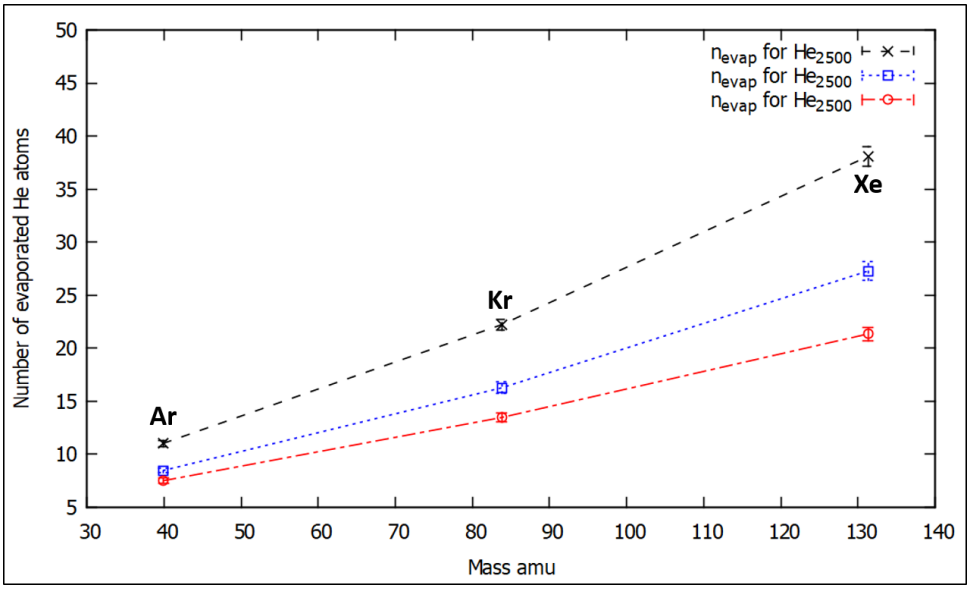

Figure 11.6: Number of evaporated helium atoms for different dopants and HeND sizes

HeND size (n_{He})	**2500**	**5000**	**9000**
nHe$_{evap}$ [Argon]	11.025 ± 0.30145	8.461 ± 0.22583	7.501 ± 0.25889
nHe$_{evap}$ [Krypton]	22.213 ± 0.48465	16.254 ± 0.53839	13.461 ± 0.39487
nHe$_{evap}$ [Xenon]	38.092 ± 0.91904	27.274 ± 0.84753	21.341 ± 0.64140

Table 11.3: Number of evaporated helium atoms for argon, krypton and xenon impact

The helium atoms in the cluster constitute a reservoir able to dissipate the excess energy. This dissipation of the excess energy of the dopant is materialised by the evaporation of helium atoms from the nanodroplet. The evaporated atoms have a certain amount of kinetic energy which can be numerically computed in order to construct their energy distribution. If the Boltzmann distribution is followed, which would mean that a quasi-equilibrium is reached, then a temperature can be deduced.

11.3.3 Kinetic energy distributions of evaporated atoms for argon, krypton and xenon impacts on HeND

The kinetic energy distribution of evaporated helium atoms following the impact of rare gas atoms have been computed. For each size and dopant a distribution has been binned into histograms. Statistics are made over the 20 chains of 50 repetitions giving sampling containing between 20,000 and 30,000 events. The idea is to test its compatibility with a Boltzmann

distribution and, in case of agreement to determine an effective temperature. For all distribution an exponential fit has been applied with a Boltzmann distribution-like function.

$$f(x) = a\exp(-\beta x) \tag{11.2}$$

Where a is the exponential pre-factor and β the coefficient in the Boltzmann distribution which is equal to $1/(k_B\mathrm{T})$. Then, the temperature of relaxation of the evaporated atoms can be deduced. The results are in cm^{-1} so Boltzmann constant is equivalent to $0.695\,\mathrm{cm}^{-1}/\mathrm{K}$. According to the exponential fit, the results obtained for the impact of argon (Figure 11.7 on p.126) give a temperature for the evaporated helium atoms of about 7.6, 8.9 and 9.9 K respectively for the droplet size of 2500, 5000 and 9000 helium atoms. For the impact of the krypton (Figure 11.8 on p.127), 7.0, 7.8 and 8.7 K, respectively, for the droplet sizes of 2500, 5000 and 9000 helium atoms. The range of temperature for xenon impacting the HeND is 6.7, 6.9 and 8.3 K, respectively, for 2500, 5000 and 9000 droplet size (Figure 11.9 on p.128). Globally, the range of the kinetic temperatures is between 6 K and 9 K which means that the atoms leave the droplets with an important energy relative to the droplet and the process of evaporative cooling is efficient but incomplete regarding the previous data on the doping rate.

According to Figures 11.7-11.9, more the HeND contains atoms more the mean kinetic energy of the distributions increases. But the relation is not trivial considering the relaxation is not completed over the time scale simulations. In fact on each subfigure a second graph shows the same distribution in log scale. We clearly see that the exponential fit unveils that higher energies are overrepresented which means that the relaxation is not totally done. However, at low energies the exponential fit is acceptable for relaxed atoms. There are several regimes present where the atoms are relaxed, in transition or still non-thermalised.

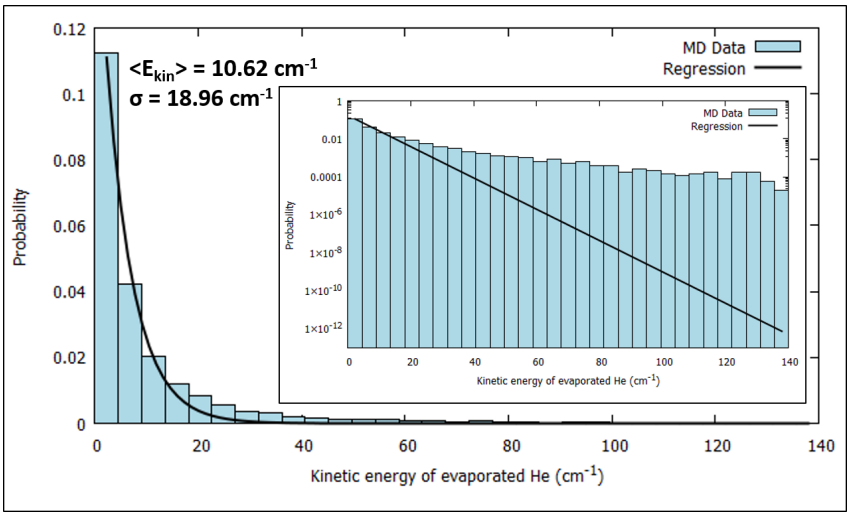

(a) Kinetic energy distribution of He atoms evaporated for argon impacting HeND 2500

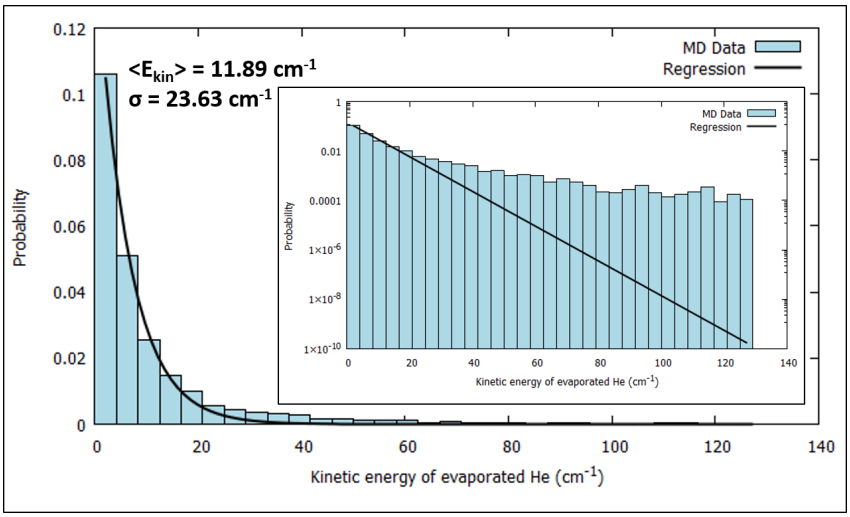

(b) Kinetic energy distribution of He atoms evaporated for argon impacting HeND 5000

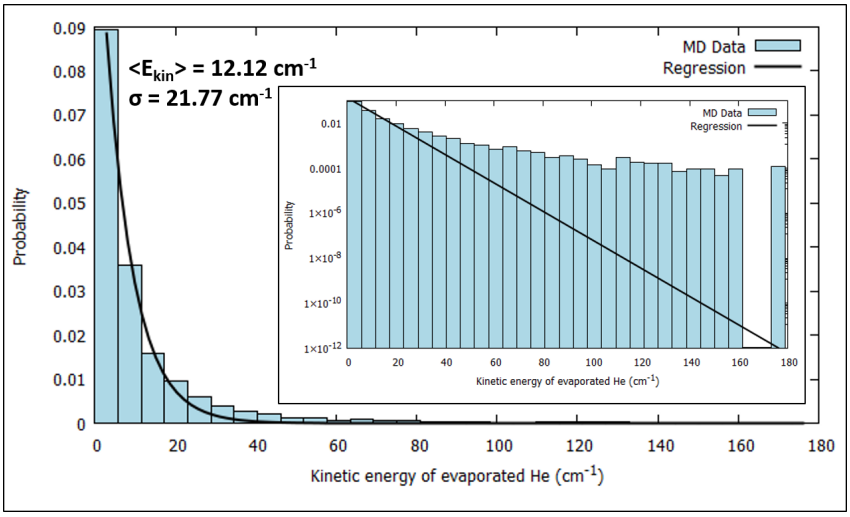

(c) Kinetic energy distribution of He atoms evaporated for argon impacting HeND 9000

Figure 11.7: Kinetic energy distribution of He atoms evaporated for argon impacting HeND. The small graph represents the same data plot in log scale

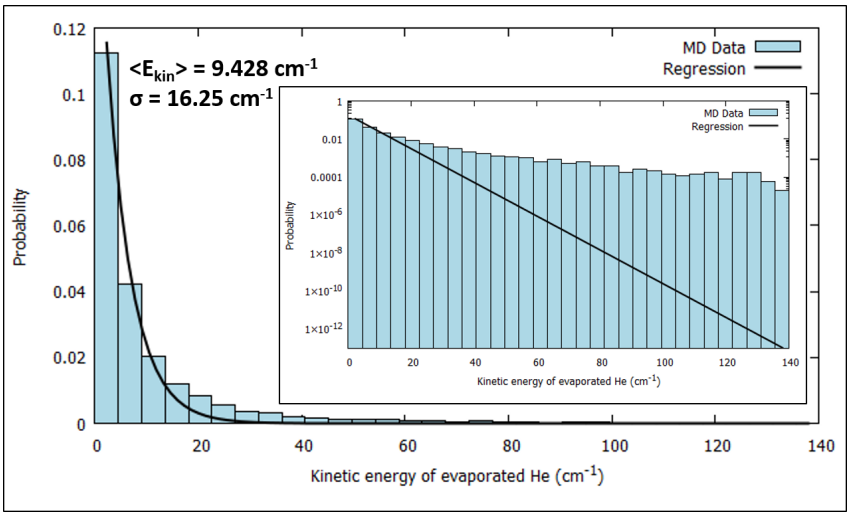

(a) Kinetic energy distribution of He atoms evaporated for krypton impacting HeND 2500

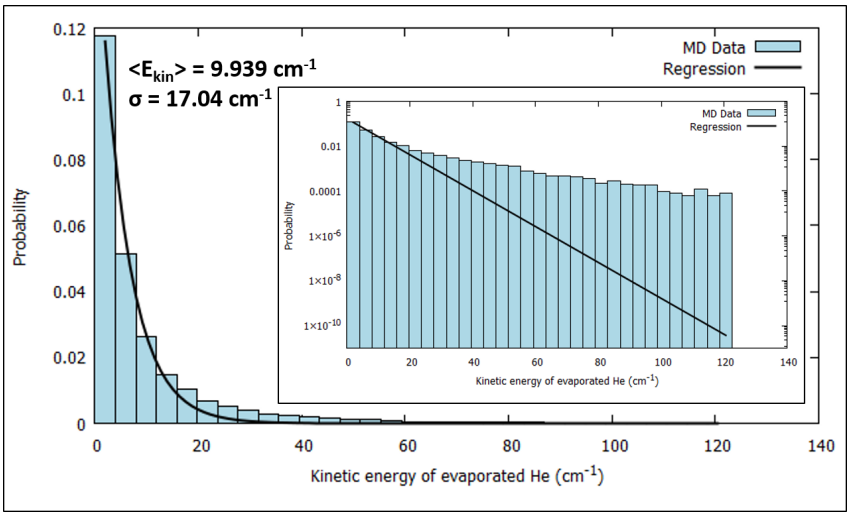

(b) Kinetic energy distribution of He atoms evaporated for krypton impacting HeND 5000

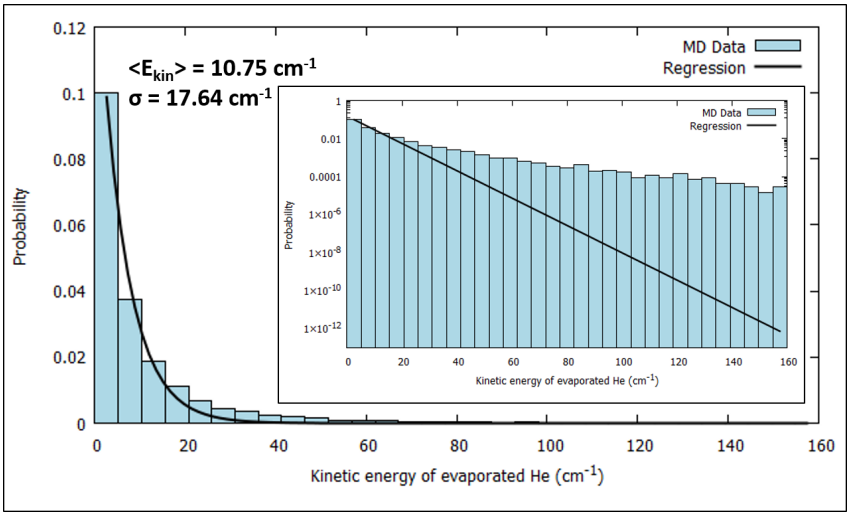

(c) Kinetic energy distribution of He atoms evaporated for krypton impacting HeND 9000

Figure 11.8: Kinetic energy distribution of He atoms evaporated for krypton impacting HeND. The small graph represents the same data plot in log scale

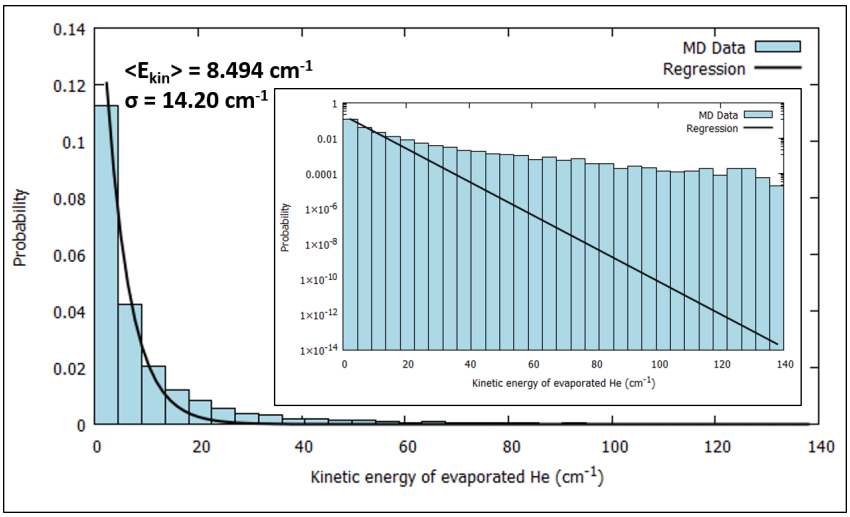

(a) Kinetic energy distribution of He atoms evaporated for xenon impacting HeND 2500

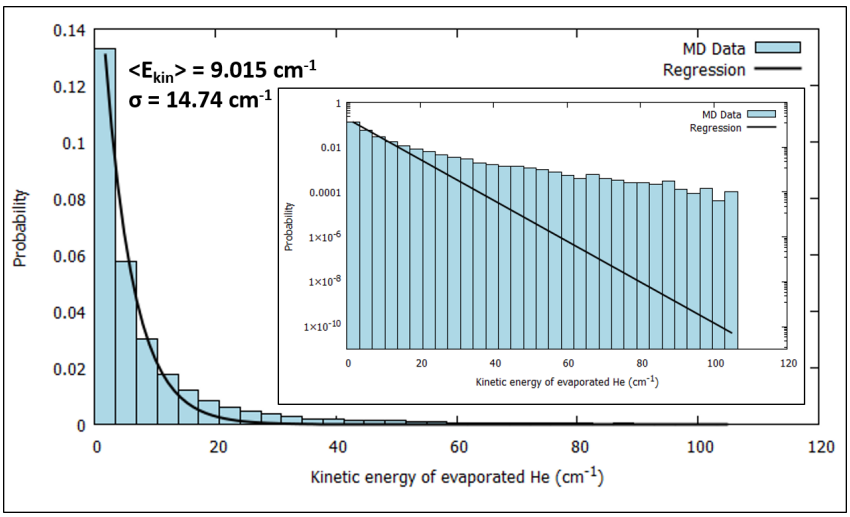

(b) Kinetic energy distribution of He atoms evaporated for xenon impacting HeND 5000

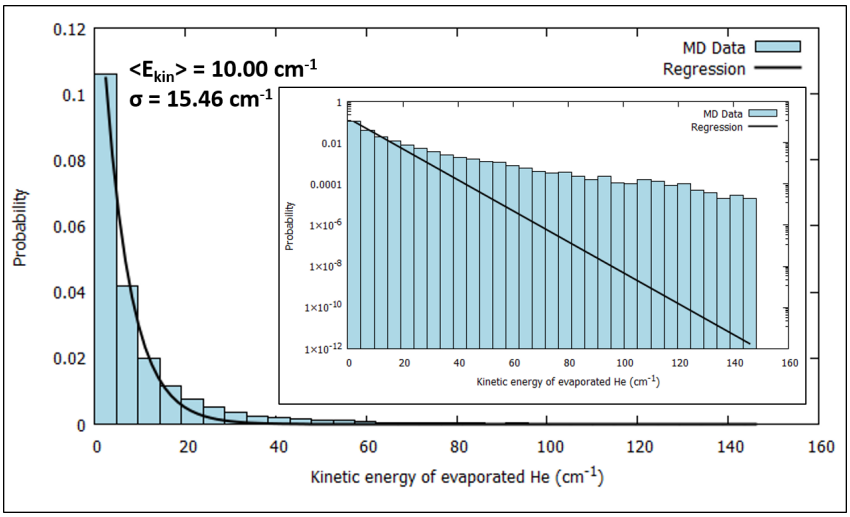

(c) Kinetic energy distribution of He atoms evaporated for xenon impacting HeND 9000

Figure 11.9: Kinetic energy distribution of He atoms evaporated for xenon impacting HeND. The small graph represents the same data plot in log scale

11.3.4 Linear and rotational momenta transmission

After the average penetration depth, the transmission of the linear and rotational momenta of the dopants are studied. In the simulations performed of this work, the only objects initially having this kind of momenta are the dopants. This statistics is calculated by the following expression:

$$\begin{aligned} \%\mathrm{P}_{\text{transmitted}} &= \frac{\mathrm{P}_{\mathrm{t}}^{\text{doped system}} - \mathrm{P}_{\text{initial}}^{\text{system}}}{\mathrm{P}_{\text{initial}}^{\text{dopant}}} \\ \%\mathrm{L}_{\text{transmitted}} &= \frac{\mathrm{L}_{\mathrm{t}}^{\text{doped system}} - \mathrm{L}_{\text{initial}}^{\text{system}}}{\mathrm{L}_{\text{initial}}^{\text{dopant}}} \end{aligned} \tag{11.3}$$

To achieve this analysis, the CCA is used to find after the impact of the main structure containing the dopant. In fact, only the doped system is taken into account in the calculation. Then, we obtain the following results for the linear momentum transmission shown in Figure 11.10. The first observation is that the transmission of the linear momentum is more efficient for large droplets. Likewise, the fraction of transmission is higher when the dopant atom is small. In fact, for all HeND size argon better transmits the momentum than krypton and xenon atoms. Between the two heavier atoms there is no flagrant distinction according to the mean standard deviation. Another remark is the fact that the linear momentum transmission is not equal to one. In fact when the droplets are doped the excess of translational motion of the dopant is amortised by the evaporation of helium atoms which takes away a part of the total momentum. For the bigger size of HeND the ratio is very high because there are more helium atoms able to play a role in the relaxation process so that the evaporated fraction which have momenta is less important than for other HeND sizes. The results of the linear momentum transmission are collected in Table 11.4 where the mean standard deviations represent the error.

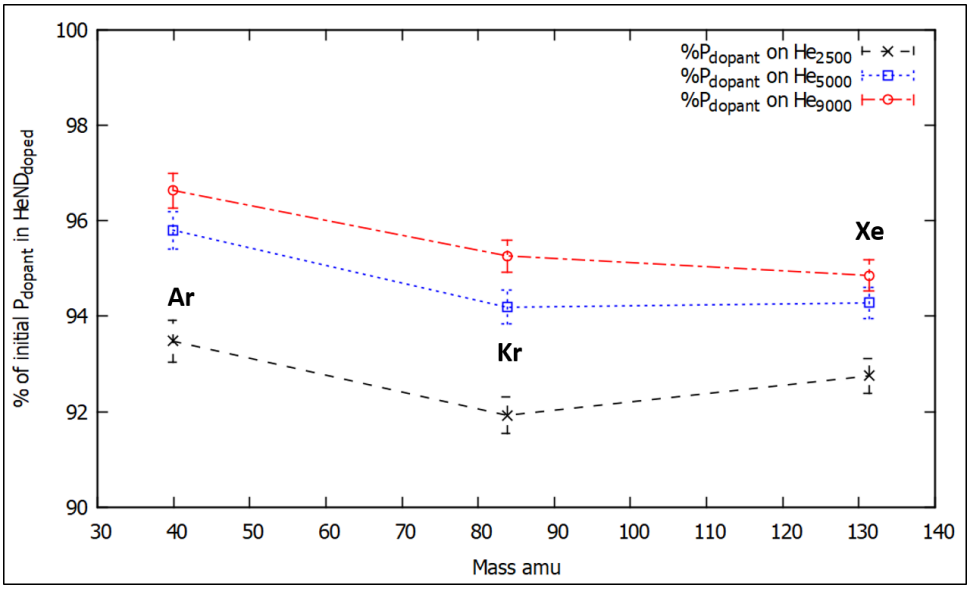

Figure 11.10: Linear momentum transmission of dopants to different HeND sizes

HeND size (n_{He})	**2500**	**5000**	**9000**
% P[Argon]	93.5 ± 0.40	95.8 ± 0.40	96.6 ± 0.36
% P[Krypton]	91.9 ± 0.38	94.2 ± 0.36	95.27 ± 0.34
% P[Xenon]	92.8 ± 0.37	94.3 ± 0.33	94.9 ± 0.33

Table 11.4: Linear momentum transmission from rare gas dopants to HeND

The same methods of tracking as for the linear momentum transmission has been used for the angular momentum. The first observation is that the fraction that the dopant transmits to the droplet is less efficient than the linear momentum. In fact, the angular momentum transmission depends strongly on where the impact is done on the surface of the droplet. If the contact takes place on the center, there is no rotation induced on the droplets. More the impact is away from the center more the droplet tends to rotate. The first observation is that the heavier the rare gas dopant is, the more it generates a rotational motion to the droplet impacted [144]. The second one is that the more there are atoms in the droplet the more the transfer of rotational motion is pronounced. This phenomenon can be explained by the fact that the dopants capture is more efficient with large nanodroplets despite the fact that rare gas dopants are able to occasionally go through the nanoliquid. To finish the angular momentum transmission is not complete as assumed in experiment [33] but it was nice approximation. This has consequences on HeND deflection which is a technique to quantify the number of helium atoms in droplet.

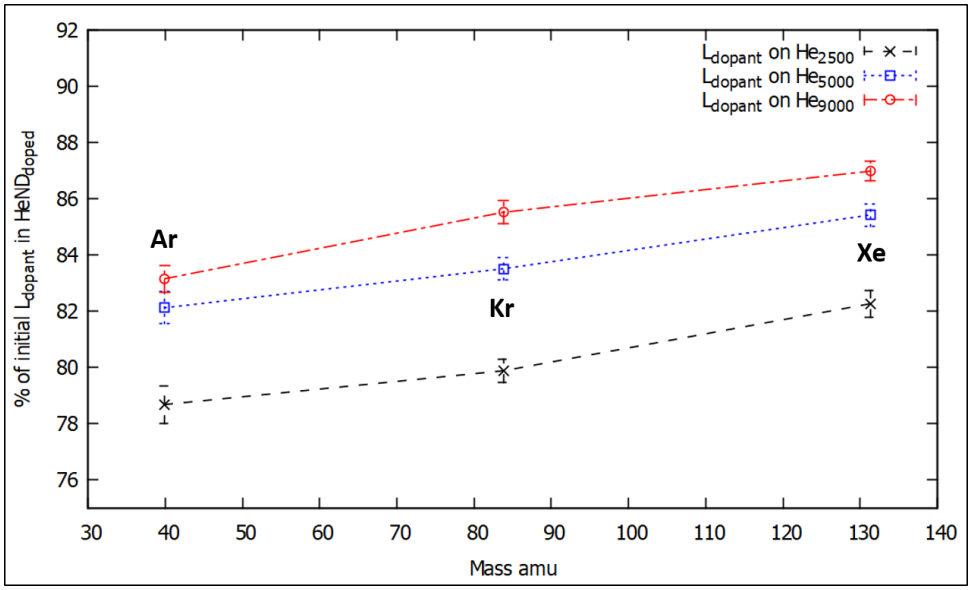

Figure 11.11: Angular momentum transmission of dopants to different HeND sizes

Table 11.5 collects the data obtained from the simulation of the angular momentum transmission to the nanodroplet. The errors are calculated with the mean standard deviation of the data set.

HeND size (n_{He})	**2500**	**5000**	**9000**
% L[Argon]	78.7 ± 0.67	82.1 ± 0.6	83.2 ± 0.48
% L[Krypton]	79.9 ± 0.42	83.5 ± 0.40	85.5 ± 0.41
% L[Xenon]	82.3 ± 0.48	85.4 ± 0.39	87.0 ± 0.34

Table 11.5: Angular momentum transmission from rare gas dopants to HeND

11.3.5 Aggregation inside HeND

This part of the work is about the multiple doping of a HeND containing 9000 atoms by twenty xenon atoms but first a simulation on HeND 5000 will be presented. The same approach as for single doping is used to generate the initial random positions and velocities. After several processes of doping when there are two dopants in the droplet of 5000 helium atoms, a recombination between them can occur on a time scale of several picoseconds as shown in Figure 11.12 which represents the distance between the two xenon atoms as a function of time. In this example, the recombination takes approximatively 100 ps. This is the secondary recombination of the xenon dimer as described by Noyes [120, 121] and late by Murrell and *et al.* [101]. Before achieving the recombination, there is a phase called the snowball or well-known as the Atkins' snowball [142], a structure where helium atoms surrounding the interacting dopant adopt an

ordered arrangement like crystal. This special arrangement is due to the strong He-dopant interaction. MD simulations in this work only deal with the neutral atoms. The presence of this structure can be explained by the analysis of the Lennard-Jones potential used to simulate the He-He, He-Xe and Xe-Xe pair interactions (Appendix A). Indeed, the He-Xe interaction is stronger than the He-He interaction so that during the diffusion of the xenon atoms they carry a shell of helium atoms (Figure 8.4). According to Figure 11.12 there are several phases before xenon recombination. Between 0 and 15 ps we observe the diffusion of xenon atoms through HeND. At 20 ps a plateau phase is shown which ends at around 40 ps. It is during this step that the snowball effect occurs. After 45 ps of simulation a collapse appears meaning that the xenon recombination occured and the dimer vibrates. This behaviour is indicated by the oscillation around the equilibrium distance value of 4.363 Å after 50 ps.

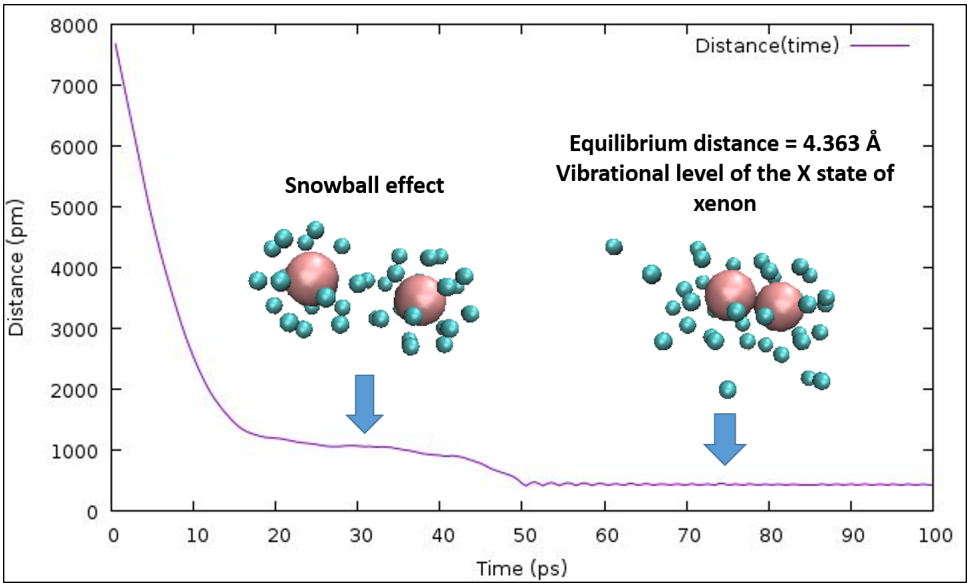

Figure 11.12: Time evolution of distance between xenon atoms after double doping trajectory in HeND 5000

Figure 11.13 shows selected outcomes which correspond to the multiple impact of xenon dopants on the liquid medium actually in the HeND containing 9000 atoms. After twenty successive collisions the droplets is multiply doped and different structures of aggregation are shown in the second section in Figure 11.13 like dimers, trimers, crystalline forms and chains of xenon in different sites of nucleation within the nanodroplets which could be analysed by soft-landing techniques for more robust species [39, 134, 145]. In this thesis, we did not evaluate the proportion of the observed structures.

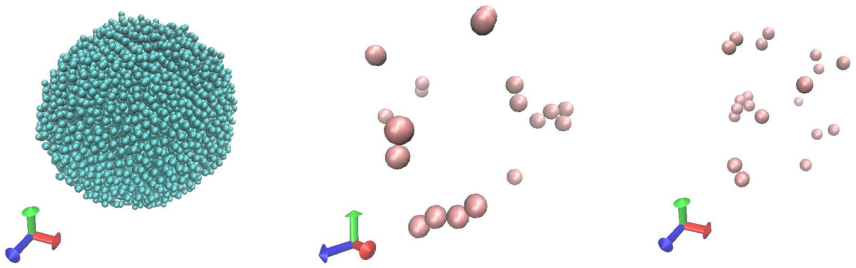

Figure 11.13: Scheme of xenon aggregation in HeND

The presence of chains of xenon can be explained by the fact that it could be a long living form before the aggregation which could happen in a long time scale which is now out of MD. In fact, the energy excess transmitted by the multiple doping is dissipated by an efficient evaporative cooling which preserves these structures. The kinetic energy of the evaporated helium atoms roughly follows a Boltzmann distribution plotted in Figure 11.14 for 364 events where the relaxation temperature is equal to 8.71 K according to the exponential fit of eq. (11.2). We observe like for single impact some non-thermal events and different regimes of relaxation.

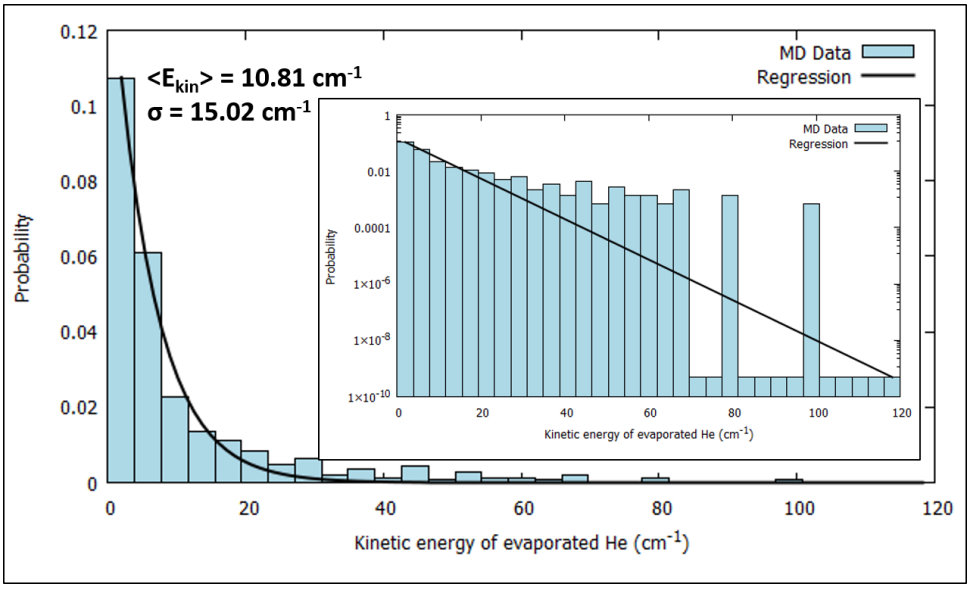

Figure 11.14: Kinetic energy distribution of He atom evaporated for 20 xenon impacts on HeND 9000

11.3.6 Conclusion

The main observations of this work on HeND doping with rare gas atom (Ar, Kr, and Xe) is that the average penetration depth strongly depends on the mass of the dopant and the dissipation of translational energy occurs within a few picoseconds. Moreover, pickup probabilities

are in good agreement with 1995 experiments [33]. For transmission of linear and rotational momentum to the nanodroplet, this phenomenon is important when the doping rate is high for the largest HeND. Calculations reveal that droplets are deflected less than they would with full momentum transfer and they appear a little larger than they actually are in 1995 experiments. Starting from the latter statistics on evaporation, kinetic distributions for each dopant have been computed and are largely consistent with Boltzmann statistics but with additional high energy contributions indicating that some helium atoms leave the cluster with high velocity.

The dynamics of aggregation in nanodroplets shows some special helium-dopant configurations where the metastable structure of snowball appears. Structures like nanocrystals, nanowires are identified in several places in HeND. The evaporative cooling and the strong helium-dopant interaction stabilise these structures at low temperature. It is evident that multiple dopants aggregate around several nucleation sites and do not form a simple dopant aggregate on a short time scale. More complete aggregation could occur on time scale beyond the reach of our atomistic simulations.

The MD with quantum effective potential has succeeded in numerically modelling these phenomena and interaction helium-dopant observed by experimentalist in doping HeND despite the fact that not all quantum effects like superfluidity (quantum vortices) are included in the model.

Part IV

Conclusion and outlook

Chapter 12

General conclusion and outlook

During this PhD. thesis the objective was to propose a new computational method for simulating phenomena of aggregation and dissociation in HeND by an approximate many body dynamics and additional tools to define specific initial conditions, to collect statistics of the dynamic events, automatise the launching and analysis of multiple dynamics. These simulations are based on the quantum effective potential idea where the quantum approximation is the delocalisation of helium atoms at temperatures close to absolute zero. Indeed, the delocalisation at 0.5 K is about 6 Å which is in the same range as the typical distances in liquid helium clusters (4 Å). Liquid helium is classified as a quantum liquid and should be treated by quantum methods but there is no fully quantum computation method able to compute large helium clusters. This justifies the present approach by the special MD allowing the observation of static and dynamic properties of the nanodroplets like density, energy relaxation, temperature and evaporation rate. The CLUSTER code is very efficient due to vectorisation so that the computational cost is modest and it allows calculations of multiple trajectories with HeND of thousands of atoms compared to QMC,DFT and PIMD [146].

To perform the study of the dynamics of dissociation in HeND, molecular iodine has been chosen because it is a well-studied chemical species by experimentalists in gas phase and non-conventional matrices at high energy [147] and in Graz University in the I_2 B state. In this part of the study, low energy photodissociation has been studied which leads to neutral fragments. This procedure has been done by a code modifying the initial iodine atom velocities. The excitation is half of the experimental one used on analogous system (CH_3I and CF_3I) [42–44] but the results are comparable concerning the distribution of photofragment velocities and sizes. An important data is the fast non-exponential energy dissipation done by the droplet within a few picoseconds. This process is mainly due to evaporative cooling and photofragment ejection which can be experimentally analysed by TOF-MS. Another observation is the diffusion behaviour of the diatomic dopant in the HeND which visits a large part of the nanoliquid before the photodissociation. Vibrational and rotational excitations have been performed

on the same diatomic molecule at energies below the fragmentation limit of 1.55 eV. It appears that rotational energy dissipation occurs on a picosecond time scale for the type of excitation done. Likewise a vibrational excitation shows absence of visible relaxation on the time scale accessible to direct simulation of the molecular iodine in helium cluster as for HF molecule [125].

In experiments, it has been shown that HeND were not spherical but geoids. An algorithm to give a well defined angular momentum to the droplet by modifying the velocities of helium atoms in the droplet has been developed and integrated into the CLUSTER code so that the rotation can be done on a chosen axis. With this strategy, the exploration of the patterns of single and multiple splitting has been studied and unveiled that the nanoclusters evolve according to a given angular momentum from oblate to prolate shape and in the extreme case to annular splitting. To easily analyse these events the asymmetry parameter has been computed for several angular momenta. The study reveals that the chosen angular momenta were close to the experiments [47]. This research topic has been an opportunity to develop an algorithm based on graph theory which is called complete clustering algorithm (CCA) where its computational complexity is strictly proportional to the number of objects treated. This has been used to quantify the number of subclusters created by this kind of fragmentation.

For the aggregation part of this thesis, doping and aggregation of rare gas atom dopant have been computed. To achieve that some development of uniform and random number codes have been done in order to randomly choose an impact point on the surface of the HeND and a random velocity according to a Maxwell-Boltzmann distribution. From this protocol the multiple single impact on the droplets give as outcomes the average penetration depth, the doping rate, the linear and rotational momenta transmission dopant-HeND. For the linear momenta transmission dopant-HeND, the travelled distance depends on the mass of the dopant. For rotational momenta transmission dopant-HeND, the larger the droplet is, the more it has the capacity to retain the dopant. However the dopant can escape after travelling in the HeND. For the third and last case, the transmission of momenta depends on the doping rate and on the mass of the dopant. It has been shown in our calculations that the momenta transmission is not complete compared to experiment [33]. Indeed, the transmission is important for deflection of HeND to determine droplet size distribution. However, our numerical results about pickup are in good agreement with experiments. Small dopant is easily captured by a large cluster. In the case of a heavy dopant, the possibility of going through the droplet increases. Then, to determine the temperature of the evaporated atoms distributions have been constructed and give as results a range of temperatures from 6 K to 8 K. It has to be known that these distributions include evaporated atoms at low and high velocities.

For the multiple doping of HeND with xenon atoms some structures appear during the simulations like the Atkins' snowball, which is a metastable state where the helium atoms are

structured as crystals surrounding the interacting dopant. This is due to the strong interactions with dopants. Despite the lack of quantum vortices because the superfluidity is not included in the model, our computations have unveiled chains of xenon in the nucleation sites of the HeND as xenon nanocrystals, dimer and trimer. This aspect of aggregation has been observed in experiments with metallic atoms [39, 134, 145].

MD with quantum effective potential is a strong modelling method to describe almost all phenomena experimentally observed with a low computational cost. The next step of this semi-classical model is the description of dissociation in more highly excited states like the ion pair states examined in the work of von Vangerow [147]. Indeed they occur in photodissociation and it can be done by including electrostatic theory by using the Coulomb-Buckingham potential which is currently used to describe interactions with ions and van der Waals forces, particularly the dispersion, which dominates interactions of rare gas atoms. This will allow the simulations and the study of the interaction between large HeND and charged species like alkaline earth. The parallelisation of the CLUSTER code is another step which will permit the modelling of larger HeND.

Part V

Bibliography

Bibliography

[1] P. Kapitza, *Nature*, 1938, **141**, 74.

[2] J. F. Allen and A. D. Misener, *Nature*, 1938, **141**, 75.

[3] H. E. Hall and F. Vinen, *Proc. R. Soc. A*, 1956, **238**, 204–210.

[4] H. E. Hall and F. Vinen, *Proc. R. Soc. A*, 1956, **238**, 215–234.

[5] G. W. Rayfield and F. Reif, *Phys. Rev.*, 1964, **136**, A1194.

[6] H. Kamerlingh Onnes, *Commun. Phys. Lab. Unive. Leiden*, 1908, **105**, 744.

[7] E. W. Becker, R. Klingelhöfer, and P. Lohse, *Z. Naturforsch. A*, 1962, **17**, 432–438.

[8] J. Gspann and H. Vollmar, *Rarefied Gas Dynamics*, Academic Press, New York, 1974.

[9] J. Gspann, G. Krieg, and H. Vollmar, *J. Phys. Colloq.*, 1977, **38**, C2–171–C2–173.

[10] H. Buchenau, E. L. Knuth, J. Northby, J. P. Toennies, and C. Winkler, *J. Chem. Phys.*, 1990, **92**, 6875.

[11] F. Stienkemeier and K. K. Lehmann, *J. Phys. B*, 2006, **39**, R127–R166.

[12] F. Stienkemeier, M. Wewer, F. Meier, and H. O. Lutz, *Rev. Sci. Instrum.*, 2000, **71**(9), 3480–3484.

[13] F. Stienkemeier, O. Bünermann, R. Mayol, F. Ancilotto, M. Barranco, and M. Pi, *Phys. Rev. B*, 2004, **70**, 214509.

[14] M. Lewerenz, B. Schilling, and J. P. Toennies, *Chem. Phys. Lett.*, 1993, **206**, 381–387.

[15] L. Gomez, E. Loginov, R. Sliter, and A. Vilesov, *J. Chem. Phys.*, 2011, **135**, 154201.

[16] R. Tanyag, C. Jones, S. O'Connell, D. Verma, and A. Vilesov, *Experiments with large superfluid helium nano-droplets. Cold chemistry: Molecular scattering and reactivity near absolute zero*, Cambridge: The Royal Society of Chemistry, 2018.

[17] S. Albertini, E. Gruber, F. Zappa, S. Krasnokutski, F. Laimer, and P. Scheier, *Mass Spectrom. Rev.*, 2022, **41**(4), 529–567.

[18] M. Slipchenko, S. Kuma, T. Momose, and A. Vilesov, *Rev. Sci. Instrum.*, 2002, **73**, 3600.

[19] D. Verma and A. Vilesov, *Chem. Phys. Lett.*, 2018, **694**, 129–134.

[20] J. P. Toennies and A. F. Vilesov, *Angew. Chem. Int. Ed.*, 2004, **43**, 2622–2648.

[21] F. Stienkemeier, J. Higgins, W. Ernst, and G. Scoles, *Phys. Rev. Lett.*, 1995, **74**(18), 3592.

[22] J. Higgins, C. Callegari, J. Reho, F. Stienkemeier, W. Ernst, M. Gutowski, and G. Scoles, *J. Phys. Chem. A*, 1998, **102**(26), 4952–4965.

[23] L. An der Lan, P. Bartl, C. Leidlmair, H. Schöbel, R. Jochum, S. Denifl, T. D. Märk, A. M. Ellis, and P. Scheier, *J. Chem. Phys.*, 2011, **135**(4), 044309.

[24] A. Schiller, P. Martini, A. Maalouf, E. E. Jabbour, and P. Scheier, *Eur. Phys. J. D*, 2021, **75**(4), 1–8.

[25] T. E. Gough, M. Mengel, P. A. Rowntree, and G. Scoles, *J. Chem. Phys.*, 1985, **83**(10), 4958–4961.

[26] J. Gspann, *Physica B+ C*, 1981, **108**, 1309–1310.

[27] A. Scheidemann, B. Schilling, J. P. Toennies, and J. Northby, *Physica B*, 1990, **165-166**, 135–136.

[28] J. Gspann, *Z. Phys. B*, 1995, **98**, 405–411.

[29] J. H. Reho, U. Merker, M. R. Radcliff, K. K. Lehmann, and G. Scoles, *J. Phys. Chem. A*, 2000, **104**(16), 3620–3626.

[30] J. Küpper, J. Merritt, and R. Miller, *J. Chem. Phys.*, 2002, **117**, 647–652.

[31] P. Claas, S.-O. Mende, and F. Stienkemeier, *Rev. Sci. Instrum.*, 2003, **74**, 4071.

[32] A. Lindinger, J. Toennies, and A. Vilesov, *J. Chem. Phys.*, 1999, **110**, 1429.

[33] M. Lewerenz, B. Schilling, and J. P. Toennies, *J. Chem. Phys.*, 1995, **102**, 8191.

[34] H. Odaka and M. Ichihashi, *Eur. Phys. J. D*, 2017, **71**, 1–6.

[35] M. Hartmann, R. Miller, J. Toennies, and A. Vilesov, *Phys. Rev. Lett.*, 1995, **75**, 1566–1569.

[36] S. Grebenev, J. Toennies, and A. Vilesov, *Science*, 1998, **279**, 2083–2086.

[37] F. Bierau, P. Kupser, G. Meijer, and G. von Helden, *Phys. Rev. Lett.*, 2010, **105**, 133402.

[38] M. Alghamdi, J. Zhang, A. Oswalt, R. Porter, J. Mehl, and W. Kong, *J. Phys. Chem. A*, 2017, **121**, 6671–6678.

[39] L. F. Gomez, E. Loginov, and A. F. Vilesov, *Phys. Rev. Lett.*, 2012, **108**(15), 155302.

[40] R. S. Mulliken, *J. Chem. Phys.*, 1971, **55**, 288–308.

[41] J. Franck and E. Rabinowitch, *Trans. Faraday Soc.*, 1934, **30**, 1381–1387.

[42] A. Braun and M. Drabbels, *J. Chem. Phys.*, 2007, **127**, 114303.

[43] A. Braun and M. Drabbels, *J. Chem. Phys.*, 2007, **127**, 114304.

[44] A. Braun and M. Drabbels, *J. Chem. Phys.*, 2007, **127**, 114305.

[45] L. F. Gomez, K. R. Ferguson, J. P. Cryan, C. Bacellar, R. M. P. Tanyag, C. Jones, S. Schorb, D. Anielski, A. Belkacem, C. Bernando, et al., *Science*, 2014, **345**(6199), 906–909.

[46] C. Bernando, R. M. P. Tanyag, C. Jones, C. Bacellar, M. Bucher, K. R. Ferguson, D. Rupp, M. P. Ziemkiewicz, L. F. Gomez, A. S. Chatterley, et al., *Phys. Rev. B*, 2017, **95**(6), 064510.

[47] S. M. O'Connell, R. M. P. Tanyag, D. Verma, C. Bernando, W. Pang, C. Bacellar, C. A. Saladrigas, J. Mahl, B. W. Toulson, Y. Kumagai, et al., *Phys. Rev. Lett.*, 2020, **124**(21), 215301.

[48] K. B. Whaley, *Int. Rev. Phys. Chem.*, 1994, **13**(1), 41–84.

[49] P. Hohenberg and W. Kohn, *Phys. Rev.*, 1964, **136**(3B), B864.

[50] F. Ancilotto, M. Barranco, F. Coppens, J. Eloranta, N. Halberstadt, A. Hernando, D. Mateo, and M. Pi, *Int. Rev. Phys. Chem.*, 2017, **36**(4), 621–707.

[51] E. Runge and E. K. Gross, *Phys. Rev. Lett.*, 1984, **52**(12), 997.

[52] F. Dalfovo, A. Lastri, L. Pricaupenko, S. Stringari, and J. Treiner, *Phys. Rev. B*, 1995, **52**(2), 1193.

[53] M. Lewerenz, Quantum Monte Carlo - Lecture notes, 2013.

[54] P. Slavíček, P. Jungwirth, M. Lewerenz, N. H. Nahler, M. Fárník, and U. Buck, *J. Chem. Phys.*, 2003, **107**, 7743–7754.

[55] D. Bonhommeau, M. Lewerenz, and N. Halberstadt, *J. Chem. Phys.*, 2008, **128**(5), 054302.

[56] R. Panzou and M. Lewerenz, *Mol. Phys.*, 2021, **119**(17-18), e1977862.

[57] M. Allen and D. Tildesley, *Computer Simulation of Liquids*, Oxford University Press, 1987.

[58] C. E. Hecht, *Statistical thermodynamics and kinetic theory*, Freeman, 1990.

[59] D. Frenkel and B. Smit, *Understanding molecular simulation: from algorithms to applications*, Vol. 1, Academic Press, 1996.

[60] P. L. Houston, *Chemical kinetics and reaction dynamics*, Dover, 2006.

[61] L. Verlet, *Phys. Rev.*, 1967, **159**.

[62] R. W. Hockney, *Methods Comput. Phys.*, 1970, **9**, 136–211.

[63] W. C. Swope, H. C. Andersen, P. H. Berens, and K. R. Wilson, *J. Chem. Phys.*, 1982, **76**, 637.

[64] H. J. C. Berendsen, J. P. M. Postma, W. F. van Gunsteren, A. DiNola, and J. R. Haak, *J. Chem. Phys.*, 1984, **81**, 3684.

[65] H. C. Andersen, *J. Chem. Phys.*, 1980, **72**, 2384.

[66] M. Lewerenz, Modelisation multi echelle : Dynamique moleculaire - Lecture notes, 2015.

[67] J. Jellinek and D. Li, *Phys. Rev. Lett.*, 1989, **62**(3), 241.

[68] D. Li and J. Jellinek, *Z. Phys. D*, 1989, **12**(1), 177–180.

[69] H. Vach, *J. Chem. Phys.*, 1999, **111**(8), 3536–3547.

[70] J. E. Jones, *Proc. R. Soc. A*, 1924, **106**(738), 463–477.

[71] P. M. Morse, *Phys. Rev.*, 1929, **34**(1), 57.

[72] R. P. Feynman and A. R. Hibbs, *Quantum Mechanics and Path Integrals*, McGraw Hill, New York, 1965.

[73] R. P. Feynman, *Statistical Mechanics*, Addison Wesley, Reading, MA, 1972.

[74] L. M. Sesé, *Mol. Phys.*, 1993, **78**(5), 1167–1177.

[75] B. Guillot and Y. Guissani, *J. Chem. Phys.*, 1998, **108**(24), 10162–10174.

[76] M. Lewerenz personal communication, 2021.

[77] V. Syvokon, *Low Temp. Phys.*, 2006, **32**(1), 48–54.

[78] W. Humphrey, A. Dalke, and K. Schulten, *J. Mol. Graph.*, 1996, **14**(1), 33–38.

[79] F. G. Brickwedde, *J. Res. Natl. Bur. Stand. A Phys. Chem.*, 1960, **64**(1), 1.

[80] H. Van Dijk, M. Durieux, J. Clement, and J. Logan, *J. Res. Natl. Bur. Stand. A Phys. Chem.*, 1960, **64**(1), 1.

[81] G. Gamow, *Proc. R. Soc. A*, 1930, **126**(803), 632–644.

[82] W. H. Press, S. A. Teukolsky, W. T. Vetterling, and B. P. Flannery, *Numerical Recipes in Fortran : The art of scientific computing 2nd edition*, Cambridge University Press, 1992.

[83] D. H. Lehmer, *Annu. Comput. Lab. Harvard Univ.*, 1951, **26**, 141–146.

[84] S. Lavenberg, *Computer performance modeling handbook*, Elsevier, 1983.

[85] P. A. W. Lewis, A. S. Goodman, and J. M. Miller, *IBM Syst. J.*, 1969, **8**(2), 136–146.

[86] S. K. Park and K. W. Miller, *Commun. ACM*, 1988, **31**(10), 1192–1201.

[87] R. Coveyou and R. D. MacPherson, *J. ACM*, 1967, **14**(1), 100–119.

[88] G. Marsaglia and T. A. Bray, *SIAM Rev.*, 1964, **6**(3), 260–264.

[89] G. E. Box, *Ann. Math. Statist.*, 1958, **29**, 610–611.

[90] G. Marsaglia and W. W. Tsang, *J. Stat. Softw.*, 2000, **5**, 1–7.

[91] E. W. Becker, *Z. Phys. D*, 1986, **3**, 101–107.

[92] J. P. Toennies and A. F. Vilesov, *Annu. Rev. Phys. Chem.*, 1998, **49**, 1.

[93] M. Choi, G. Douberly, T. Falconer, W. Lewis, C. Lindsay, J. Merritt, P. Stiles, and R. Miller, *Int. Rev. Phys. Chem.*, 2006, **25**(1-2), 15–75.

[94] S. Yang and A. M. Ellis, *Chem. Soc. Rev.*, 2013, **42**(2), 472–484.

[95] A. Volk, P. Thaler, M. Koch, E. Fisslthaler, W. Grogger, and W. E. Ernst, *J. Chem. Phys.*, 2013, **138**(21), 214312.

[96] G. Douberly and R. Miller, *J. Chem. Phys.*, 2005, **122**(2), 024306.

[97] J. M. Merritt, J. Küpper, and R. E. Miller, *Phys. Chem. Chem. Phys.*, 2005, **7**(1), 67–78.

[98] J. Merritt, S. Rudić, and R. Miller, *J. Chem. Phys.*, 2006, **124**(8), 084301.

[99] S. Rudić, J. M. Merritt, and R. E. Miller, *Phys. Chem. Chem. Phys.*, 2009, **11**(26), 5345–5352.

[100] A. Harris, J. Brown, and C. Harris, *Annu. Rev. Phys. Chem.*, 1988, **39**(1), 341–366.

[101] J. N. Murrell, A. J. Stace, and R. Dammel, *J. Chem. Soc., Faraday Trans. 2*, 1978, **74**, 1532–1539.

[102] H. Hippler, K. Luther, and J. Troe, *Chem. Phys. Lett.*, 1972, **16**(1), 174–176.

[103] K. Luther and J. Troe, *Chem. Phys. Lett.*, 1974, **24**(1), 85–87.

[104] J.-C. Dutoit, J.-M. Zellweger, and H. Van den Bergh, *J. Chem. Phys.*, 1983, **78**(4), 1825–1837.

[105] B. Otto, J. Schroeder, and J. Troe, *J. Chem. Phys.*, 1984, **81**(1), 202–213.

[106] D. L. Bunker and B. S. Jacobson, *J. Am. Chem. Soc.*, 1972, **94**(6), 1843–1848.

[107] J. T. Hynes, R. Kapral, and G. M. Torrie, *J. Chem. Phys.*, 1980, **72**(1), 177–188.

[108] R.-E. Smalley, D.-H. Levy, and L. Wharton, *J. Chem. Phys.*, 1976, **64**(8), 3266–3276.

[109] J. J. Valentini and J. B. Cross, *J. Chem. Phys.*, 1982, **77**(1), 572–573.

[110] A. Rohrbacher, N. Halberstadt, and K. C. Janda, *Annu. Rev. Phys. Chem.*, 2000, **51**, 405.

[111] C. Leonard, F. Le Quere, and K. Peterson, *Phys. Chem. Chem. Phys.*, 2005, **7**(8), 1694–1699.

[112] G. Portwich, Semiklassische Simulation von Stoßprozessen zwischen Fremdatomen und großsen Heliumclustern Master's thesis, Universität Göttingen, 1995.

[113] P. Slavíček, P. Jungwirth, M. Lewerenz, N. H. Nahler, M. Fárník, and U. Buck, *J. Chem. Phys.*, 2004, **120**(9), 4498–4511.

[114] D. Bonhommeau, P. Lake Jr, C. Le Quiniou, M. Lewerenz, and N. Halberstadt, *J. Chem. Phys.*, 2007, **126**(5), 051104.

[115] N. Halberstadt and D. A. Bonhommeau, *J. Chem. Phys.*, 2020, **152**(23), 234305.

[116] M. Barranco and E. Hernández, *Phys. Rev. B*, 1994, **49**(17), 12078.

[117] J. Harms, J. P. Toennies, and F. Dalfovo, *Phys. Rev. B*, 1998, **58**(6), 3341.

[118] F. Ancilotto, P. B. Lerner, and M. W. Cole, *J. Low Temp. Phys.*, 1995, **101**(5), 1123–1146.

[119] K. K. Lehmann, *Mol. Phys.*, 1999, **97**(5), 645–666.

[120] R. M. Noyes, *J. Chem. Phys.*, 1954, **22**(8), 1349–1359.

[121] R. M. Noyes, *J. Am. Chem. Soc.*, 1955, **77**(8), 2042–2045.

[122] S. Goyal, D. Schutt, and G. Scoles, *J. Phys. Chem.*, 1993, **97**(10), 2236–2245.

[123] I. Reinhard, C. Callegari, A. Conjusteau, K. Lehmann, and G. Scoles, *Phys. Rev. Lett.*, 1999, **82**(25), 5036.

[124] C. Callegari, I. Reinhard, K. Lehmann, G. Scoles, K. Nauta, and R. Miller, *J. Chem. Phys.*, 2000, **113**(11), 4636–4646.

[125] K. Nauta and R. Miller, *J. Chem. Phys.*, 2000, **113**(21), 9466–9469.

[126] A. Vilà, M. Paniagua, and M. González, *Phys. Chem. Chem. Phys.*, 2018, **20**(1), 118–130.

[127] D. Rupp, N. Monserud, B. Langbehn, M. Sauppe, J. Zimmermann, Y. Ovcharenko, T. Möller, F. Frassetto, L. Poletto, A. Trabattoni, et al., *Nat. Commun.*, 2017, **8**(1), 1–7.

[128] B. Langbehn, K. Sander, Y. Ovcharenko, C. Peltz, A. Clark, M. Coreno, R. Cucini, M. Drabbels, P. Finetti, M. Di Fraia, et al., *Phys. Rev. Lett.*, 2018, **121**(25), 255301.

[129] N. Bohr and J. A. Wheeler, *Phys. Rev.*, 1939, **56**(5), 426.

[130] M. I. Sulaiman, S. Yang, and A. M. Ellis, *J. Phys. Chem. A*, 2017, **121**(4), 771–776.

[131] D. Verma, R. M. P. Tanyag, S. M. O'Connell, and A. F. Vilesov, *Adv. Phys.: X*, 2019, **4**(1), 1553569.

[132] D. Verma, S. Erukala, and A. F. Vilesov, *J. Phys. Chem. A*, 2020, **124**(30), 6207–6213.

[133] D. Spence, E. Latimer, C. Feng, A. Boatwright, A. M. Ellis, and S. Yang, *Phys. Chem. Chem. Phys.*, 2014, **16**(15), 6903–6906.

[134] R. Fernández-Perea, L. F. Gómez, C. Cabrillo, M. Pi, A. O. Mitrushchenkov, A. F. Vilesov, and M. P. de Lara-Castells, *J. Phys. Chem. C*, 2017, **121**(40), 22248–22257.

[135] E. Gordon, A. Karabulin, V. Matyushenko, V. Sizov, and I. Khodos, *Low Temp. Phys.*, 2010, **36**(7), 590–595.

[136] E. Gordon, A. Karabulin, V. Matyushenko, V. Sizov, and I. Khodos, *Chem. Phys. Lett.*, 2012, **519**, 64–68.

[137] E. Gordon, A. Karabulin, V. Matyushenko, V. Sizov, and I. Khodos, *Appl. Phys. Lett.*, 2012, **101**(5), 052605.

[138] O. Gessner and A. F. Vilesov, *Annu. Rev. Phys. Chem.*, 2019, **70**(1).

[139] A. Boatwright, C. Feng, D. Spence, E. Latimer, C. Binns, A. M. Ellis, and S. Yang, *Faraday Discuss.*, 2013, **162**, 113–124.

[140] S. B. Emery, K. B. Rider, B. K. Little, A. M. Schrand, and C. M. Lindsay, *J. Chem. Phys.*, 2013, **139**(5), 054307.

[141] P. Thaler, A. Volk, F. Lackner, J. Steurer, D. Knez, W. Grogger, F. Hofer, and W. E. Ernst, *Phys. Rev. B*, 2014, **90**(15), 155442.

[142] K. Atkins, *Phys. Rev.*, 1959, **116**(6), 1339.

[143] F. Coppens, F. Ancilotto, M. Barranco, N. Halberstadt, and M. Pi, *Phys. Chem. Chem. Phys.*, 2017, **19**(36), 24805–24818.

[144] C. F. Jones, C. Bernando, R. M. P. Tanyag, C. Bacellar, K. R. Ferguson, L. F. Gomez, D. Anielski, A. Belkacem, R. Boll, J. Bozek, et al., *Phys. Rev. B*, 2016, **93**(18), 180510.

[145] E. Latimer, D. Spence, C. Feng, A. Boatwright, A. M. Ellis, and S. Yang, *Nano Lett.*, 2014, **14**(5), 2902–2906.

[146] E. Garcia-Alfonso, M. Barranco, D. A. Bonhommeau, N. Halberstadt, M. Pi, and F. Calvo, *J. Chem. Phys.*, 2022, **157**(1), 014106.

[147] J. von Vangerow, A. Bogomolov, N. Dozmorov, D. Schomas, F. Stienkemeier, A. Baklanov, and M. Mudrich, *Phys. Chem. Chem. Phys.*, 2016, **18**(28), 18896–18904.

[148] C. Wasikowski and S. Klemm, Xmol 1.3.1, Research Equipment, Inc. d. BA Minnesota Supercomputer Center, 1993.

Part VI

Appendices

Appendix A

Interaction potentials

A.1 Lennard-Jones potentials

The Lennard-Jones parameters ε_0 and r_e given in Table A.1 for several atom pairs are used in the MD simulations [76].

	He-Ar	**He-I**	**He-Kr**	**He-Xe**	**Ar-Ar**	**Kr-Kr**	**Xe-Xe**
r_e **(Å)**	3.48041	4.0	3.69269	3.978	3.759	4.011	4.363
ε_0 **(cm**$^{-1}$**)**	20.551	18.5	20.47	19.527	99.546	139.91	196.2

Table A.1: Lennard-Jones potential parameters

A.2 Morse potentials

The parameters a, D_e and r_e given in Table A.2 characterize the Morse potential describing the quantum effective potential at 0.37 K and 0.5 K for the helium-helium interaction and for the iodine-iodine interaction [40].

	He-He at 0.37 K	**He-He at 0.5** K	**I-I**
a (Å^{-1}**)**	1	1	1.868
D$_e$ **(cm**$^{-1}$**)**	0.65	0.8	12,541
r$_e$ **(Å)**	4.1	4.1	2.67

Table A.2: Morse potential parameters

Appendix B

Tensor of inertia

The tensor of inertia I describes the spatial distribution of mass. The total angular momentum L is a summation over the masses m_i, their positions r_i and their linear velocities v_i or their angular velocities ω_i. Here the cross product is represented by the symbol $\times$.

$$\vec{\mathrm{L}} = \sum_i m_i \vec{r}_i \times \vec{v}_i = \sum_i m_i \left[r_i \times (\omega_i \times r_i) \right] = \sum_i m_i \begin{pmatrix} 0 & -z_i & y_i \\ z_i & 0 & -x_i \\ -y_i & x_i & 0 \end{pmatrix} \begin{pmatrix} 0 & -\omega_z & \omega_y \\ \omega_z & 0 & -\omega_x \\ -\omega_y & \omega_x & 0 \end{pmatrix} \begin{pmatrix} x_i \\ y_i \\ z_i \end{pmatrix}$$

$$= \sum_i m_i \begin{pmatrix} 0 & -z_i & y_i \\ z_i & 0 & -x_i \\ -y_i & x_i & 0 \end{pmatrix} \begin{pmatrix} \omega_y z_i - \omega_z y_i \\ \omega_z x_i - \omega_x z_i \\ \omega_x y_i - \omega_y x_i \end{pmatrix} = \sum_i m_i \begin{pmatrix} \omega_x \left(y_i^2 + z_i^2 \right) - \omega_y x_i y_i - \omega_z x_i z_i \\ -\omega_x y_i x_i + \omega_y \left(z_i^2 + x_i^2 \right) - \omega_z y_i z_i \\ -\omega_x z_i x_i - \omega_y z_i y_i + \omega_z \left(x_i^2 + y_i^2 \right) \end{pmatrix}$$

$$= \begin{pmatrix} \omega_x \sum_i m_i \left(y_i^2 + z_i^2 \right) - \omega_y \sum_i m_i x_i y_i - \omega_z \sum_i m_i x_i z_i \\ -\omega_x \sum_i m_i y_i x_i + \omega_y \sum_i m_i \left(z_i^2 + x_i^2 \right) - \omega_z \sum_i m_i y_i z_i \\ -\omega_x \sum_i m_i z_i x_i - \omega_y \sum_i m_i z_i y_i + \omega_z \sum_i m_i \left(x_i^2 + y_i^2 \right) \end{pmatrix}$$

$$= \begin{pmatrix} \sum_i m_i \left(y_i^2 + z_i^2 \right) & -\sum_i m_i x_i y_i & -\sum_i m_i x_i z_i \\ -\sum_i m_i y_i x_i & \sum_i m_i \left(z_i^2 + x_i^2 \right) & -\sum_i m_i y_i z_i \\ -\sum_i m_i z_i x_i & -\sum_i m_i z_i y_i & \sum_i m_i \left(x_i^2 + y_i^2 \right) \end{pmatrix} \begin{pmatrix} \omega_x \\ \omega_y \\ \omega_z \end{pmatrix} \tag{B.1}$$

The diagonal elements are equal to

$$\begin{aligned} \mathrm{I}_{xx} &= \sum_i m_i \left(y_i^2 + z_i^2\right) \\ \mathrm{I}_{yy} &= \sum_i m_i \left(x_i^2 + z_i^2\right) \\ \mathrm{I}_{zz} &= \sum_i m_i \left(x_i^2 + y_i^2\right) \end{aligned} \tag{B.2}$$

The non-diagonal elements are equal to

$$\begin{aligned} \mathrm{I}_{xy} &= -\sum_i m_i x_i y_i = \mathrm{I}_{yx} \\ \mathrm{I}_{xz} &= -\sum_i m_i x_i z_i = \mathrm{I}_{zx} \\ \mathrm{I}_{yz} &= -\sum_i m_i y_i z_i = \mathrm{I}_{zy} \end{aligned} \tag{B.3}$$

Appendix C

Rotation of He5000 at 8 $\hbar$/atom and 16 $\hbar$/atom

Several numerical rotation experiments have been made on helium nanoclusters by imposing a rotational energy equivalent to 8 $\hbar$/atom and 16 $\hbar$/atom.

Time (ps)	**6.85**	**95.9**	**746.65**	**1335.75**	**1938.55**	**2075.55**	**2233.1**
XY-plane			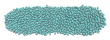	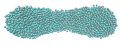	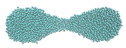	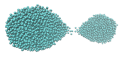	
XZ-plane				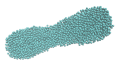	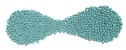	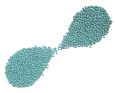	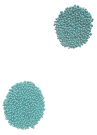

Table C.1: Evolution of helium nanodroplet fragmentation at 8 $\hbar$ rotating about the Y-axis

Time (ps)	**6.85**	**27.4**	**75.35**	**267.15**	**363.05**	**411**	**513.75**
XY-plane			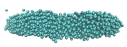		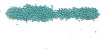	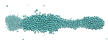	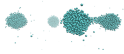
XZ-plane							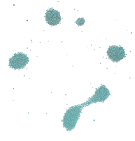

Table C.2: Evolution of helium nanodroplet fragmentation at 16 $\hbar$ rotating about the Y-axis

Appendix D

Some important files for the CLUSTER code

D.1 Example of configuration (CFG) file of HeND

The cfg file used and generated by the CLUSTER code has in the first line the total kinetic and potential energies calculated over all atoms in the file in joule. The positions on x,y and z are in meter (m) written in the lines in even number starting from line 2. The velocities on x,y and z are in meter per second (m/s) written in the lines in odd number starting from line 3. There are $2n_{atoms} + 1$ lines in this type of file without specification of the element.

```
-3.083657873668675E-019  3.068693401800398E-020
 2.821859116364030E-010 -3.142212598609716E-010 -1.940379075013650E-010
  9.81564947745843       0.992462529564055       3.53169154583238
 3.283695435341714E-010 -1.736962822043631E-010 -4.146215916168959E-010
  4.18759359598954       5.68063605479084       -2.88793233739580
-2.052273646034432E-010  5.502866575871868E-010  2.347063434701813E-009
 -3.12989770693456        45.9093799401392        68.5692011107588
-3.625830464072229E-011 -5.510426067700574E-010 -2.158330567432595E-010
  16.0167793276406       -89.7741462808851       -20.1618545561699
-8.291037475387546E-010  2.264330180642585E-009 -1.140916332811134E-009
 -28.4338926974040       -78.8687753777101       -8.20779347759080
 2.396790915954346E-010 -6.930302544716944E-010 -3.308842878462761E-010
 -14.7665558742859        14.2858657591788       -85.0547874794666
 5.506386437643907E-010 -5.222984298519725E-010 -3.961814455575408E-010
 -16.2515608608743       -39.9681191056863       34.0934642146463
 5.006735551384365E-010 -6.306469055311549E-010 -1.062240486320370E-010
 -28.2577549794460       -36.0376750290449       -32.5737081119176
-9.435465885002730E-010  1.309199905514168E-010 -1.565651586893858E-010
 -8.27887413990384        4.80334288436172        32.7263541382849
 1.326273408663586E-009 -1.373101256065270E-009  1.062770434310386E-009
  32.7371809205907       -42.3468510513864       -1.43833860319406
 2.049361716427157E-012 -2.682438077128221E-011 -2.222504241730497E-010
 -35.9124146391195        28.0209081507703       -18.4192326604493
 3.796820980054355E-010 -2.890964673237231E-010 -7.891907836825762E-010
-0.693643775029470        42.2324398966874        47.2173043033230
-1.159843405250163E-009 -4.623518922998785E-010  1.001782914166212E-009
 -39.8142583410144       -47.3218295250262        64.8457211774076
 6.894398621515587E-011 -8.105296271642203E-010 -5.909848684213156E-010
  50.8313243877043       -18.8756716731902       -31.0432431652537
 1.109234486230713E-011  2.342164479726926E-011 -5.457247743758940E-010
 3.263056516676466E-002   6.51468400048159        25.1179268251002
 6.145596139742896E-010 -3.727656812179215E-010  1.840778293914833E-011
 -10.3364109662483        14.4229481715989       -10.2195783786160
 1.939245695602315E-009  6.094026304007650E-010  1.171975526460850E-010
```

Figure D.1: Example of configuration file (cfg-file) of HeND

D.2 Example of XYZ file of HeND

Here is an example of xyz file commonly used in our MD to specify the geometry arrangement. This convention has first been introduced by the Minnesota Supercomputer Centre for the Xmol software [148]. The first line shows the total number of atoms and the number of atoms in each of the two subgroups. The second line is a comment line. Then the following lines are described as: in first column the chemical element and the second, third and fourth the xyz-positions in angstroms (Å).

```
  2493      2   2491
cluster xyz
 I   0.41298E+01 -0.46156E+01 -0.14706E+01
 I   0.45916E+01 -0.32103E+01 -0.36764E+01
 He -0.74433E+00  0.40295E+01  0.23940E+02
 He  0.94536E+00 -0.69838E+01 -0.16885E+01
 He -0.69831E+01  0.21170E+02 -0.10939E+02
 He  0.37047E+01 -0.84037E+01 -0.28390E+01
 He  0.68143E+01 -0.66964E+01 -0.34920E+01
 He  0.63147E+01 -0.77798E+01 -0.59245E+00
 He -0.81275E+01 -0.16418E+00 -0.10959E+01
 He  0.14571E+02 -0.15204E+02  0.11097E+02
 He  0.13284E+01 -0.17416E+01 -0.17527E+01
 He  0.51048E+01 -0.43643E+01 -0.74221E+01
 He -0.10290E+02 -0.60969E+01  0.10488E+02
 He  0.19974E+01 -0.95787E+01 -0.54392E+01
 He  0.14189E+01 -0.12392E+01 -0.49875E+01
 He  0.74535E+01 -0.52010E+01  0.65387E+00
 He  0.20700E+02  0.46207E+01  0.16418E+01
 He  0.18970E+01 -0.41169E+01 -0.65164E+01
 He  0.47590E+01  0.39837E+00 -0.53362E+01
 He  0.37541E+01 -0.34932E+01 -0.22916E+02
 He  0.69065E+01 -0.19158E+01 -0.67376E+01
 He  0.13419E+02  0.19580E+01 -0.14465E+02
 He -0.18738E+02 -0.15127E+02 -0.81551E+00
 He -0.64038E+01 -0.11482E+02  0.16825E+02
 He  0.28532E+01  0.81926E+01  0.25357E+02
 He  0.24568E+01 -0.16220E+02 -0.20150E+02
 He  0.13294E+01 -0.10454E+02 -0.22592E+01
 He  0.21768E+02  0.11184E+02  0.19394E+01
 He  0.62346E+00 -0.38957E+01 -0.36064E+01
 He -0.20554E+02  0.19261E+02 -0.50850E+01
 He -0.24795E+02 -0.50342E+01  0.58980E+01
 He  0.23552E+01 -0.13545E+02  0.12524E+02
```

Figure D.2: Example of xyz file of HeND

D.3 CLUSTER code input file

Figure D.3 presents the input file of the CLUSTER code. Two types of atoms can be simulated at the same time. At the end of the simulation some output files are generated with the name which has been given following by a specific termination which indicates the type of data collected. # introduces a comment line.

```
#  input for cluster program
#-----------------------------------------------
#  simulation of particle pickup from background gas by a
#  cluster with given parallel velocity
#-----------------------------------------------
#  header text to be printed:
pure helium cluster equilibration
# generic output file name
XXX
# initial md configuration file
YYY.cfg
# initial mc configuration file

#----------------------------
#   particle type 1 details
# iprot(1)  mass(1)  natoms(1)
    53        0        2
#  1-1 interaction, optional spline input file name

#  1-1 interaction, predefined potential via code
#     Morse
     5   3    2.666  1.868  375.
#----------------------------
#   particle type 2 details
# iprot(2)  mass(2)  natoms(2)
     2        0        2497
#  1-2 interaction, optional spline input file name

#  1-2 interaction, predefined potential via code
#      LJ
    0   2   18.5   4.
#--------------------------
#  2-2 interaction, optional spline input file name

#  2-2 interaction
#   morse potential optimised for density and cohesive energy
    5   3    4.1    1.    0.80
#--------------------------
#  ivvset  temp    iseed    vfact
    0       0.0  70209288    1.00
#  icmset  cmx   cmy   cmz  rfact
    1       0.    0.    0.   1.00
#  ipset    px   py   pz
    1       0.   0.   0.
#  ilset    lx   ly   lz
    0       0.   0.   0.
#  tstep/fs   nstep   nwait
     10      10000     000
#  itest  ideq   tfix
     0      0     0.0
#  ncorr  nwstep  nsamp  nhwait  refdis  rclose  nwxy
    200      0     50     1000      0.     6.0    50
#--------------------------
#       histogram parameters
# center of mass histogram 1      *.com1
   0.    40.   150
# center of mass histogram 2      *.com2
   0.    40.   150
# pair distribution histogram 1-1  *.p11
   2.    4.   100
# pair distribution histogram 2-2   *.p22
   0.    70.   100
# pair distribution histogram 1-2   *.p12
   0.    70.   100
```

Title of the simulation

Name of the general output name.*

Name of the initial cfg-file

Name of an xyz-file where speed are generated by MB distribution

Nuclear mass, nominal nuclear mass, number of atom type 1

Spline pair potential interaction 1-1

Analytical pair potential interaction 1-1

Nuclear mass, nominal nuclear mass, number of atom type 2

Spline pair potential interaction 1-2

Analytical pair potential interaction 1-2

Spline pair potential interaction 1-1

Analytical pair potential interaction 1-1

Maxwellian random velocity at temperature T (0: off ; >0: on)
Seed for random number generator
Velocity multiplier factor

ipset and ilset (0: off ; >0: on)
Velocity modificator for L and/or P momenta

Time step, number of time step and number of step before property averaging

Ideq: type of step integrator (0: Velocity Verlet; 1: Leap frog; 2: Verlet position) and thermostat (0: no thermostat)

ncorr: max. lenght of correlation function
nwstep: write cfg info on stepwide logfile every nwstep
nsamp: sampling every nsamp
refdis.: dist. ref. points from overall center of mass for octahedron in xyz output
rclose: max. dist for counting atoms as neighbours
nwxy: write xyz file every nwxyz step

Histogram parameters: starting point, ending point and number of bins

Figure D.3: Input of the CLUSTER MD code

Appendix E

Some important codes of the thesis

E.1 UNIRAN

The subroutine generates random uniform numbers.

```
165  subroutine uniran(invar,outvar)
166
167   implicit none
168   integer,parameter::a=16807,m=2147483647
169   integer,intent(inout)::invar
170   real(kind=8),intent(out)::outvar
171
172   invar=a*(invar-m*int(invar/m))
173   outvar=real(invar)/m
174  if (outvar<0) then
175      outvar=1+outvar
176  endif
177  if (outvar>1) then
178      outvar=outvar-1
179  endif
180
181  end subroutine uniran
```

Figure E.1: Subroutine UNIRAN

E.2 GAUSSRAN

The subroutine generates random normal numbers.

```
1   subroutine gaussran(invar,out1,out2)
2
3   implicit none
4   integer,intent(inout)::invar
5   real(kind=8),intent(out)::out1,out2
6   real(kind=8)::v1,v2,univar,fac,s
7
8   s=1
9   do while((s>=1).or.(s==0))
10      call uniran(invar,univar)
11      v1=2*univar-1.
12      call uniran(invar,univar)
13      v2=2*univar-1.
14      s=v1**2+v2**2
15  enddo
16  fac=sqrt(-2*log(s)/s)
17  out1=fac*v1
18  out2=fac*v2
19
20  end subroutine gaussran
```

Figure E.2: Subroutine GAUSSRAN

E.3 Fortran 90 Complete clustering algorithm

Recursion in Fortran90 needs two identical CCA subroutines (Figure E.3) which call each other sharing informations about neighbour numbers of a computed atom through the main loop.

```
100     tree_number = 0
101     in_atoms = 1
102     call cpu_time(start2)
103   do while (in_atoms<=natoms)
104   	if (tree_id(in_atoms)==0) then
105   	    tree_number = tree_number + 1
106   	    call append_to_list(in_atoms)
107   	endif
108   	in_atoms = in_atoms + 1
109   enddo
127   subroutine append_to_list1(input)
128   use declare
129   implicit none
130   integer,intent(in)::input
131
132   tree_id(input) = tree_number
133   voisins=0
134   do n=1,neighnumb
135   	if (list(input,n)/=0) then
136   	    voisins = voisins + 1
137   	endif
138   enddo
139   do compteur=1,voisins
140   	if (tree_id(list(input,compteur)) == 0) then
141   	    call append_to_list2(list(input,compteur))
142   	endif
143   enddo
144   compteur = 0
145
146   end subroutine append_to_list
```

Figure E.3: Main loop of Complete clustering algorithm in Fortran90

E.4 Photodissociation

```
51  rx_I2 = rx(1) - rx(2)
52  ry_I2 = ry(1) - ry(2)
53  rz_I2 = rz(1) - rz(2)
54  r_I2 = sqrt(rx_I2**2+ry_I2**2+rz_I2**2)
55  print*,'r_I2 =',r_I2
56
57  !Colinearity parameter k (vrel=k.rI2) and relative velocity
58  k = sqrt((4/mass_I)*(1/(r_I2**2))*Ex)
59  vrel = k*r_I2
60  print*,'Relative velocity between iodines is',vrel,'m.s^(-1)'
61
62  !Excess speed adding
63  vx(1) = vx(1) + k*rx_I2/2
64  vy(1) = vy(1) + k*ry_I2/2
65  vz(1) = vz(1) + k*rz_I2/2
66  vx(2) = vx(2) - k*rx_I2/2
67  vy(2) = vy(2) - k*ry_I2/2
68  vz(2) = vz(2) - k*rz_I2/2
```

Figure E.4: Photodissociation code in Fortran90

E.5 Automation of the photodissociation process

```
for (( i=0; i<$iteration; i++ ))
    do
    j=$(($i+1))
    cat equi.cluster | sed s/YYY/$i/ | sed s/XXX/$j/ > equi-new.cluster
    cluster2 < equi-new.cluster
    cat autozapcfg | sed s/YYY/$i/ | sed s/XXX/$j/ > autozapcfg-new
    cfgzap-v5 < autozapcfg-new
    cat zaping.cluster | sed s/YYY/$i/ | sed s/XXX/$j/ > zaping-new.cluster
    cluster2 < zaping-new.cluster
    cat eqzap.cluster | sed s/XXX/$j/ > eqzap-new.cluster
    cluster2 < eqzap-new.cluster
    echo '1 '`tail --lines=1 eqzap_$j.cage | cut -c 30-39` >> v1.log
    echo '1 '`tail --lines=1 eqzap_$j.cage | cut -c 40-49` >> v2.log
    echo '1 '`tail --lines=1 eqzap_$j.cage | cut -c 94-97` >> ag1.log
    echo '1 '`tail --lines=1 eqzap_$j.cage | cut -c 103-106` >> ag2.log
    rm -f equi-new.cluster autozapcfg-new zaping-new.cluster zaping_$j.cfg eqzap-new.cluster
done
```

EQUI MD

Modification of I_2 velocity

ZAPING MD

EQZAP MD

Data collection

Figure E.5: Automation of photodissociation process in Shell scripting

E.6 Dopant impact code

```
print*,'xmax =',xmax
print*,'ymin =',ymin
print*,'ymax =',ymax
print*,'zmin =',zmin
print*,'zmax =',zmax
print*,'Diameter in x-axis :',xmax-xmin,'m'
print*,'Diameter in y-axis :',ymax-ymin,'m'
print*,'Diameter in y-axis :',zmax-zmin,'m'

!Mise en place de l'impact sur la surface de l'agrégat
call uniran(u,uniform)
rrx(1)=xmin+(xmax-xmin)*uniform
call uniran(u,uniform)
rry(1)=ymin+(ymax-ymin)*uniform
do while (rrx(1)**2+rry(1)**2>0.25*((xmax-xmin)/2 + (ymax-ymin)/2)**2)
    call uniran(u,uniform)
    rrx(1)=xmin+(xmax-xmin)*uniform
    call uniran(u,uniform)
    rry(1)=ymin+(ymax-ymin)*uniform
enddo
rrz(1)=100E-10 + zmax
print*,'New x-position :',rrx(1)
print*,'New y-position :',rry(1)
print*,'New z-position :',rrz(1)

v=1
do while(v>=0)
call gaussran(u,g1,g2)
v=g1*sqrt(kb*T/mass)-v_agreg
enddo
vvx(1)=0
vvy(1)=0
vvz(1)=v
print*,'Iodine velocity :',v,'m/s'
```

HeND diameter calculation

Selection of the impact point on the XY-plan of the droplet

Ensure a collision by selecting a point on the circle which defines the surface of the droplet

The dopant is placed at 100 Å from de XY-droplet surface

The dopant travel from (+) to (-) coordinates in the space

Figure E.6: Doping code in Fortran90

E.7 Automation of the single dopant impact

```
for (( i=0; i<$iteration; i++ ))
    do
    j=$((i+1))
    a=`head -1 SEED_FILE`        → Initialisation of a seed for random numbers
    b=$((a+1-1))

    cat input-impact | sed s/SEED/$b/ > input-impact-new
    Multimpact < input-impact-new        → Launching of the position and velocity of the dopant
    echo `head -1 SEED_FILE` >> SEED_HISTORY
    Z_Impact        → Determination of the Z coordinate of th dopant-cluster impact point

    cat equi.cluster | sed s/XXX/$j/ > equi-new.cluster
    cluster2 < equi-new.cluster        → MD of the doping
    cp equi_$j.cfg equi_$j-og.cfg

    cat input-tree | sed s/XXX/$j/ > input-tree-new        → Complete clustering to find the doped cluster
    TreeforMMI_Xe < input-tree-new

    cat input-APD | sed s/XXX/$j/ > input-APD-new        → Calculation of the average penetration depth
    APD_distance < input-APD-new

    cat input-LR | sed s/XXX/$j/ > input-LR-new        → Calculation of the linear and rotational momenta transmission
    LR_momentum_Xe < input-LR-new                        dopant → HeND

    rm -f equi-new.cluster input-impact-new input-tree-new input-APD-new input-LR-new equi_0.cfg Dopant_Coord XYZ_dopant
done
```

Figure E.7: Single doping automation code in Shell scripting

E.8 Automation of the multiple dopant impact

```
for (( i=0; i<$iteration; i++ ))
    do
        j=$((i+1))
        a=`head -1 SEED_FILE`                    --> Initialisation of a seed for random numbers
        b=$((a+1-1))
        if [ $i -eq 0 ]                          --> Condition of first impact to avoid the overwriting of xyz position in VMD
        then
            cat equi.cluster | sed s/ZZZ/$i/ | sed s/YYY/$i/ | sed s/XXX/$j/ > equi-new.cluster
            cluster2 < equi-new.cluster          --> Equilibration of the non-doped HeND
            cp equi_${j}.cfg equi-${j}.cfg

            cat input-impact | sed s/YYY/$i/ | sed s/XXX/$j/ | sed s/SEED/$b/ > input-impact-new
            Multimpact < input-impact-new        --> Launching of the position and velocity modification of the dopant
            echo `head -1 SEED_FILE` >> SEED_HISTORY

            cat eqflight.cluster | sed s/ZZZ/$j/ | sed s/YYY/$i/ | sed s/XXX/$j/ > eqflight-new.cluster
            cluster2 < eqflight-new.cluster      --> MD of the doping
            cp eqflight_${i}.cfg eqflight-${i}.cfg

            cat input-tree | sed s/YYY/$i/ | sed s/XXX/$j/ > input-tree-new
            Treeforimpact-II < input-tree-new    --> Complete clustering to find the main doped cluster
            c=`head -1 XE_IN`
            d=$((c+1-1))

            cat zero-energy.cluster | sed s/ZZZ/$d/ | sed s/YYY/$i/ | sed s/XXX/$j/ > zero-energy-new.cluster
            cluster2 < zero-energy-new.cluster   --> MD of to relaxation the system : T=0.38 K; L=0; P=0

            rm -f equi-new.cluster input-impact-new input-tree-new eqflight-new.cluster zero-energy-new.cluster equi_$j.cfg eqflight_$j.cfg
        elif [ $i -gt 0 ]
        then
            cat input-dopanalysis | sed s/XXX/$i/ > input-dopanalysis-new
            Dopanalysis < input-dopanalysis-new
            c=`head -1 XE_IN`                    --> Analysis of XYZ file for avoiding the xyz
            d=$((c+1-1))                             position in VMD for the video visualisation
            e=$((c+1))

            cat equi.cluster | sed s/ZZZ/$d/ | sed s/YYY/$i/ | sed s/XXX/$j/ > equi-new.cluster
            cluster2 < equi-new.cluster
            cp equi_${j}.cfg equi-${j}.cfg       --> Equilibration of the n-time doped HeND

            cat input-impact | sed s/YYY/$i/ | sed s/XXX/$j/ | sed s/SEED/$b/ > input-impact-new
            Multimpact < input-impact-new
            echo `head -1 SEED_FILE` >> SEED_HISTORY --> Launching of the position and velocity modification of the n-dopant

            cat eqflight.cluster | sed s/ZZZ/$e/ | sed s/YYY/$i/ | sed s/XXX/$j/ > eqflight-new.cluster
            cluster2 < eqflight-new.cluster
            cp eqflight_${i}.cfg eqflight-${i}.cfg --> MD of the doping

            cat input-tree | sed s/YYY/$i/ | sed s/XXX/$j/ > input-tree-new
            Treeforimpact-II < input-tree-new
            c=`head -1 XE_IN`                    --> Complete clustering to find the main doped cluster
            d=$((c+1-1))

            cat zero-energy.cluster | sed s/ZZZ/$d/ | sed s/YYY/$i/ | sed s/XXX/$j/ > zero-energy-new.cluster
            cluster2 < zero-energy-new.cluster   --> MD of to relaxation the system : T=0.38 K; L=0; P=0

            rm -f equi-new.cluster input-impact-new input-tree-new eqflight-new.cluster zero-energy-new.cluster equi_$j.cfg eqflight_$j.cfg
            mv zero-energy_$j.cfg equi_$j.cfg
        fi
done
```

Figure E.8: Multiple doping automation code in Shell scripting

E.9 VMD video script

```
for {set i 1 } {$i < 400 } { incr i } {
mol addfile rot40000_$i.xyz
}
```